Universitatea „Politehnica“
Timisoara

Fachhochschule
Gelsenkirchen

Wear Resistance Improvement of Titanium by Surface Alloying using Electron Beam Irradiation

PhD Thesis

submitted by

Dipl. Eng. Călin – Marius POGAN

for the award of the degree of

DOCTOR OF ENGINEERING

Scientific coordinators:

Prof. Dr. - Eng. Ion Mitelea

Prof. Dr. - Eng. Waltraut Brandl

- 2011 -

Acknowledgments

I would like to express my sincere gratitude to my scientific supervisors, Prof. Dr.-Eng. Waltraut Brandl and Prof. Dr.-Eng. Ion Mitelea for their encouragement and guidance throughout the achievement of my Ph.D thesis, and for their invaluable suggestions and unwavering support.

My honest gratefulness to Prof.Dr.-Eng. Rainer Sievers from the University of Applied Sciences Gelsenkirchen, Dr.-Eng. Klaus Schulze and Dipl.-Eng. Bernhard Jung from PTR Präzisionstechnik GmbH for their wise words and the possibility of conducting my experiments in their institutions.

And last but not least, i would like to thank my friends and colleagues Dr.-Eng. Gabriela Mărginean and Dipl.-Eng. Ioan Secosan for their support.

CONTENT

List of Figures vi

List of Tables ix

Preface 1

Chapter I Theoretical aspects regarding properties and limitations of titanium and titanium alloys 4

1.1 Titanium and titanium alloys 4

1.1.1 Alloying and alloy classification 5

1.1.1.1 Alloying behavior 5

1.1.1.2 Alloy classification 6

1.1.2 Properties of titanium and titanium alloys 8

1.1.2.1 General properties 8

1.1.2.2 Corrosion behavior of titanium and its alloys 10

1.1.3 Applications 12

1.1.4 Limitations of titanium and its alloys 15

1.2 Friction and Wear 17

1.2.1 Friction 18

1.2.1.1 Friction mechanisms 19

1.2.1.2 Stages in friction mechanisms 20

1.2.1.3 Friction of metals 21

1.2.2 Wear 24

1.2.2.1 Stages of wear 26

1.2.2.2 Types of wear 27

1.2.2.3 Wear rate 30

1.3 Surface engineering methods of titanium 31

1.3.1 Ion implantation 31

1.3.2 Thermo-chemical diffusion treatments 33

1.3.2.1 Nitriding 33

1.3.2.2 Oxidizing 34

1.3.2.3 Carburizing 35

1.3.2.4 Boronizing 35

1.3.3 Plating 36

1.3.4 Laser surface treatments 37

1.3.4.1 Laser surface melting 37

1.3.4.2 Laser surface alloying 38

1.3.4.3 Laser cladding 40

1.3.5 Thermally sprayed coatings 40

Chapter II Experimental program 43
2.1 Materials 43
2.1.1 Titanium base material 43
2.1.2 Powder material 43
2.1.2.1 Al8Si20BN powder 44
2.1.2.2 WC-CoCr 86 10 4 powder 45
2.2 Deposition techniques 46
2.2.1 Atmospheric Plasma Spraying (APS) 46
2.2.1.1 Principle of atmospheric plasma spraying 46
2.2.1.2 Unique features of plasma spray process 47
2.2.2 High Velocity Oxygen-Fuel (HVOF) 48
2.2.2.1 Principle of the high velocity oxygen fuel technique 48
2.2.2.2 Characteristics of the HVOF spray method 49
2.3 Methods of investigation 49
2.3.1 X – Ray diffraction 50
2.3.1.1 The nature of X - rays 51
2.3.1.2 The detection of X - rays 52
2.3.1.3 Bravais Lattices 52
2.3.1.4 Miller Indices 53
2.3.1.5 Diffraction and Bragg´s Law 54
2.3.2 Scanning electron microscopy (SEM) 55
2.3.2.1 SEM principle 56
2.3.2.2 Secondary electrons 57
2.3.2.3 Back-scattered electrons 57
2.3.2.4 Energy dispersive X-ray spectroscopy 58
2.3.3 Pin-on-disc method 59
2.3.3.1 Friction coefficient and wear rate determination 60
2.3.4 Hole drilling residual stress measurement 61
2.3.4.1 Principle of the hole drilling method 62
2.3.4.2 Data processing 62
2.3.5 Electrochemical corrosion test 64
2.3.5.1 Large signal polarization 65
Chapter III Powder deposition 67
3.1 Sample preparation 67
3.2 Process parameters 68
3.2.1 A.P.S parameters used by the deposition of the Al8Si20BN 68
3.2.2 HVOF parameters used by the deposition of the WC-CoCr 84-10-4 69
3.3 Investigation of the as-sprayed coatings 70
3.4 Conclusions 71

Chapter IV Electron beam remelting of the pre-deposited coatings 72
4.1 Electron beam surface engineering 72
4.1.1 Electron beam hardening (EBH) 73
4.1.2 Electron beam shock processing (EBS) 74
4.1.3 Electron beam remelting (EBR) 75
4.1.4 Electron beam cladding (EBC) 76
4.1.5. Electron beam alloying (EBA) 77
4.1.6 Electron beam versus conventional methods 79
4.2 Structural modifications in the substrate – coating system 80
4.2.1 Structural modifications in the titanium – boron nitride system 81
4.2.1.1 Remelting parameters 81
4.2.1.2 Penetration depth of the remelted samples 82
4.2.1.3 Microstructure and phase composition of the TiBN samples 83
4.2.2 Structural modifications in the titanium – tungsten carbide system 88
4.2.2.1 Remelting parameters 88
4.2.2.2 Penetration depth of the remelted samples 89
4.2.2.3 Microstructure and phase composition of the TiWC samples 90
4.3 Tribological and corrosive behavior of the alloyed surfaces 95
4.3.1 Surface properties of the TiBN samples 95
4.3.1.1 Vickers microhardness 95
4.3.1.2 Friction coefficient and sliding wear rate of the alloyed TiBN samples 97
4.3.1.3 Corrosion behavior of the alloyed TiBN samples 102
4.3.2 Surface properties of the TiWC samples 104
4.3.2.1 Vickers microhardness 104
4.3.2.2 Friction coefficient and sliding wear rate of the alloyed TiWC samples 105
4.3.2.3 Corrosion behavior of the alloyed TiWC samples 111
4.4 Residual stresses in the alloyed samples 112
4.4.1 Residual stresses in the TiBN samples 112
4.4.2 Residual stresses in the TiWC samples 114
4.5 Conclusions 116
Chapter V General conclusions, original contributions and future recommendations 117
5.1 Conclusions 117
5.2 Original contributions 118
5.2 Future recommendations 119

References 120
APPENDIX 128

LIST OF FIGURES

Figure	*Description*	*Page No.*
1.1	Allotropic forms of titanium	5
1.2	The influence of the alloying elements on the phase diagram of Ti alloys	6
1.3	Titanium jet engine (frame, fan blades, shafts, discs, etc.)	12
1.4	Titanium landing gear	13
1.5	Satellite fuel tank	13
1.6	Titanium in automotive applications	14
1.7	Military applications of titanium (a. helicopter rotor head, b. bulkhead, c. tank center)	14
1.8	Titanium in sports and medical application	15
1.9	Slip systems in (hcp) structure	
1.10	Several material, contact conditions and environmental parameters which control friction and wear	17
1.11	The three components of sliding friction	18
1.12	The six stages of friction mechanisms	20
1.13	Friction coefficients of metals in contact with themselves at very low loads and sliding velocities	22
1.14	Friction coefficient vs temperature as a function of phase transformation for cobalt on cobalt	23
1.15	Wear coefficient as a function of friction	24
1.16	Wear rate of zirconium oxide as function of fracture toughness	25
1.17	Stages of wear	26
1.18	Adhesive wear mechanism	27
1.19	Abrasive wear mechanism	28
1.20	Fatigue wear mechanism	29
1.21	Chemical wear mechanism	29
1.22	Breakthrough load for titanium substrate – ion combinations	31
1.23	Wear volume loss of untreated and nitrogen implanted Ti-6Al-4V	32
1.24	Microhardness profile of plasma-nitrated Ti-6Al-4V	33
1.25	Effect of interstitial alloying on the strength of titanium	34
1.26	Influence of the gas mixture on the hardness profile of laser-nitrated Ti-6Al-4V	38
1.27	Hardness profile of SiC laser alloyed Ti-6Al-4V	39
1.28	Hardness of cobalt-based clad layer on Ti-6Al-4V	40
1.29	Characteristics of flame and plasma spraying	42
2.1	SEM micrograph of the Al8Si20BN powder	44
2.2	EDX and X-ray diffraction pattern of the Al8Si20BN powder	44
2.3	SEM micrograph of the WC-CoCr 86 10 4 powder	45
2.4	EDX analysis and XRD pattern of the WC-CoCr 84-10-6 powder	45
2.5	Atmospheric plasma spray principle	46

2.6	High Velocity Oxygen Fuel principle	48
2.7	X´pert MPD diffractometer	50
2.8	Bragg´s law	54
2.9	XL 30 ESEM scanning electron microscope	55
2.10	Principle of scanning electron microscopy	56
2.11	EDX principle	58
2.12	CSM pin-on-disc tribometer	59
2.13	Coefficient of friction measurement	60
2.14	Wear groove geometry	60
2.15	RESTAN residual stress measurement device	61
2.16	ASTM standard strain gage rosette	62
2.17	Electrochemical corrosion cell	64
2.18	Tafel extrapolation	65
3.1	Sand-blasting effect on the surface geometry	67
3.2	SEM micrograph of the Al8Si20BN powder	70
3.3	SEM micrograph of the WC-CoCr 84-10-6 powder	71
4.1	Classification of electron beam surface engineering processes	72
4.2	Electron beam transformation hardening	73
4.3	Electron beam shock hardening	75
4.4	Electron beam remelting	75
4.5	Electron beam cladding	76
4.6	One-stage and two-stage electron beam alloying	77
4.7	Stages involved in EB alloying	78
4.8	BW 700/3-6 electron beam equipment	80
4.9	Schematic of remelted samples	81
4.10	Remelted depths of the TiBN samples	82
4.11	SEM micrographs of the TiBN1.3 sample	83
4.12	EDX measurement on the light gray phase	83
4.13	X-Ray diffraction pattern of sample TiBN1.3	84
4.14	SEM micrographs of the TiBN1.4 sample	85
4.15	EDX analysis on the bright phase	85
4.16	X-Ray diffraction pattern of sample TiBN1.4	85
4.17	SEM micrographs of the TiBN2.2 sample	86
4.18	EDX analysis on the needle shaped phase	86
4.19	X-Ray diffraction pattern of sample TiBN2.2	86
4.20	SEM micrographs of the TiBN2.4 sample	87
4.21	X-ray diffraction pattern of sample TiBN2.4	87
4.22	Penetration depths of the TiWC samples	89
4.23	SEM micrographs of the TiWC2.3 sample	90

4.24	EDX analysis on the bright phase	90
4.25	X-ray diffraction pattern of sample TiWC2.3	91
4.26	SEM micrographs of the TiWC2.4 sample	91
4.27	EDX analysis of the dark denditric phase	91
4.28	X-ray diffraction pattern of sample TiWC2.4	92
4.29	SEM micrographs of the TiWC2.5 sample	92
4.30	XRD analysis on the dark gray phases	92
4.31	X-ray diffraction pattern of sample TiWC2.5	93
4.32	SEM micrographs of the TiWC2.6 sample	94
4.33	X-ray diffraction pattern of the TiWC2.6 sample	94
4.34	Hardness gradient of the TiBN samples	95
4.35	Overall bulk microhardness of the TIBN samples	96
4.36	Friction coefficient of the titanium substrate	97
4.37	Friction coefficient of sample TiBN1.3	97
4.38	Friction coefficient of sample TiBN1.4	98
4.39	Friction coefficient of sample TiBN2.2	98
4.40	Friction coefficient of sample TiBN2.4	98
4.41	Wear track of the titanium substrate	99
4.42	Wear track and ball wear of sample TiBN1.3	100
4.43	Wear track and ball wear of sample TiBN1.4	100
4.44	Wear track and ball wear by sample TiBN2.2	101
4.45	Wear track and ball wear by sample TiBN2.4	101
4.46	Wear rate histogram of the TiBN samples	102
4.47	Polarization curves of the TiBN samples	103
4.48	Hardness gradient of the TiWC samples	104
4.49	Overall bulk hardness of the TiWC samples	105
4.50	Friction coefficient of sample TiWC2.3	106
4.51	Friction coefficient of sample TiWC2.4	106
4.52	Friction coefficient of sample TiWC2.5	106
4.53	Friction coefficient of sample TiWC2.6	107
4.54	Wear track and ball wear by sample TiWC2.3	108
4.55	Wear track and ball wear by sample TiWC2.4	108
4.56	Wear track and ball wear by sample TiWC2.5	109
4.57	Wear track and ball wear by sample TiWC2.6	109
4.58	Wear rate histogram of the TiWC samples	110
4.59	Polarization curves of the TiWC samples	111
4.60	Stress distribution in sample TiBN1.3	112
4.61	Stress distribution in sample TiBN1.4	112
4.62	Stress distribution in sample TiBN2.2	113

4.63 Strain distribution in sample TiBN2.4 113
4.64 Strain distribution in sample TiWC2.3 114
4.65 Strain distribution in sample TiWC2.4 114
4.66 Strain distribution in sample TiWC2.5 115
4.67 Strain distribution in sample TiWC2.6 115

LIST OF TABLES

Table	*Description*	*Page No.*
1.1	Properties of α, (α+β) and β titanium alloys	8
1.2	Physical and mechanical properties of titanium alloys	9
1.3	Corrosive environments where titanium's oxide film provides resistance	11
1.4	Crystal structure characteristics	16
2.1	Chemical composition of TIKRUTAN RT 12	43
2.2	Crystal systems and Bravais lattices	53
3.1	APS parameters used for the deposition of the BN powder	68
3.2	HVOF parameters used for the deposition of the WC powder	69
4.1	Characteristics of EB and EB technologies	79
4.2	Electron beam remelting conditions	80
4.3	Remelting parameters of the Al8Si20BN coating	81
4.4	Phase composition of TiBN samples	87
4.5	Remelting parameters of the WC-CoCr coating	88
4.6	Phase composition of TiWC samples	94
4.7	Friction coefficient values of the TiBN samples	99
4.8	Wear measurements of the TiBN samples	101
4.9	Corrosion values of the tested TiBN samples	103
4.10	Friction coefficient values of the TiWC samples	107
4.11	Wear measurements of the TiWC samples	106
4.12	Corrosion values of the tested TiWC samples	111

Preface

Introduction

The ever-increasing demand for higher performance, weight reduction and more challenging application conditions have been the main driver for substituting steel and cast iron components with those of light weight metals, such as titanium and aluminium [1]. However, these materials are characterized by low hardness and wear resistance, which have been a severe barrier to tribological applications. This shortcoming can be overcome by means of material and component – specific surface engineering.

The aim of surface engineering is to achieve the desired properties specifically at the surface of a component. In many cases it might be strategic to combine desirable bulk properties of an underlying substrate material (e.g. low density, high toughness) with enhanced properties of the external surfaces (e.g. hardness, wear and corrosion resistance) [2].

A variety of surface engineering techniques have been applied with the aim of improving titanium´s tribological properties. Such techniques include ion implantation [3], PVD coatings [4], CVD coatings [5] and laser cladding [6]. The common goal of these techniques is to deposit an outer layer with improved tribological properties, such as TiN [7], CrN [8], diamond [5], TiB [6], TiC [9] and ZrN [10].

Thermally sprayed coatings are increasingly used due to their high deposition rates and capability of depositing a large variety of materials. Therefore, among many coating methods, thermal spraying is considered to be one of the most efficient, especially for thick coatings. Thermally sprayed coatings consist of lamellar structures of flattened solidified fine particles. The bonding strength is mainly determined by the mechanical anchoring effect between the substrate and particles and a sintering between the particles.

In the case of titanium alloys, the coating process may have a disadvantageous effect on their corrosion behavior. Therefore, it is desirable to combine titanium's corrosion resistance with the hardness and good tribological properties of the thermal sprayed coating.

Motivation

Despite the numerous surface engineering methods, some limitations of these surface engineering techniques exist, including porosity, insufficient thickness, delamination [10], high residual stresses [5] and long manufacturing times. Due to the described structure of the sprayed coatings and a lack of metallurgical bonding between the lamella, thermal sprayed coatings may have disadvantages such as low coating strength and low interface strength between the substrate and coating [11].

The most efficient and reliable technique that provides the desired metallurgical interface structure and combined properties is electron beam alloying of the coating with the base material, due to its advantages over laser technology concerning beam oscillation, penetration depths and process conditions.

This thesis aims at contributing to the ongoing effort of understanding the low friction and wear resistant coatings. The focus is on the characterization of the microstructure and mechanical properties of titanium surfaces alloyed with boron nitride (BN) in aluminium – silicon and tungsten carbide (WC) in cobalt – chromium powders, through

electron beam irradiation.

Accordingly, the thesis has been structured into the following chapters: chapter 1 displays theoretical aspects regarding surface properties of titanium alloys, as well as the current trends in surface engineering of titanium; chapter 2 presents the experimental program concerning the coating and substrate materials, deposition and investigation methods; chapter 3 concentrates on powder deposition and characterization of the as-sprayed coatings; chapter 4 is dedicated to the electron beam engineering processes, as well as the characterization of the structural and mechanical properties of the alloyed samples and chapter 5 points out the general conclusions and original contributions of the present work.

Chapter I

Theoretical aspects regarding properties and limitations of titanium and titanium alloys

1.1 Titanium and titanium alloys

Titanium has often been referred as the “wonder metal” with excellent strength, ductility and fracture resistant characteristics in combination with superior environmental resistance. The element is the fourth most abundant structural element in Earth’s crust (behind Al, Fe and Mg), occurring mainly as rutile (TiO_2) and ilmenite ($FeTiO_3$) [12].

Titanium is one of the few allotropic metals that can exist in two different crystallographic forms. At room temperature, it has a close-packed hexagonal structure, designated as the alpha phase. At around 882°C the alpha phase transforms to a body-centered cubic structure, known as the beta phase, which is stable up to titanium’s melting point of about 1677°C [13]. This allotropic transformation allows the opportunity for formation of alloys composed of α, β or α/β microstructures, in addition to compound formation in certain alloys.

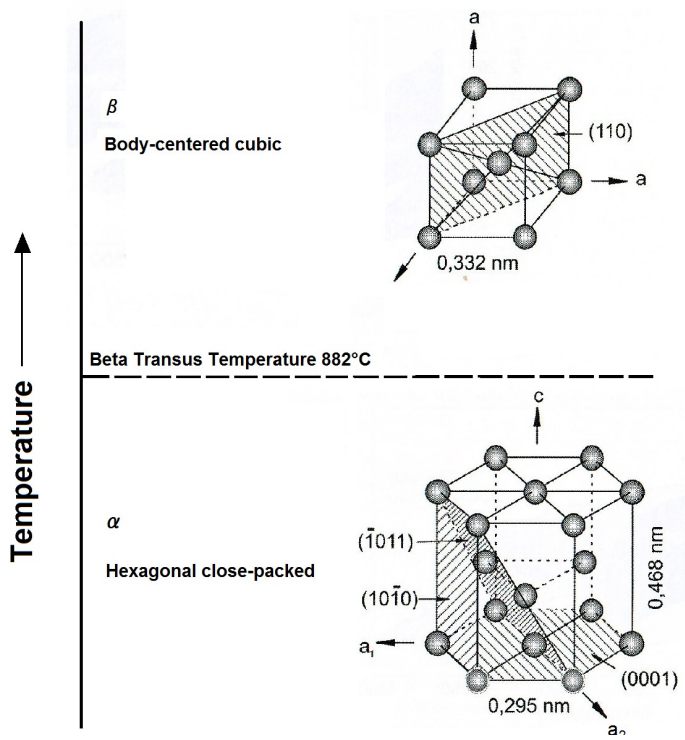

Figure 1.1 *Allotropic forms of titanium [19]*

Metallic titanium can be divided into two main categories: corrosion resistant (essentially titanium alloyed to a minor extent) and structural use (for which titanium is more highly alloyed to increase the strength level while maintaining usable levels of other mechanical properties such as ductility) [14,15].

1.1.1 Alloying and alloy classification

1.1.1.1 Alloying behavior

The choice of alloying elements is determined by the ability of the element to stabilize either the α or the β phase [16]. Aluminium, oxygen, nitrogen, gallium and carbon are the most common α-stabilizing elements. Zirconium, tin and silicon are viewed as neutral in their ability to stabilize either phase. Elements that stabilize the β phase can either form binary systems of the β-isomorphous-type or the β-eutectoid-type. Elements forming the isomorphous type binary system include molybdenum, vanadium and

tantalum, while copper, manganese, chrome, iron, nickel, cobalt and hydrogen are eutectoid formers in which compounds may form. The β-isomorphous alloying elements, which do not form intermetallic compounds, have traditionally been preferred to the eutectoid-type elements as additional to α/β or β-alloys to improve hardenability and increase response to heat treatment.

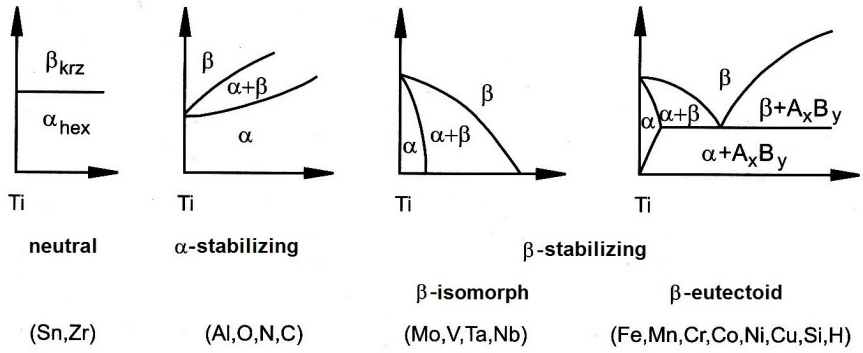

Figure 1.2 *The influence of the alloying elements on the phase diagram of Ti alloys [16]*

1.1.1.2 Alloy classification

Depending on the microstructure of the alloy phase, there are three main structural types of titanium alloys:

a. Alpha alloys contain predominantly α-phase at temperatures up to well above 540°C. A major class of the α-alloys is the unalloyed titanium family of alloys that differ in the amount of oxygen and iron in each alloy. Alloys with higher interstitial content are higher in strength, hardness and transformation temperature compared to high purity alloys [17]. Other α alloys contain additions such as aluminium and tin. Generally, α-rich alloys are more resistant to high-temperature creep than α/β or β-alloys, and they exhibit little strengthening by heat treatment. These alloys are usually annealed or recrystallized to remove stress from cold working and they have good weldability and generally inferior forgeability in comparison to α/β or β-alloys. A few α alloys are: Ti-5Al-2.5Sn, Ti-6Al-2Sn-4Zr-2Mo, Ti-8Al-1Mo-1V.

b. Alpha-beta alloys contain one or more of the α or β stabilizers. These alloys retain more β after final heat treatment than the near α alloys and can be strengthened by solution treating and aging, although they are generally used in the annealed condition. Solution treatment is usually performed high in the α/β field followed by aging at lower temperature to precipitate α, giving a mixture of fine α in an α/β matrix. The solution treating and aging can increase the strength of these alloys by up to 80% [17]. Alloys with low amounts of β stabilizers have poor hardenability and must be rapidly quenched for subsequent strengthening. A few important α/β alloys include: Ti-6Al-4V, Ti-3Al-2.5V, Ti-5Al-2Sn-2Zr-2Mo-2Cr-0.25Si, Ti-6Al-2Sn-4Zr-6Mo and Ti-6Al-6V-2-Sn.

c. Beta alloys have more β stabilizers content and less α stabilizer than α/β alloys. These alloys have high hardenability with the β phase retained completely during air cooling of thin sections, and water quenching of thick sections. Beta alloys have good forgeability and good cold formability in the solution-treated condition. After solution treatment, aging is performed to transform some β phase to α. The strength level of these alloys is greater than α/β alloys, as a result of the finely dispersed α particles in the β phase [17,18]. These alloys have relatively higher densities and generally lower creep strengths than α/β alloys. The fracture toughness of aged β alloys at a given strength level is generally higher than that of an aged α/β alloy, although crack growth rate can be faster. A few commercially available β alloys include: Ti-3Al-8V-6Cr-4Mo-4Zr, Ti-4.5Sn-6Zr-11.5Mo, Ti-8Mo-8V-2Fe-3Al and Ti-13V-11Cr-3Al.

The properties of titanium alloys are primarily determined by the arrangement, volume fraction and individual properties of the two phases. Table 1.1 illustrates the essential differences between the three alloy classes.

Table 1.1 *Properties of α, (α+β) and β titanium alloys [19]*

	α	α+β	β
Density	+	+	-
Strength	-	+	++
Ductility	-/+	+	+/-
Fracture toughness	+	-/+	+/-
Creep resistance	+	+/-	-
Corrosion behavior	++	+	+/-
Oxidation behavior	++	+/-	-
Weldability	+	+/-	-

++ - very good

+ - good

+/- - satisfactory

-/+ - unsatisfactory

- - poor

1.1.2 Properties of titanium and titanium alloys

1.1.2.1 General properties

Titanium is a light, strong, nonmagnetic metal with low density (approximately 60% of the density of steel). Titanium is as strong as steel, but lighter and it is heavier than aluminium, but twice as strong [19].

The properties and characteristics of titanium that are important to design engineers are enlisted below:

- superior strength to weight ratio – the density of current commercial titanium ranges between 4420 kg/m^3 and 4850 Kg/m^3; yield strengths range from 172 MPa for commercially pure (CP) Grade1 to above 1.380 MPa for heat treated alloys,

- excellent corrosion resistance – titanium is immune to corrosive attack by salt water or marine atmospheres; it also exhibits exceptional resistance to a broad range of acids, alkaline, natural waters and industrial chemicals,
- high heat transfer efficiency – in service conditions the heat transfer properties of titanium approximate to those of brass and copper-nickel.

The physical and mechanical properties of titanium are presented in table 1.2.

Table 1.2 *Physical and mechanical properties of titanium alloys*

Property	Value
Crystal structure	α: close-packed hexagonal ≤ 1156 K
	β: body-centered cubic ≥ 1156 K
Colour	Dark grey
Density	4,506 g/cm^3
Melting point	1668°C
Boiling point	3287°C
Specific heat	0.518 J/kgK
Thermal conductivity	21 W/mK
Heat of fusion	440 kJ/kg
Heat of vaporization	9.83 MJ/kg
Specific gravity	4.5
Hardness	HRB 70-74
Tensile strength	241 GPa
Young's modulus	116 GPa
Poisson's ratio	0.32
Coefficient of friction	0.8 at 40 m/min
	0.68 at 300 m/min
Specific resistance	0.554 μΩm
Coefficient of thermal expansion	8.64*10^{-6}/K
Electrical conductivity	3% IACS* (copper 100%)
Electronegativity	1.5 Pauling's ratio
Temperature coefficient of electrical resistance	0.0026/K
Magnetic susceptibility	180*10^{-6}
Machinability rating	40

IACS – International Annealed Copper Standard

1.1.2.2 Corrosion behavior of titanium and its alloys

The excellent corrosion resistance of titanium alloys results from the formation of very stable, continuous, highly adherent, and protective oxide films on the surface. Because titanium metal is highly reactive and has an extremely high affinity for oxygen, these beneficial surface oxide films form spontaneously and instantly when fresh metal surfaces are exposed to air and/or moisture. In fact, a damaged oxide film can generally re-heal itself instantaneously if at least traces of oxygen or water are present in the environment [17,20]. However, anhydrous conditions in the absence of a source of oxygen may result in titanium corrosion, because the protective film may not be regenerated if damaged.

The nature, composition, and thickness of the protective surface oxides that form on titanium alloys depend on environmental conditions. In most aqueous environments, the oxide is typically TiO_2, but may consist of mixtures of other titanium oxides, including Ti_2O_3, and TiO [12]. High-temperature oxidation tends to promote the formation of the chemically resistant, highly crystalline form of TiO_2, known as rutile, whereas lower temperatures often generate the more amorphous form of TiO, anatase, or a mixture of rutile and anatase.

The highly adherent oxide film that forms on the surface of titanium and its alloys offers an exceptional resistance to a broad range of acids and alkalis, as well as natural and salt and polluted waters [21].

Although these naturally formed films are typically less than 10 nm thick and are invisible to the eye, the TiO_2 oxide is highly chemically resistant and is attacked by very few substances. Some of the substances to which titanium exhibits resistance are hot, concentrated HCl, H_2SO_4, NaOH, and (most notably) HF. This thin surface oxide is also a highly effective barrier to hydrogen.

Some of the corrosive environments in which titanium surfaces prove resistance are presented in table 1.3.

Table 1.3 *Corrosive environments where titanium's oxide film provides resistance*

Chlorine and other halides	• fully resistant to chlorine and its compounds • fully resistant to solutions of chlorites hypochlorites, perchlorates and chloride dioxide • resistant to moist bromine gas, iodine and their compounds
Water	• immune to corrosion in all natural, sea, polluted waters • immune to microbiologically influenced corrosion (MIC)
Oxidizing mineral acids	• highly resistant to nitric, chromic, perchloric and hypochlorous acids
Gases	• corrosion resistant to sulphur dioxide, ammonium, carbon dioxide, hydrogen sulphide and nitrogen
Inorganic salt solution	• highly resistant to chlorides of calcium, cooper, iron, ammonia, manganese and nickel • highly resistant to bromide salts • highly resistant to sulfides, sulfates, carbonates, nitrates, chlorates and hypochlorates
Organic acids	• generally very resistant to acetic, terephthalic, adipic, citric, formic, lactic, stearic, tartaric and tannic acids
Organic chemicals	• corrosion resistant in organic process streams of alcohols, aldehydes, esters, ketones and hydrocarbons with air or moisture
Alkaline media	• low corrosion rates in hydroxides of sodium, potassium, calcium, magnesium and ammonia

1.1.3 Applications

Because of their high strength to weight ratio, excellent fracture related properties and superior environmental resistance titanium alloys are the material choice in many aerospace and terrestrial applications [22].

Selection of titanium for both airframes and engines is based upon its specific properties: weight reduction (which translates to fuel economy) coupled with outstanding corrosion resistance and mechanical properties. Highly efficient gas turbine engines are possible through the use of titanium alloy components such as fan blades, compressor blades, rotors, discs, hubs and numerous non-rotor parts like inlet guide vanes. Titanium is the most common material for engine parts that operate up to 593°C because of its strength and ability to tolerate the temperatures in the cooler parts of the engine.

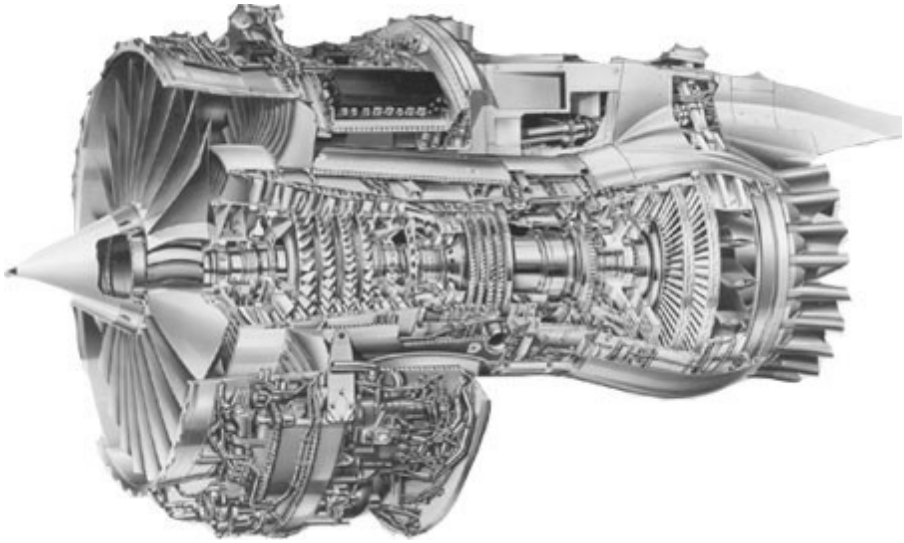

Figure 1.3 *Titanium jet engine (frame, fan blades, shafts, discs, etc.) [http://people.bath.ac.uk]*

Despite higher initial cost, primary components of aircraft landing gear are increasingly manufactured from forged titanium alloys. Their higher up front cost pays off over the long term as high-strength steels typically need to be replaced at least once in aircraft's lifetime due to their susceptibility to stress corrosion.

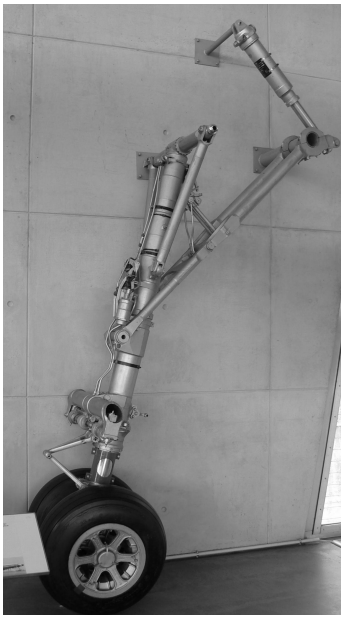

Figure 1.4 *Titanium landing gear [http://forums.pelicanparts.com]*

Figure 1.5 *Satellite fuel tank [http://www.psi-pci.com]*

Fuel and satellite tanks are regarded as a standard application for titanium alloys. Titanium's low weight, high strength and long term chemical compatibility with fuel give titanium alloys an advantage over high-strength steels [18].

An area of expansion for titanium is in automobiles [22,23]. Titanium and its alloys have come to be actively used for various parts of the general mass-produced cars due to the increasing demand for lightweight parts and thanks to remarkable progress made in the manufacturing technology of low-cost titanium [24-26]. The application of titanium started with components for large-sized motorcycles, but nowadays we have become familiar with exhaust pipes, engine valves, connecting rods, springs and other titanium parts for the motorcycle and automobile market.

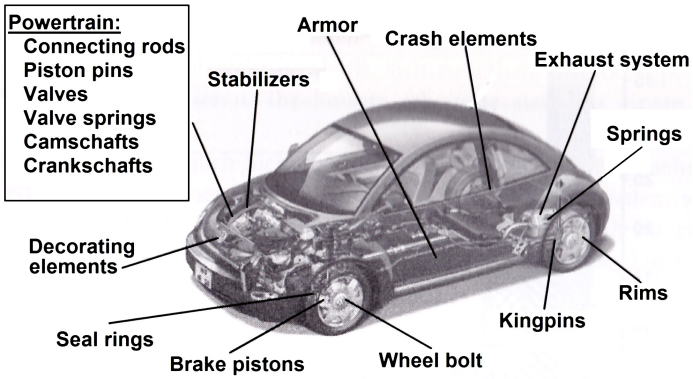

Figure 1.6 *Titanium in automotive applications [25]*

Recently, the attractive ballistic behavior of titanium has led to use in military armored vehicles and other military applications such as bulkheads, missiles, tank center guides, fuselage panels and helicopter rotor heads.

Figure 1.7 *Military applications of titanium (a. helicopter rotor head, b. bulkhead, c. tank center guides [http://www.dynamettechnology.com])*

Other applications fields in which titanium finds increasingly use is sports (baseball bats, golf “woods”, ice skates, hubs) and medicine (dental and orthopedic implants, instruments).

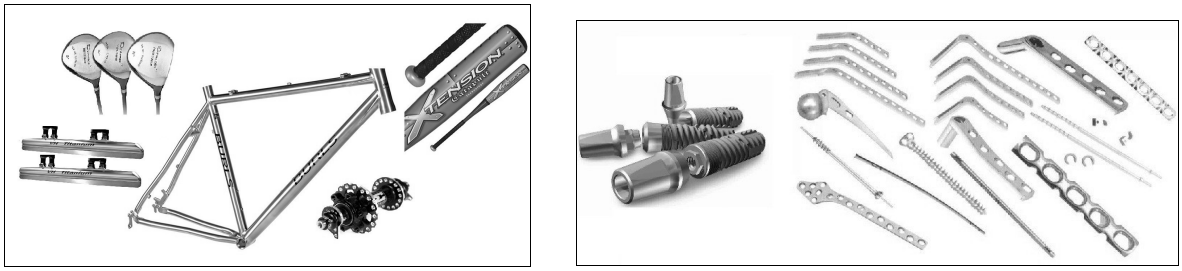

Figure 1.8*: Titanium in sports and medical application*

1.1.4 Limitations of titanium and its alloys

As described earlier, titanium alloys offer an attractive combination of high specific mechanical properties. They also have high toughness and corrosion resistance, making them useful materials for many industrial applications. However, these alloys have poor fretting fatigue resistance and poor tribological properties [27].

The poor wear resistance of titanium is caused by its low c/a ratio as a hexagonal close-packed metal. The slip systems produce relatively low shear strengths and a high coefficient of friction [19,28,29].

The essential features of the three crystal structures pertinent to metals are summarized in table 1.4. The ease of plastic deformation increases from the hexagonal close pack (hcp) lattice to the body-centered cubic (bcc) to the face centered cubic (fcc) lattice. Generally the number of slip systems – which is equivalent to the number of dislocation glide opportunities in a crystal lattice – is only 3 for the (hcp) structure while it is 12 for the (bcc) lattice. The number of slip systems is determined by the number of slip planes multiplied by the number of slip directions. These planes and directions of highly dense packed atoms are energetically most favorable for plastic deformation.

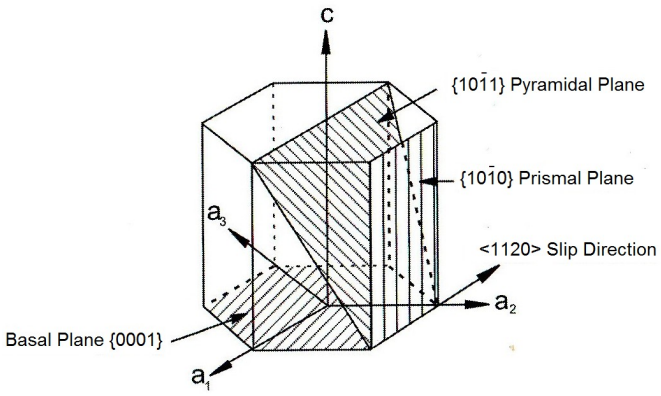

Figure 1.9 *Slip systems in (hcp) structure [19]*

The denser slip planes are packed with atoms, the easier dislocations can glide. Therefore, a slip plane in the (hcp) lattice with a packing density of 91% should be superior to a slip plane in the (bcc) lattice with a packing density of only 83%. However, the energy needed for plastic deformation is also directly dependent on the length of the

minimal slip path. For (hcp) lattice structures this minimum slip path corresponds to b_{min}=1*a, while for the (bcc) structures b_{min}=0.87*a, where a is the lattice parameter of the respective unit cell [19].

Table 1.4 *Crystal structure characteristics [19]*

Crystal system	A	C_N	P	Slip planes Slip direction		Slip systems	D_{SP}	b_{min}/a
				Indices	No.			
hex	6	12	74%	{0001} (1120)	1 3	1*3=3	≈ 91%	1
bcc	2	8	68%	{110} <111>	6 2	6*2=12	≈ 83%	≈ 0,87
fcc	4	12	74%	{111} <110>	4 3	4*3=12	≈ 91%	≈ 0,71

A – number of atoms per elementary cell

C_N – coordination number (adjacent atoms)

P – packing density of the lattice

D_{SP} – density of the slip plane

b_{min}/a – minimum slip path

In α titanium the lattice parameters of the hexagonal close pack crystal structure are a=0.295 nm and c=0.468 nm, giving a c/a ratio of 1.587. For an ideally close packed hexagonal lattice the c/a ratio is 1.633. The insertion of interstitially dissolved atoms in the (hcp) lattice, e.g. C, N or O, or the incorporation of substitutional atoms with smaller atomic radii that titanium, e.g. Al, slightly increases the c/a ratio of the α titanium. The lattice parameter of (bcc) titanium at 900°C is a=0.332 nm.

Compared to an ideally packed hexagonal crystal structure the reduced c/a ratio of α titanium leads to a larger spacing between prism planes. This causes the packing density of the prism plane to increase relative to the basal plane and thus favoring slip on prism planes rather then on basal plane [28]. The three active slip systems in α titanium are presented in figure 1.9.

1.2 Friction and Wear

In industrialized societies there is a growing need to reduce or control friction and wear for several reasons, such as to extend the lifetime of machinery, to make engines and devices more efficient, to conserve scarce material resources, save energy and improve safety [30].

A typical metallic surface for engineering purposes is not completely flat at the microscopic level. At high magnification, even the best polished surface will show ridges and valleys, asperities, and depressions. The height difference from the bottom to the top of a hill is typically 0,1 to 3 μm. When one surface is placed upon another, the first contact between the surfaces will take place at the top points of the highest peaks of the surfaces [31]. This causes material breakage, which under the influence of different parameters leads to friction and wear.

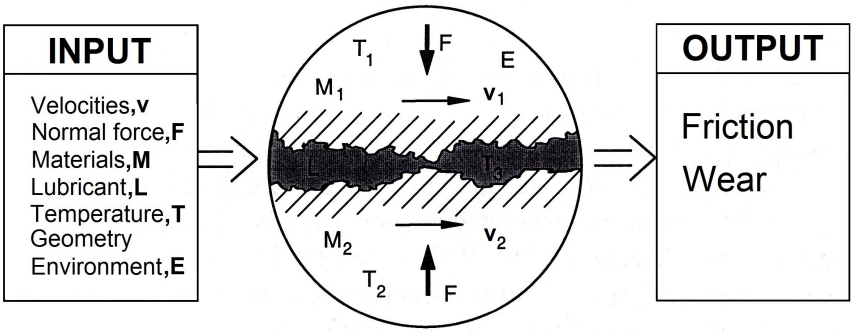

Figure 1.10 *Several material, contact conditions and environmental parameters which control friction and wear [30]*

1.2.1 Friction

Friction is the tangential resistance to movement of one body over another found in relative motion. The bodies in question may be two solids (solid friction), a gas and a solid (aerodynamic friction) or a liquid and a solid (liquid friction).

Friction is commonly represented by the friction coefficient, for which the symbols μ or f are generally are used. The friction coefficient is the ratio between the friction force, F, and the load, N:

$$\mu = \frac{F}{N} \qquad \text{(Eq. 1.1)}$$

In moving machinery, friction is responsible for dissipation and loss of energy. The energy lost to friction is an energy input that must continually be provided in order to maintain the sliding motion. This energy is dissipated in the system, primarily as heat- which may have to be removed by cooling to avoid damage and may limit the conditions under which the machinery can be operated. Some of the energy is dissipated in various deformation processes, which result in wear of the sliding surfaces and their eventual degradation to the point where replacement of whole components becomes necessary.

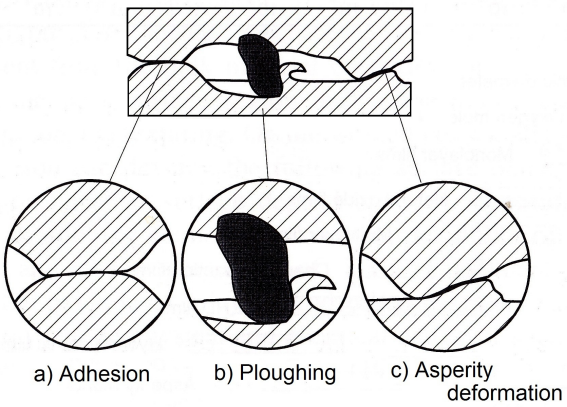

Figure 1.11 *The three components of sliding friction [31]*

Traditionally, the mechanism of friction in sliding contacts has been explained by the adhesional effect between surface asperities. This concept explains that when two asperities are forced into contact they will weld together due to the adhesion between the two materials (fig. 1.11a). When one of the bodies is moved in a tangential direction the micro welded joints will break, their shear causing the resistance to motion [32]. During sliding, new micro weld joints are formed and broken continuously.

1.2.1.1 Friction mechanisms

Some concepts say that the effect of friction can be divided into three basic mechanisms, one due to asperity deformation, one due to adhesion and one due to ploughing (fig. 1.11b) [33]. On the basis of crossed-cylinder experiments carried out, the following typical values for the three components of the friction coefficient were obtained:

- Friction due to asperity deformation, $\mu_d = 0 – 0.43$. It appears that asperity deformation is responsible for the static coefficient of friction. Once the original asperities have been deformed, asperity interlocking cannot take place.

- Friction due to adhesion, $\mu_a = 0 – 0.4$. The low value is for a well lubricated surface. The high value is for identical metals sliding against each other without any contamination or oxide layers.

- Friction due to ploughing, $\mu_p = 0 – 0.4$. The low value is obtained either when wear particles are totally absent from the interface or when a soft surface slides against a hard surface with a mirror finish. The high value is associated to two identical metals sliding against each other with deep penetration of wear particles.

1.2.1.2 Stages in friction mechanisms

A sliding contact goes through several stages of different frictional mechanisms in the running-in period before the steady state period is reached [33]. The experimentally observed stages of friction are shown in figure 1.12.

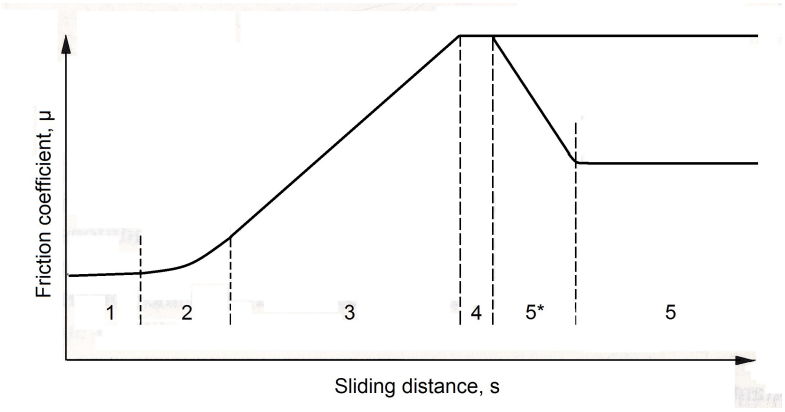

Figure 1.12 *The six stages of friction mechanisms [30]*

Stage 1. At the first stage of movement the frictional force is largely a result of ploughing of the surface by asperities. Because of surface contamination, adhesion does not play any significant role but asperity deformation takes place and affects the static coefficient of friction. The surface is easily polished. Consequently, the friction coefficient in the initial stage is largely independent of material combinations, surface and environmental conditions.

Stage 2. The polishing process from the previous stage has removed surface contamination and elements of bare surface will appear, resulting in a slow increase in the coefficient of friction due to increased adhesion.

Stage 3. The coefficient of friction increases due to a rapid increase of particles entrapped between the sliding surfaces. The asperity deformation continues and the adhesion effect increases due to larger interfacial areas. Some of the material particles are trapped between surfaces, causing ploughing. If the wear particles are entrapped between metallic surfaces with equal hardness, they will penetrate into both surfaces, preventing any slippage between the particle and the surface, resulting in maximum

ploughing friction.

Stage 4. The number of particles entrapped between the surfaces remains constant because the number of particles entering the interface is the same as the number of particles leaving the interface. When two identical materials slide against each other or when the mechanisms from stage 5* are not significant, then stage 4 could represent a steady-state friction.

*Stage 5**. In some cases, such as when a very hard stationary slider is slid against a soft specimen, the asperities of the hard surface are gradually removed, creating a mirror-like smooth surface. The frictional force decreases, due to the decrease of asperity deformation and ploughing, because the particles cannot anchor so easily to a polished surface.

Stage 5. The coefficient of friction slowly levels off and reaches a steady-state value as the hard surface becomes mirror smooth to a maximum extent and the softer surface also acquires a mirror finish.

1.2.1.3 Friction of metals

It was demonstrated that the adhesion between two surfaces depends on the degree of matching between the crystal planes [34]. The highest adhesion and friction forces are observed for matched planes of the same material. Lower values are found for matched planes of materials that are different but that have similar lattice dimensions and also show some mutual solubility. Still lower values are found when the two materials are insoluble in each other. For example, values of μ = 0,21 for the self-mated couple copper-copper; μ = 0,4 for the closely fitting planes of the mutually soluble couple copper-nickel; μ = 0,2 for copper-cobalt, where solubility exists but where one metal is face centered cubic (fcc) and the other is hexagonal close-packed (hcp); and last μ = 0,14 for copper-tungsten, where no bulk solubility exists were quoted.

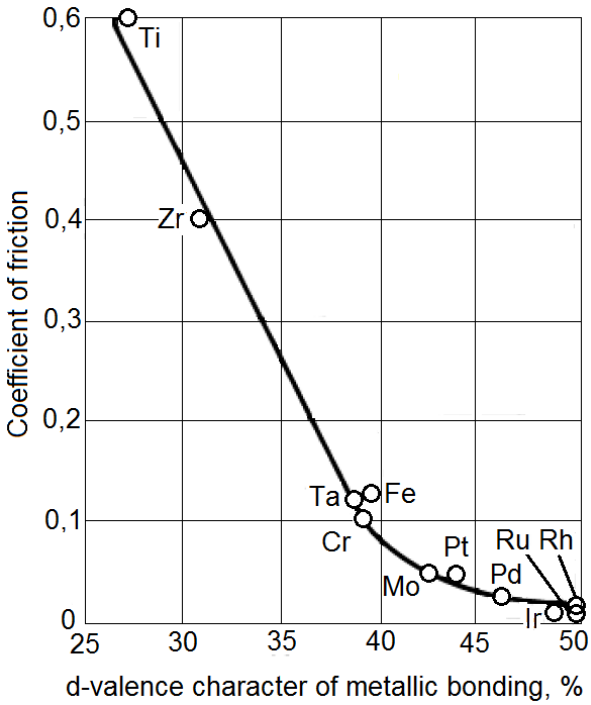

Figure 1.13 *Friction coefficients of metals in contact with themselves, at very low loads and sliding velocity [35]*

Adhesive friction may also be related to other fundamental properties. One such property is the degree of *d*-valence bond character of the transition metals (fig. 1.13) [34]. Titanium, which has a very high degree of bond unsaturation, shows a strong tendency to bond with almost anything, such as a matching titanium surface or a nonmetal. As the degree of *d* bond character increases, the friction coefficient decreases-possibly because the greater the degree of bonding of a metal to itself, the less the bonding across the interface [35].

Because plastic deformation is associated with friction, in most cases it is expected that the flow stress of the material will affect μ. This is confirmed, for example, by results of friction tests with changing temperature for metals and alloys that undergo phase transformations. Figure 1.14 illustrates this for cobalt, which is hcp below 417 °C (783 °F) and fcc above this temperature. Below the transition temperature, μ = 0.35 for cobalt, because the basal hexagonal planes develop a preferred orientation, slips takes place between them, and there is little stain hardening. In this range, cobalt behaves like a solid lubricant. For the fcc structure above the transition temperature, μ rises

rapidly, possibly because of the significant work hardening of this structure.

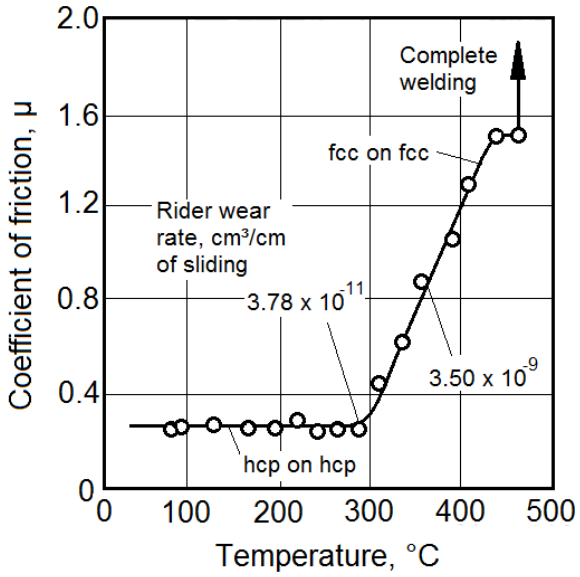

Figure 1.14 *Friction coefficient versus temperature as a function of phase transformation for cobalt on cobalt [35]*

Similar behavior has been observed for thallium, which also undergoes an hcp-fcc transformation. Not all hcp structures show low friction, however. A good example of this is titanium (fig 1.13). It appears that low friction occurs only for those structures that deform exclusively in the basal plane and that show low work hardening because the basal planes slide readily over one another. For lanthanum, which has three crystalline phases, the friction coefficients are in the order: $\mu_{hcp} < \mu_{fcc} < \mu_{bcc}$ (bcc, body-centered cubic). Tin and tin-copper solid solutions show the opposite behavior with temperature: there is a drop in as the phase transformation from gray tin to white tin takes place upon heating 13 °C (55 °F). In this case, the behavior can also explained on the basis of the deformation properties of the two crystal structures. The high friction is exhibited by the low-temperature phase (gray tin). It has a diamond-type structure and exhibits a high degree of work hardening, while the white tin has a body-centered tetragonal (bct) structure that deforms more readily and that shows less work hardening and consequently lower friction [35].

One can say that adhesion is a very important component of friction in a vacuum. In extreme cases, it may lead to complete seizure of the two surfaces. The amount of adhesion depends on the nature of the surfaces, on their affinity for each other, and on their affinity for any adsorbates that may be present in the vacuum. The friction coefficient also depends on the flow stress properties of the near-surface material, because this is where deformation to accommodate the sliding most often takes place. In contrast, the effect of adhesion on friction under ambient conditions is more controversial, because it is not as unequivocally demonstrated.

1.2.2 Wear

Wear has been defined as the removal of material from solid surfaces as a result of one surface moving over another. Thus both friction and wear are simultaneously the results of the same tribological contact process that takes place between two moving surfaces. However, their interrelationship is not well understood. It is common to find that low friction corresponds to low wear and high friction to high wear, as shown in figure 1.15, but this is not a general rule [36].

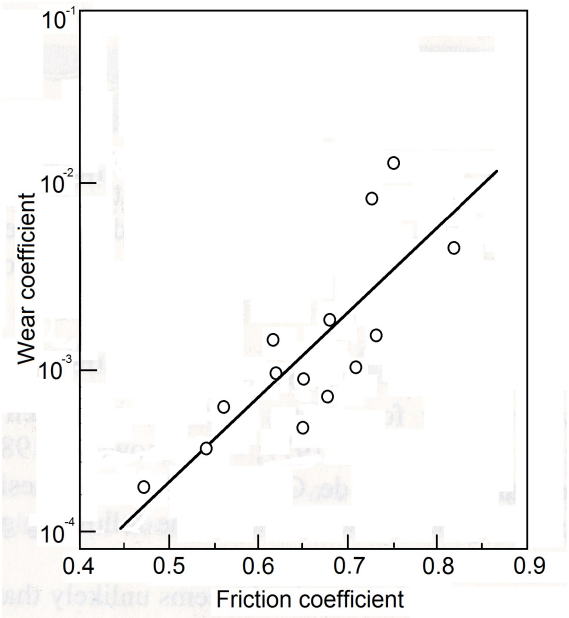

Figure 1.15 *Wear coefficient as a function of friction [36]*

Wear has been found to be dependent on the crystal structure and orientation [37]. It was shown that cubic metals wear at about twice the rate of hexagonal metals, which was attributed to the lower work-hardening rate of the hexagonal metals. In addition, single crystal wear studies, consisting in scratching body-centered cubic (bcc) and face-centered cubic (fcc) metals with a prepared surface on the (001) plane, revealed wider scratch width, which implied higher wear, along the <100> than the <110>direction [38].

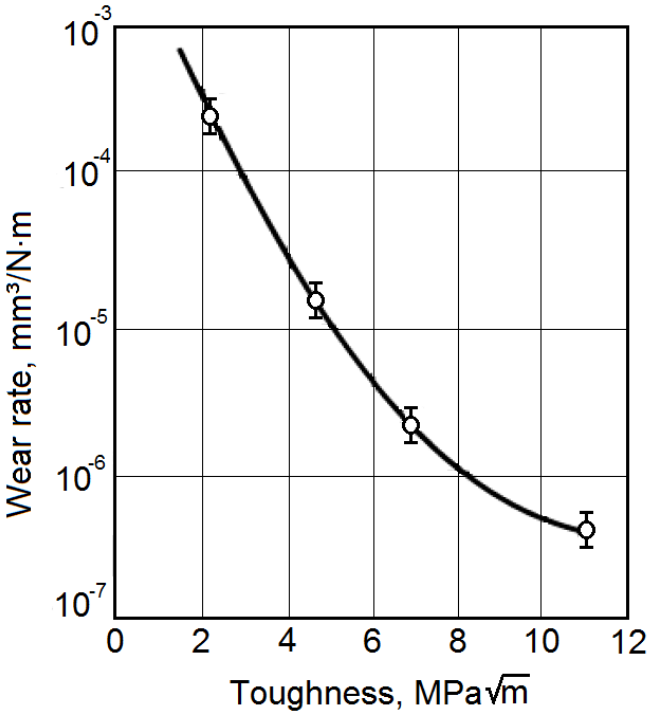

Figure 1.16 *Wear rate of zirconium oxide as function of fracture toughness [39]*

Additionally, it has been found that fracture toughness, K_{Ic}, of the material is important in determining wear for ceramics (fig. 1.16). Studies concerning a series of zirconia samples with constant hardness, but varying toughness showed that the wear decreased with the fourth power of the toughness [39].

1.2.2.1 Stages of wear

Under normal operating parameters, the property changes during usage normally occur in three different stages as follows:

- Primary or early stage or run-in period, where rate of change can be high;
- Secondary or mid-age process where a steady rate of aging process is maintained. Most of the useful or working life of the component is comprised in this stage;
- Tertiary or old-age stage, where a high rate of aging leads to rapid failure

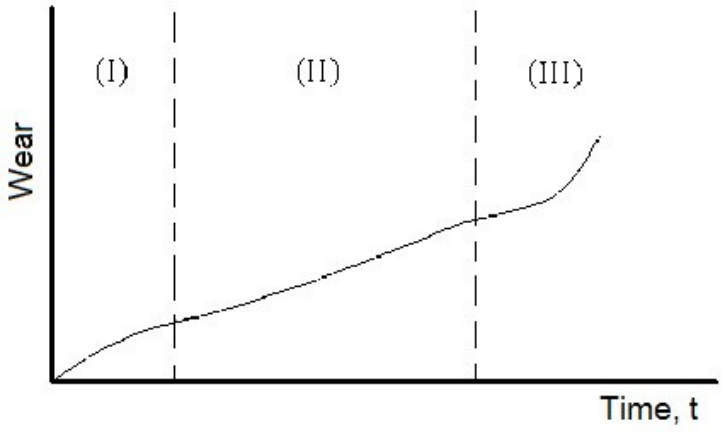

Figure 1.17 *Stages of wear*

With increasing severity of environmental conditions such as higher temperatures, strain rates, stress and sliding velocities, the secondary stage is shortened and the primary stage tends to merge with the tertiary stage, thus drastically reducing the working life of components [40].

1.2.2.2 Types of wear

The way in which the removal of material from the surface takes place is described by several wear mechanisms. There is, however, still no general agreement about the classification of wear mechanisms and modes. The mostly met classification of wear types distinguishes four mechanisms: adhesive, abrasive, fatigue and chemical.

Adhesive wear. When asperities of one surface come in contact with asperities of the counterface they adhere strongly to each other and form asperity junctions as shown in figure 1.18 . Relative tangential motion of the surfaces causes separation in the bulk of the softer asperities and material is removed. Adhesion has been confirmed to be a major contributor to sliding resistance (friction).

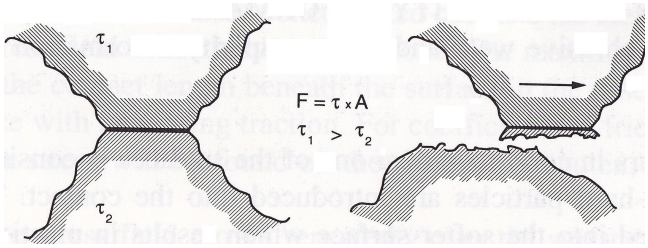

Figure 1.18 *Adhesive wear mechanism [30]*

Adhesive wear is the most common form of wear and is commonly encountered in conjunction with lubricant failures. It is commonly referred to as welding wear due to the exhibited surface characteristics [41]. In engineering science, adhesive wear is usually referred to as galling and is common in sheet metal forming (SMF) and other industrial applications.

The tendency of contacting surfaces to adhere arises from the attractive forces that exist between the surface atoms of the two materials. The type and mechanism of attraction varies between different materials. Most solids will adhere on contact to some extent, however, oxidation films and contaminants naturally occurring, generally suppress adhesion [42].

Abrasive wear occurs in contacts where one of the surfaces is considerably harder or where hard particles are introduced in the contact. The harder surface asperities are pressed into the softer surface which results in a plastic flow of the softer material around the harder one. When the harder surface moves tangentially, ploughing and removal of the softer materials takes place.

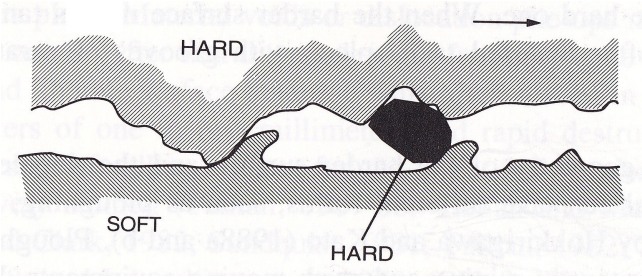

Figure 1.19 *Abrasive wear mechanism [30]*

Abrasive wear is commonly classified according to the type of contact and the contact environment [43]. The type of contact determines the mode of abrasive wear. The two modes of abrasive wear are known as *two-body* and *three-body* abrasive wear. Two-body wear occurs when the hard particles, are rigidly mounted or adhere to a surface, when they remove the material from the surface. Three-body wear occurs when the particles are not constrained, and are free to roll and slide down a surface. The contact environment determines whether the wear is classified as open or closed [44]. An open contact environment occurs when the surfaces are sufficiently displaced to be independent of one another. Two-body systems typically experience from 10 to 1000 times as much loss as three-body systems for a given load and path length of wear.

Abrasion is often further categorized as being low stress, high stress, or gouging. *Low-stress* abrasion occurs when the abrasive remains relatively intact, for example, when sanding wood with sandpaper. *High-stress* abrasion exists when abrasive particles are being crushed, for example, in a ball mill where both the grinding balls and the ore are down. In *gouging* abrasion, a relatively large abrasive will cut the material that is not fully work hardened by the process from the material of concern, for example, when rocks are crushed in jaw crusher.

Fatigue wear. Fatigue crack growth is a phenomenon which results from cyclic loading of a surface, at a stress level that the material can not sustain if repeated more times. Fatigue can form the origin for large scale cracking and liberation of surface material to form wear debris as shown in figure 1.20.

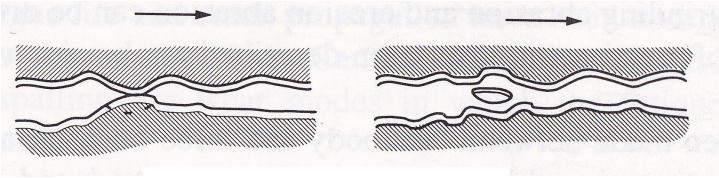

Figure 1.20 *Fatigue wear mechanism [30]*

Fatigue cracks may also be initiated where the contacting surfaces are under a very heavy normal load or where there is a static tensile stress in one of the surfaces. There are cases where the movement is not simply tangential, but is complicated by the normal force also oscillating to the extent that the surfaces lose contact in each cycle. This leads to a hammering effect, which is termed "impact fatigue." In this case, the phase relationship between the two motions can be an important factor.

Chemical wear is defined as the degradation of materials in which both corrosion and wear mechanisms are involved [42,45]. The combined effects of wear and corrosion can result in total material losses that are much greater than the additive effects of each process taken alone, which indicates synergism between the two processes. Rubbing, in combination with the chemical reactions in the contact results in the removal of material and wear debris formation. The rubbing action results in increased temperatures at the surface and creates surface cracks which are favorable for more chemical reactions to take place [35,40].

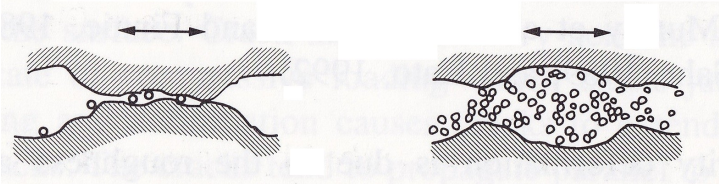

Figure 1.21 *Chemical wear mechanism [30]*

Oxidational wear is the most common chemical wear process. A thin layer of oxides will be formed on the top of metal surfaces. This is an important protecting layer because without it both the friction and wear in metal contacts would be extremely high. If this layer is continuously removed by a rubbing action and the formation of new layers is speeded up by a high humidity environment that can easily reach the contact, the result is a typical form of oxidational wear [46,47].

1.2.2.3 Wear rate

For design and material development purposes it is necessary to have some universal quantitative parameter for wear. To use the volume of removed material is neither useful nor illustrative because of the very different test conditions in use. The wear rate is illustrated as:

$$K = \frac{V}{L \cdot d} \text{ [10}^{-6}\text{ mm}^3\text{/Nm]} \qquad \text{(Eq. 1.2)}$$

where, V – worn volume, [mm³]
L – normal load, [N]
d – moved distance, [m]

Even if, from some aspects, this is not the ideal way of expressing wear, it has a wide support. There is also a clear physical argument for using the wear rate as defined above because it is the worn volume divided by the mechanical energy input into the contact. The contact energy input can be described as the product of the normal load, the velocity and the applied time, which again is the same as the product of load and distance found in the equation.

1.3 Surface engineering methods of titanium

Although titanium alloys offer attractive mechanical and physical properties, their surface properties are deficient, thus restricting the use of uncoated titanium alloys to nontribological applications [48]. To realize the full benefit of titanium alloys in friction and wear applications, surface modification treatments are required to effectively increase near-surface strength, thereby reducing the coefficient of friction and lowering the tendency for material transfer and adhesive wear.

Many surface treatments have been used to modify the tribological properties of titanium alloys. These treatments can be classified as ion implantation, thermo-chemical conversion treatments (oxidizing, nitriding, carburizing, borinizing, siliconizing), plating, laser surface treatments and sprayed coatings.

1.3.1 Ion implantation

The ion implantation process involves the acceleration of ions to a sufficiently high velocity so that they are able to penetrate the surface of the substrate material being implanted. The mean depth of penetration depends on the energy, the atomic number, the atomic masses of the implanted and the target species, and the angle of incidence. Industrial implanters are typically designed to accelerate the ions to energies of between 50 and 200 keV, resulting in implant layer thicknesses of up to several hundred nanometers.

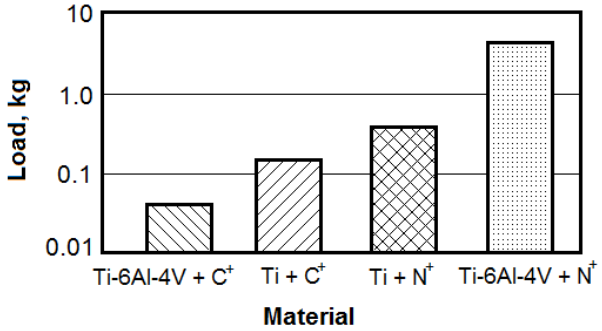

Figure 1.22 *Breakthrough load for titanium substrate – ion combinations [50]*

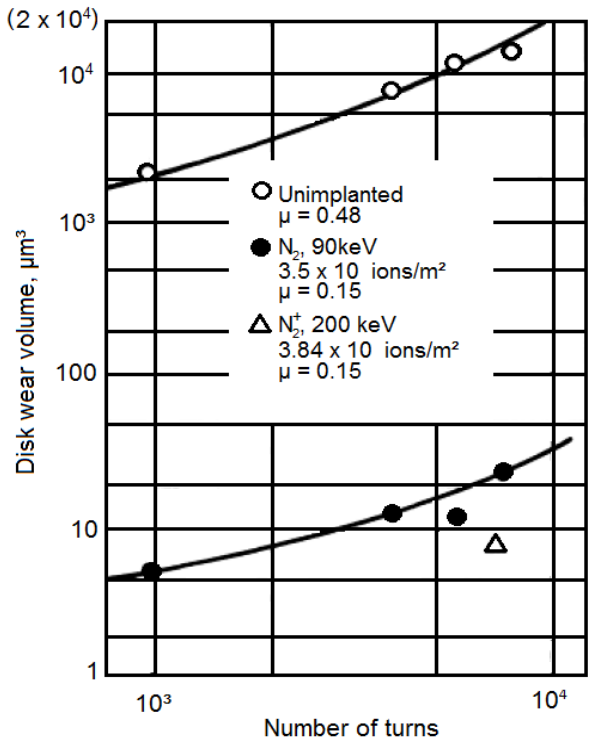

Figure 1.23 *Wear volume loss of untreated and nitrogen implanted Ti-6Al-4V [50]*

The most commonly implanted species are nitrogen and carbon, which may be noted from a review of the ion implantation of Ti-6Al-4V [49]. From pin-on-disk friction wear tests, much greater wear resistance has been shown (fig. 1.23) for nitrogen-implanted Ti-6Al-4V compared with untreated material [50]. Nitrogen or carbon implanted into pure titanium produces nearly equivalent results for breakthrough load to failure of the ion-implanted zones. In contrast, nitrogen implantation of higher hardness and higher-strength Ti-6Al-4V showed more effective than carbon implantation in increasing breakthrough load (fig. 1.22).

1.3.2 Thermo-chemical diffusion treatments

Diffusion treatments, as the name suggests, require sufficient time at temperature to allow significant atomic mobility to occur. The interstitial alloying elements boron, carbon, nitrogen and oxygen may all be thermochemically alloyed with titanium [51]. Nitriding and oxidizing are more useful from the hardening depth point of view, since solid-solution-hardened diffusion zones exist beneath the surface compound layers.

1.3.2.1 Nitriding

Nitriding of titanium and its alloys has been widely investigated and effectively used as a surface treatment for protection against wear. The wear resistance is imparted by a very favorable phase equilibrium relationship between the elements [52]. Nitrogen has a high solid solubility in α-Ti, and the strength increase effected by the interstitial nitrogen is significant (fig. 1.24).

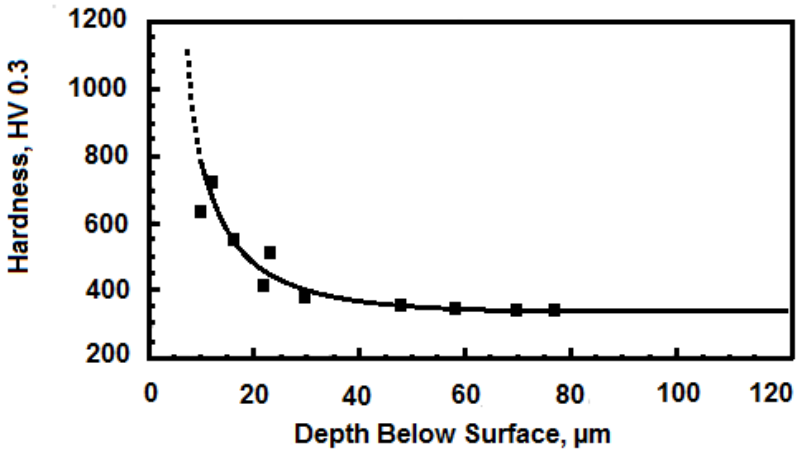

Figure 1.24 *Microhardness profile of plasma-nitrated Ti-6Al-4V [52]*

Nitriding produces a thin compound layer of TiN at the surface, above a thicker compound layer of Ti_2N, which is above a diffusion zone of nitrogen-strengthened titanium. Nitriding cannot be achieved in air because of the tendency of titanium to form TiO_2 in preference to either of the nitrides, but it can be achieved in a nitrogen gas atmosphere. Plasma, ion, or glow discharge nitriding has long been applied to ferrous

alloys, but the direct current plasma process is equally applicable to titanium-base materials [53]. Nitrogen, nitrogen-hydrogen, nitrogen-argon, or cracked ammonia may be used as the treatment gas. A typical hardness profile from plasma nitrided Ti-Al-4V is shown in fig. 1.24, in which the dashed line represents the hardness of the thin TiN and Ti_2N compound layers.

1.3.2.2 Oxidizing

Oxidizing of titanium and titanium alloys can be used to improve their tribological properties. Oxygen in solution in α- Ti produces significant strengthening of the material (fig. 1.25). A great deal of work has been devoted to the study of the oxidation of titanium and its alloys. It was observed when chemically pure titanium was heated in the range 850 to 1000 °C in air at a pressure between 10^{-3} and 10^{-2}mm Hg, the surface was effectively hardened. The process was commonly disregarded, however, because at a temperature high enough to achieve an appreciable hardening effect, a considerable amount of scale is also formed.

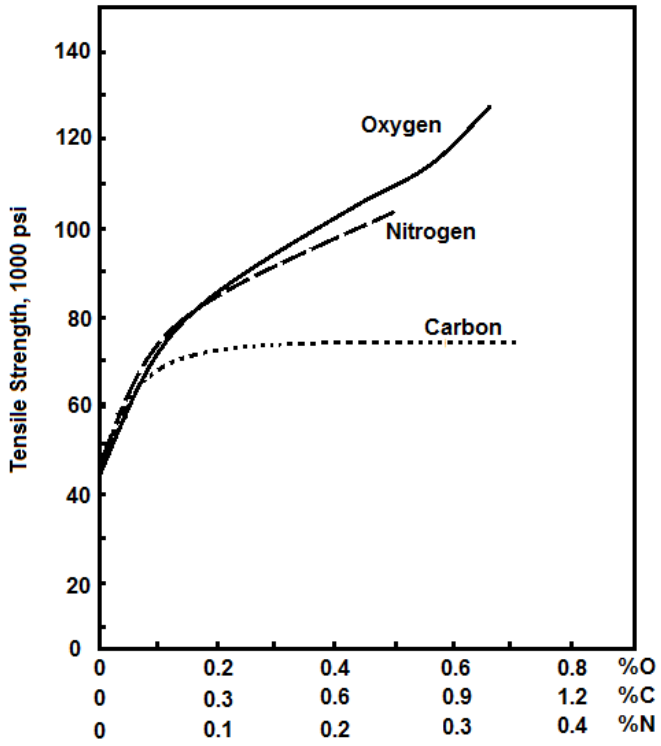

Figure 1.25 *Effect of interstitial alloying on the strength of titanium [54]*

Oxygen diffusion hardening (ODH) of Ti-6Al-7Nb alloys lead to surface with a gradation in hardness from the surface to a depth of 50 μm. The maximum hardness was 900 HV, compared with 360 HV for the untreated alloy. The corrosion resistance of the ODH-treated titanium alloy was equal to that of commercially pure titanium and untreated Ti-6Al-7Nb alloy [54].

1.3.2.3 Carburizing

Carburizing of titanium and titanium alloys may be achieved in non-oxidizing, carburizing environments. The phase equilibrium system for Ti-C differs from those for Ti-O and Ti-N in that there is very little solid solubility for carbon in titanium. Hence, compound layer formation of TiC may result, but there is no significant diffusion zone beneath the TiC. Carburizing is accomplished in pack processes using carbonaceous media such as calcium carbonate, or following evacuation and heating to 1050 °C, a carburizing gas is introduced and is used for cooling. Such operations were used for creating wear resistant engine valves.

1.3.2.4 Boronizing

Boronizing of titanium-base materials is similar to carburizing in that it results in the formation of an extremely hard compound layer with a negligible diffusion zone. TiB_2 is usually the outermost layer, although other borides are also formed. Wear resistance of boronized titanium has been studied, and in comparison with other surface treatments, it has performed very well in lightly loaded gear tests.

1.3.3 Plating

Plating of hard chromium and electroless nickel are the most widely used for wear-resistant applications. However, in wear situations the thin oxide layer present on titanium alloys can make satisfactory adhesion of these coatings to titanium substrates difficult to achieve. Measures taken to overcome this problem include [55]:

- Surface cleaning with an etchant, followed by rinsing in a water solution containing anions of cyanides, tartrate, citrate, and acetate complexing or chelating ions, followed by heat treatment;
- Cathodic cleaning of the surface, activation in stannous chloride:
- Chemical etching, immersion plating in a mixture of hydrofluoric acid, zinc sulfate, and sodium dichromate, followed by rinsing and conventional chromium plating;
- Oxide removal in hydrofluoric acid;
- Immersion in nitric acid and sodium citrate solution

Heat treatment has been successfully used for enhancement of adhesion of hard chromium plating of titanium alloys. A 700 °C temperature was used for the heat treatment, which resulted in a loss of hardness of the hard chromium, so a second chromium plating was applied to the initial, adherent, heat-treated chromium surface. Degradation in fatigue properties was improved by the use of shot peening. Components treated using this procedure have included oil seal collars, racing car flywheels, bearing housings, and pistons [56].

1.3.4 Laser surface treatments

Energy beam surface treatment for materials encompasses a wide range of processes, ranging from laser ablation at very high power densities to transformation hardening and annealing of metals and alloys at relatively low power densities. The only processes applied to titanium and titanium alloys to any significant extent are surface melting, surface cladding, and surface alloying techniques. These processes all involve the use of the energy beam to melt a surface layer in order to produce a conduction-limited melt profile. This molten region may vary in size from <1 μm, where gas alloying is used to mark surfaces, up to >400 μm, where hard surface layers are created for load-bearing, wear-resistant applications.

1.3.4.1 Laser surface melting

Surface melting using laser beams can homogenize a surface by melting all the microstructural components of the workpiece and allowing the relatively rapid resolidification of the melted region, distributing the phases on a much refined scale, or allowing the phases to solidify as new, metastable phases. In the extreme case, surface melting can be used as a rapid solidification tool by employing very high power densities and very rapid traverse speeds, thus relying on the efficient heat extraction from the melted region by the unheated bulk of the workpiece.

No significant changes in the overall mechanical properties occur with either commercially pure titanium or Ti-6Al-4V after laser surface melting. For example, columnar beta grains formed upon solidification of Ti-6Al-4V transform to martensite on further cooling [57].

1.3.4.2 Laser surface alloying

Laser surface alloying is achieved by changing the chemical composition of the substrate material during surface melting. Of the many possible alloying additions, nitrogen is the most widely researched. The object of the process is to harden the surface of the titanium alloy to a depth of 0.1 to 0.5 mm in order to improve its wear resistance [58]. By controlling the amount of nitrogen take-up by the melt pool, a range of solidification structures can be obtained that are usually described as predominantly TiN dendrites, nitrogen-rich α-Ti dendrites, or nitrogen-rich basket-weave. In fact, the most commonly mentioned structures contain TiN dendrites surrounded by nitrogen-rich α-Ti. The degree of alloying has a direct influence on the hardness of the alloyed volume, which can be simply controlled by changing the interaction time of the nitrogen with the melt pool or changing the nitriding potential of the alloying gas (fig. 1.26).

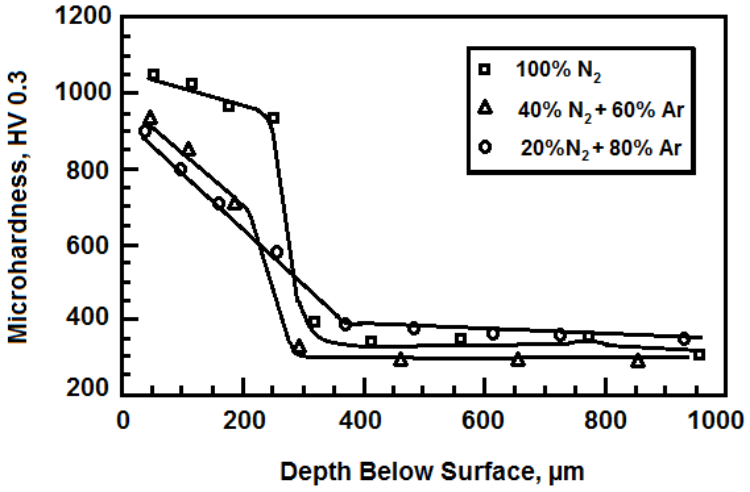

Figure 1.26 *Influence of the gas mixture on the hardness profile of laser-nitrated Ti-6Al-4V [58]*

The major concerns of this process are to avoid cracking, porosity formation, and unacceptably rough surfaces. Cracking is the major problem associated with laser-gas-nitrided titanium; it results from thermal stresses acting on the hard, relatively brittle phases arising from the process. The problem is ameliorated by using a mixture of argon and nitrogen in the treatment gas to produce an alloyed region of less than 650 HV and by preheating the substrate. With typical processing parameters, if the preheating temperature exceeds 300 °C, cracking can be completely eliminated [53,58].

Combinations of alloying elements have also been used to produce hardness increases and wear performance improvements. The most successful of these is the simultaneous addition of carbon and silicon in the form of silicon carbide. Surface hardness of 650 to 750 HV without any cracking were noticed. The microstructure comprises TiC dendrites surrounded by α-Ti dendrites, which contain some silicon and very fine precipitation of Ti_5Si_3. The advantage of this system is that the α-Ti component of the microstructure is relatively tough compared to that solidified after laser gas nitriding. A typical hardness profile obtained from this process is shown in figure 1.27.

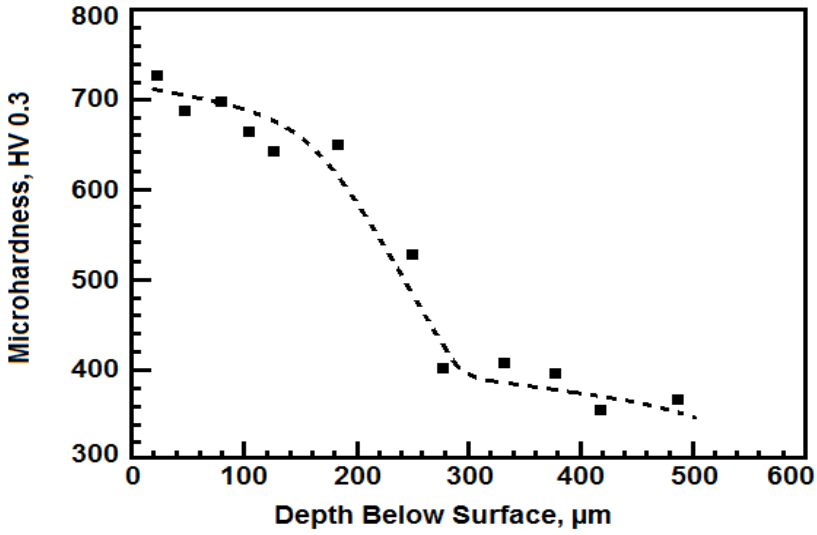

Figure 1.27 *Hardness profile of SiC laser alloyed Ti-6Al-4V [53]*

1.3.4.3 Laser cladding

Laser cladding involves the addition of a sacrificial layer on the surface of the substrate material, ideally with minimum dilution of the cladding by the substrate but with good adhesion of the clad. A prerequisite for good bonding of the clad to the substrate is similar coefficients of thermal expansion. For erosion resistance in gas turbines, TiC in a β-Ti alloy matrix has been clad on a Ti-6Al-4V substrate [59]. Experimental studies have shown that a dilution of 15% of the clad layer is associated with the highest hardness values [60].

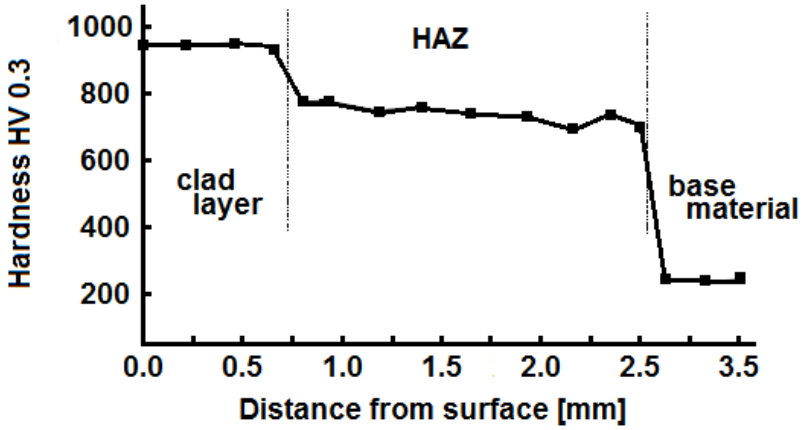

Figure 1.28 *Hardness of cobalt-based clad layer on Ti-6Al-4V [60]*

1.3.5 Thermally sprayed coatings

Thermal spray technology is emerging as an important processing tool for both surface protection and advanced materials forming. Despite the technology having been use for over 80 years, much of its advancement, driven by aerospace applications, has occurred in the past 5 years. Increased understanding of process/structure/property relationships has resulted in the growing application of thermal spray coating technology resulting in new processes; for example, Low -Pressure Plasma Spray, High Velocity Oxygen Fuel Spray, Vacuum Plasma Spray, Atmospheric Plasma Spray etc.

Thermal spray processes are particulate deposition methodologies that involve the deposition of the molten droplets of material on a substrate. The coating material is typically in the form of a powder. It is injected into a hot carrier gas and sprayed on the target substrate with a gun. This process can quickly deposit a wide variety of coatings. A shortcoming of traditional thermal spray technologies has been a limitation on the thickness and smoothness of the deposit [61]. The behavior of the injected powder, with respect to particle heat-up and acceleration greatly differs in the spraying techniques.

The quality of a thermal spraying coating, especially regarding porosity and substrate adhesion, is largely dependent upon the particle temperature and velocity at the moment of impact. In order to obtain dense and well-bonded coating, it is desirable that the particle be completely molten and that they travel at a high velocity when they impact the substrate.

The thermal spraying methods can be divided into three major groups:

- *flame spraying methods,* like High Velocity Oxygen-Fuel (HVOF), D-GUN method, wire flame spraying, etc.
- *plasma spraying methods,* such as Atmospheric Plasma Spray (APS), Vacuum Plasma Spray (VPS), Inert Gas Plasma Spraying (IGPS), etc
- *arc spraying methods*: wire arc spray.

The main difference between these techniques is that of the temperature of the powder melting. The temperature of a combustion flame is limited by the enthalpy of the chemical reaction that leads to the combustion of gases such as acetylene or propane in the presence of oxygen. While the flame velocity can be boosted in modern equipment (such as HVOF) to values near Mach 5, the temperature achievable are limited to approximately 3300 K. On the other hand, plasma jets have temperatures limited only by the amount of electrical energy supplied. Temperatures as high as 25000 K can be easily generated. Thus, flame spray including HVOF systems are used mainly for the spraying of materials with lower melting points such as metals or metal-ceramic composites, while spraying of ceramics with high melting points, such as alumina (2050°C), zirconia (2680°C) or boron nitride (2973°C) is the domain of plasma spray

systems [62,63].

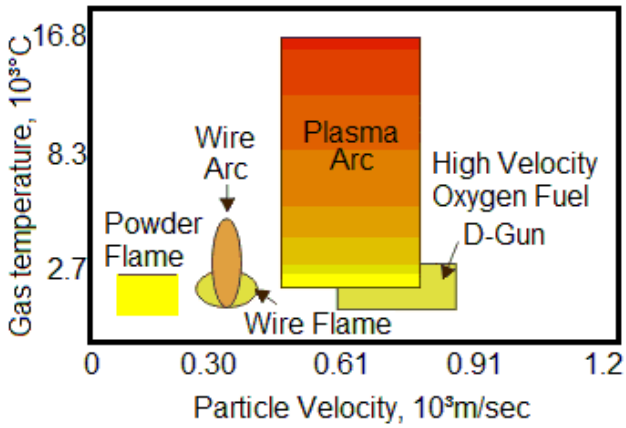

Figure 1.29 *Characteristics of flame and plasma spraying [www.kermetico.com]*

Chapter II

Experimental program

2.1 Materials

2.1.1 Titanium base material

TIKRUTAN RT 12 commercially pure titanium from ThyssenKrupp Titanium was used as substrate material. The chemical composition of TIKRUTAN RT 12 is presented in table 2.1.

Table 2.1 *Chemical composition of TIKRUTAN RT 12*

Element	C	H	Fe	N	O	Ti
weight %	< 0,06	< 0,013	< 0,15	<0,05	<0,12	> 99,607

2.1.2 Powder material

Two types of powder were used for the experiments: a boron nitride powder in aluminium-silicon matrix Al8Si20BN from SulzerMetco and a tungsten carbide powder in cobalt-chrome matrix WC-CoCr 86 10 4 from Thermico GmbH & Co.

2.1.2.1 Al8Si20BN powder

The particle size distribution of the Al8Si20BN powder is illustrated in figure 2.1.

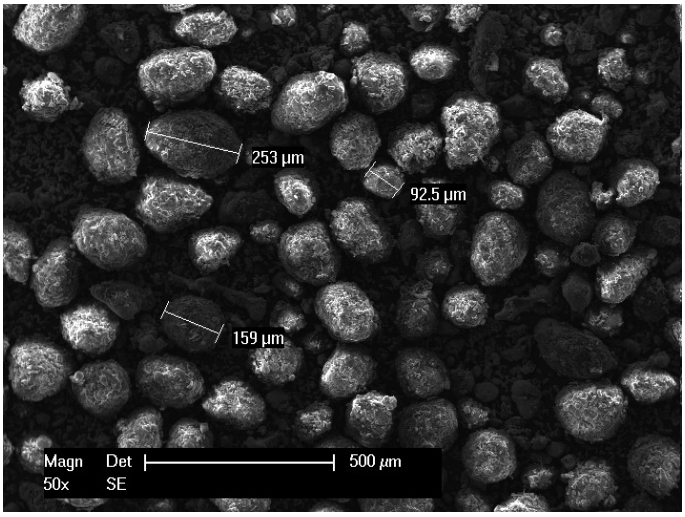

Figure 2.1 *SEM micrograph of the Al8Si20BN powder*

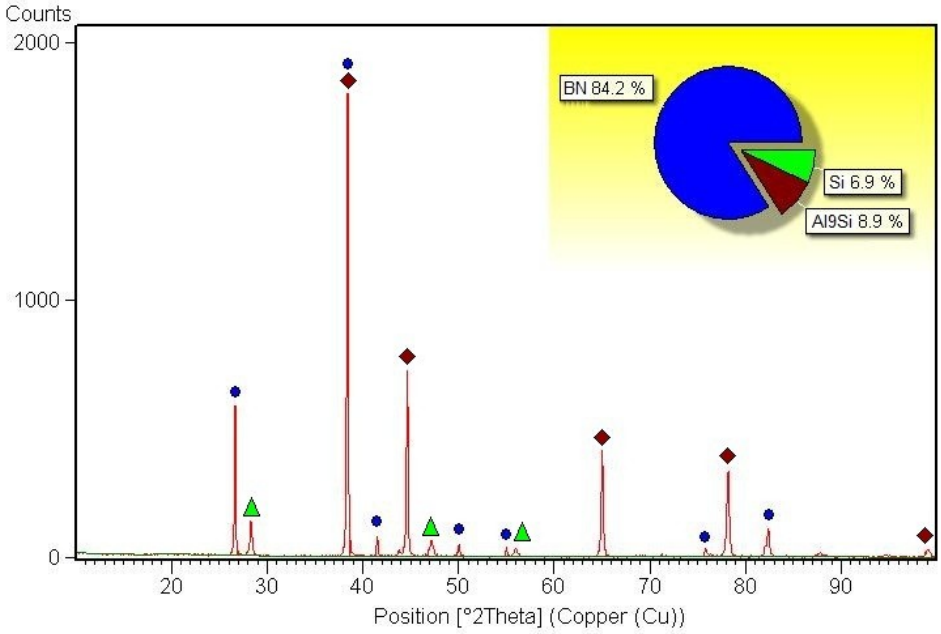

Figure 2.2 *X-ray diffraction pattern of the Al8Si20BN powder*

After performing X-ray diffraction on the powder sample, boron nitride (BN), aluminium-silicon Al_9Si and silicon (Si) could be identified.

2.1.2.2 WC-CoCr 86 10 4 powder

The SEM micrograph in figure 2.3 illustrates the grain size and morphology of the tungsten carbide cobalt – chromium powder.

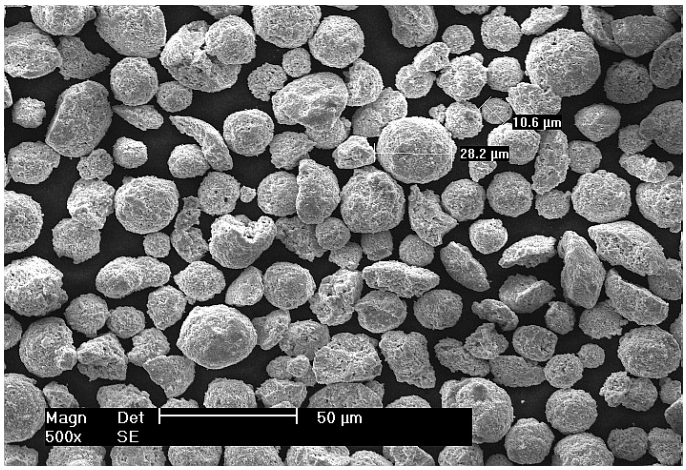

Figure 2.3 *SEM micrograph of the WC-CoCr 86 10 4 powder*

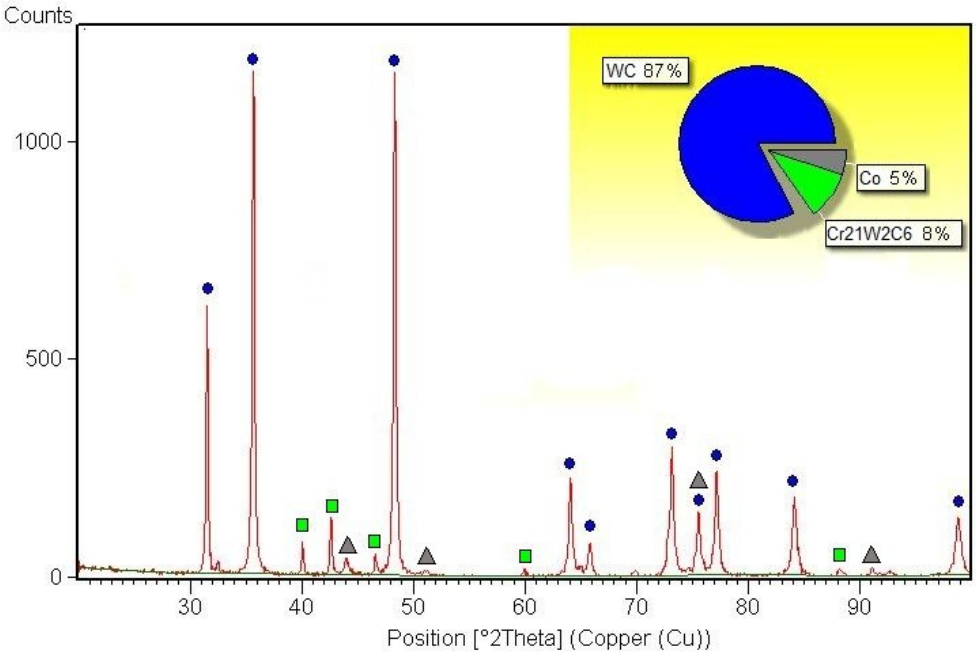

Figure 2.4 *XRD pattern of the WC-CoCr 84-10-6 powder*

The X-ray diffraction pattern shows that the powder consists of tungsten carbide (WC), chromium tungsten carbide (Cr21W2C6) and cobalt (Co).

2.2 Deposition techniques

The powder materials were deposited using two distinct thermal spray methods. The boron nitride in aluminium – silicon matrix powder was deposited with atmospheric plasma spraying (APS) and the tungsten carbide in cobalt – chromium matrix powder with the high velocity oxygen fuel (HVOF) technique. The features and principles of the two deposition methods are described below.

2.2.1 Atmospheric Plasma Spraying (APS)

Plasma spray is one of the most flexible of all the thermal spray processes as it can develop sufficient energy to melt any material. Since it uses powder as the coating feedstock, the number of coating materials that can be used in the plasma spray process is almost unlimited [64].

2.2.1.1 Principle of atmospheric plasma spraying

The atmospheric plasma spray principle in shown in figure 2.5

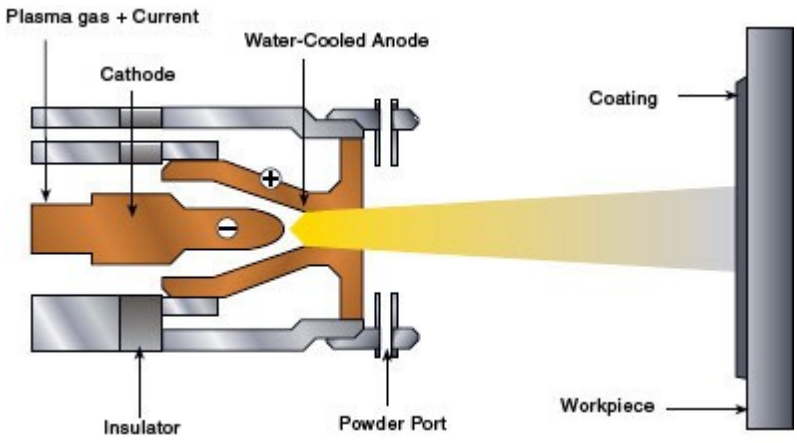

Figure 2.5 *Atmospheric plasma spray principle [www.surfacetechno.com]*

In this process the ionization of a plasma gas (H_2, N_2, Ar, He) takes place in an electric arc. The carrier gas, usually argon Ar, transports the powder to be sprayed in the plasma jet zone, where the partial or total melting of the particles takes place at temperatures between (4000 – 25000)°C.

The particles in this state will be projected on the surface of the material that follows to be coated. The cooling on the surface of the material takes place very rapidly (10^6-10^7 K/s), thus the molten particles transfer quickly in a solid state, while the heating of the substrate is very reduced.

2.2.1.2 Unique features of plasma spray process

The plasma spray process is characterized by a set of unique features:

- a wide range of materials and combinations of them can be deposited;
- possibility of deposition of mixed ceramics and alloys containing components with different vapour pressures without significant changes in coating composition;
- homogeneous coatings, without compositional changes across the thickness;
- microstructures with fine, equiaxed grain without columnar defects;
- high deposition rates of the order of mms^{-1} can be achieved with modest investment of capital;
- free-standing thick forms can be sprayed in near net shape fashion of pure and mixed ceramics;
- the process can be carried out in any environment such as air, reduced pressure, or underwater.

2.2.2 High Velocity Oxygen-Fuel (HVOF)

High Velocity Oxygen Fuel thermal spray system has been used in the aerospace industry for a variety of surface coating applications for many years. Due to the less porous structure of the HVOF sprayed coating as compared to the plasma sprayed one, the protection capability of the coating is increased [65]. However, because of the relatively low temperature of the HVOF flame, the spray process must be carefully optimized in order to produce coating with a sufficient melting state and good adhesion.

2.2.2.1 Principle of the high velocity oxygen fuel technique

The principle of high velocity oxygen fuel is illustrated in figure 2.6.

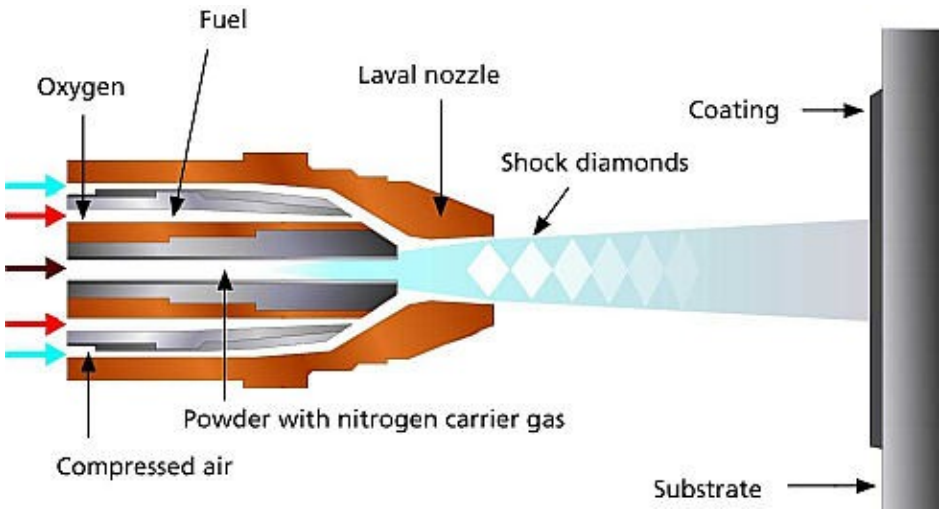

Figure 2.6 *High Velocity Oxygen Fuel principle [www.surfacetechno.com]*

The HVOF process uses a mixture of gaseous or liquid fuel, which are fed into a combustion chamber and combusted continuously. A powder feed stock is then injected in the gas stream. The powder are partially melted in the stream and propelled at near supersonic speeds onto the substrate.

2.2.2.2 Characteristics of the HVOF spray method

The performance advantages of HVOF tungsten carbide coatings have been demonstrated for a variety of aviation engine and airframe components including aircraft flap tracks, landing gear, actuators, jet engine bearings, and even some dynamic components, such as helicopter drive trains and propeller assemblies.

Some of the advantages given by this deposition method are:

- high density coatings;
- good bonding to the substrate;
- reduced oxidation risk, due to the very high velocities;
- reduced heating of the substrate;
- possibility to deposit different mixtures of materials.

2.3 Methods of investigation

The features of the as-sprayed and electron beam remelted coatings were characterized by means of X-ray diffraction, energy dispersive spectrometry (EDX) and scanning electron microscopy. The wear rates of the treated samples were determined with the pin-on-disc method. The corrosion behavior was investigated through electro-corrosion testing and the hole-drilling method was used for determining the residual stresses of the electron beam irradiated samples.

2.3.1 X – Ray diffraction

X-ray diffraction was performed on the X´Pert MPD from Phillips (fig 2.7).

Figure 2.7 *X´pert MPD diffractometer*

X-ray diffractometry can identify specific compounds on the basis of their crystal structure. In XRD, an aggregate of small crystal fragments is irradiated with a monochromatic beam of X-rays. The beam is diffracted at angles determined by the planes of the atoms in the crystals. The intensity and spacing of these diffracted beams are unique to each type of crystalline material and can be identified by comparison to an established data base.

2.3.1.1 The nature of X - rays

X-Rays are relatively short wavelength, high-energy electromagnetic radiations. These are characterized by either their energy E, wavelength λ (i.e., distance between peaks) or frequency ν (the number of peaks which pass a point per second) [66]. The following are useful relationships for inter-converting the most common measures of radiation energy:

$$\lambda = \frac{c}{\nu} \qquad \text{(Eq. 2.1)}$$

$$E = h \cdot \nu \qquad \text{(Eq. 2.2)}$$

where, c – speed of light

h – Planck´s constant

Wave numbers particularly in the low energy regions of the electromagnetic spectrum are used, such as the microwave and the infrared. A wave number ($\bar{\nu}$) is frequency divided by the speed of light

$$\bar{\nu} = \frac{\nu}{c} = \frac{c/\lambda}{c} = \frac{1}{\lambda} \qquad \text{(Eq. 2.3)}$$

The angstrom unit (Å) defined as 1x10^{-10}m, is the most common unit of measure for X-rays. Energy in electron volts is related to angstroms through:

$$E(eV) = \frac{h \cdot c}{\lambda_{cm}} = \frac{12396}{\lambda_A} \qquad \text{(Eq. 2.4)}$$

2.3.1.2 The detection of X - rays

The nature of X-ray detectors and the electronics used with them is an important part of understanding the approaches to, and limitations of, X-ray application. The modern X-ray diffractometer has developed primarily with the use of scintillation detectors, while fluorescence spectrometers more commonly use proportional counters [67]. Most recently position sensitive proportional counters and high-energy resolution solid state detectors have gained popularity.

The principal methods used to detect X-rays are:

- Non-Electronic Detector;
- Gas- Ionization Detector;
- Solid State Detector;
- Electronic Processing of X-ray signals.

2.3.1.3 Bravais Lattices

The atoms in a crystal structure are arranged in groups which repeat three-dimensionally to make up a crystal structure. If each symmetrically unique group of atoms would be considered a single point, then the entire crystal structure can be imagined as a three-dimensional lattice of these points. This concept is called a space lattice and the points which define it are lattice points. These lattice points represent the asymmetric unit or basis of the crystal structure, which is the smallest group of atoms upon which the crystallographic symmetry operates to produce the complete crystal structure [66].

These periodic arrays can be sorted into seven unique arrangements called crystal systems and define the coordinate systems described in table 2.1. By connecting the translation vectors that exist between the lattice points along the three principal axes of the coordinate system, a collection of boxes called unit cell are produced. The three vectors which define the unit cell have lengths of a, b and c making angles of α, β and γ with each other.

Table 2.2 *Crystal systems and Bravais lattices [66]*

Crystal class	*Axis system*	*Bravais lattice*
Cubic	$a=b=c\,,\alpha=\beta=\gamma=90\,°$	**P, I, F**
Tetragonal	$a=b\neq c\,,\alpha=\beta=\gamma=90\,°$	**P, I**
Hexagonal	$a=b\neq c\,,\alpha=\beta=90\,°\,,\gamma=120\,°$	**P**
Rhomboedral	$a=b=c\,,\alpha=\beta=\gamma\neq 90\,°$	**R**
Orthorhombic	$a\neq b\neq c\,,\alpha=\beta=\gamma=90\,°$	**P, C, I, F**
Monoclinic	$a\neq b\neq c\,,\alpha=\gamma=90\,°\,,\beta\neq 90\,°$	**P, C**
Triclinic	$a\neq b\neq c\,,\alpha\neq\beta\neq\gamma\neq 90\,°$	**P**

When the unit cell, which repeats itself in space is defined by one point at each corner, the unit cell is called primitive and given the symbol **P**. If there is an additional lattice point in the middle of each cell it is called body centered and given the symbol **I**. When the cell has points in each corner and in the center of each face, is called face centered and the symbol **F** is used. The rather strange rhomboidal cell, in which the three interaxial angles are equal and acute, is given the symbol **R**. The last type of Bravais lattice is when only one face is centered. The symbol used to describe this cell type depends on the name of the centered face. The plane perpendicular to the ***a*** and ***b*** directions of the lattice is called **C**. Likewise, the face perpendicular to the a and c directions is called **B** [66,67].

2.3.1.4 Miller Indices

The unit cell is a very useful concept and its use is not only to characterize the symmetry of a crystal, but also to specify crystallographic directions and even inter-atomic distances. To describe directions and distances planes with various orientations, intercepting the translation vectors at various points are considered. For example, the plane which passes through each unit cell intercepting the ***a*** axis at ½ and parallel to the ***b*** and ***c*** axes has a Miller indices of $1/2,1/\infty,1/\infty$ or (200) [68].

The distance (d_{hkl}) between the planes is on the same order as the distances between atoms. It should be noted that these d-values are vectors, having direction and magnitude. It should also be noted that Miller indices defining a plane are usually written in brackets, as (hkl), while crystallographic directions, which are the normal to any plane, are written in square brackets as $[hkl]$.

2.3.1.5 Diffraction and Bragg´s Law

Diffraction occurs when waves scattering from an object constructively and destructively interfere with each other. Waves are characterized by their wavelength (λ), which is defined as the distance between peaks. If wave scatters from an object it will do so in all directions. If a second wave scatters from another object, displaced from the first by a distance on the order of the wavelength, then there will be some angle at which we can view the two scattered waves such that they will be in phase [68].

W. L. Bragg was the first to show that the scattering process that leads to diffraction can be equally visualized as if the X-rays were 'reflecting' from the imaginary planes defined by Miller indices **(hkl)**. This view pushes the reflection analogy rather hard; however, this rather strained analogy allows a simple derivation of the overall controlling law, which describes the phenomena of diffraction.

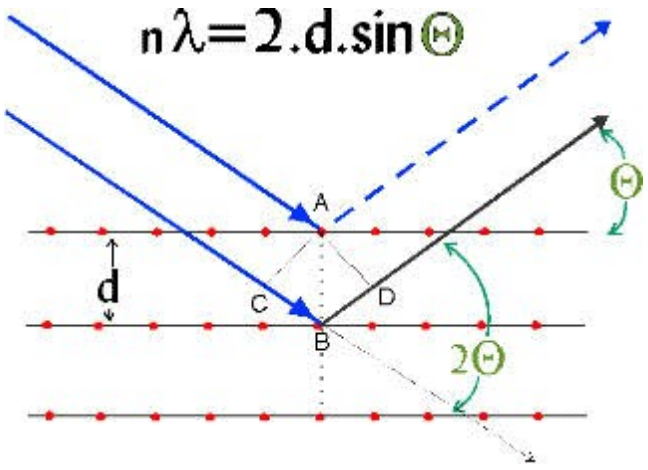

Figure 2.8 *Bragg´s law [http://serc.carleton.edu]*

In figure 2.8, X-rays impinge on a set of atomic planes, with indices **(hkl)**, from the left, marking an angle Θ with them. The distance between the planes is $\mathbf{d_{hkl}}$ ($\mathbf{d_{hkl}}$ is inter-atomic distance). However, all of the atoms in a unit cell will be bathed in the X-ray beam and, in fact, all will be scattering in all directions.

$$n\lambda = 2d\sin(\Theta) \qquad \text{(Eq. 2.5)}$$

$$\lambda = 2d_{hkl}\sin(\Theta) \qquad \text{(Eq. 2.6)}$$

where **n** is an integer

This equation (called Bragg' s law) allows us to relate the distance between a set of planes in a crystal and the angle at which these planes will diffract X-rays of a particular wavelength.

2.3.2 Scanning electron microscopy (SEM)

SEM micrographs and EDX of the investigated samples were performed on the XL 30 ESEM scanning electron microscope from Phillips.

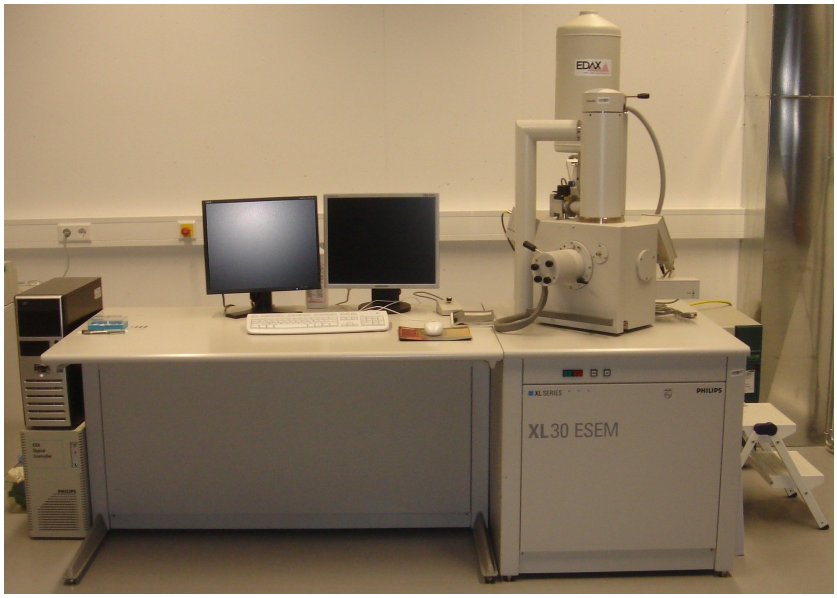

Figure 2.9 *XL 30 ESEM scanning electron microscope*

The Scanning Electron Microscope (SEM) is a microscope that uses electrons rather than light to form an image. There are many advantages to using the SEM instead of a light microscope. The SEM has a large depth of field, which allows a large amount of the sample to be in focus at one time. It also produces images of high resolution, which means that closely spaced features can be examined at a high magnification. Preparation of the samples is relatively easy since most SEMs only require the sample to be conductive. The combination of higher magnification, larger depth of focus, greater resolution, and ease of sample observation makes the SEM one of the most heavily used instruments in research areas today [69].

2.3.2.1 SEM principle

A beam of electrons is produced at the top of the microscope by heating of a metallic filament. The electron beam follows a vertical path through the column of microscope. It makes its way through electromagnetic lenses, which focus and direct the beam down towards the sample. Once it hits the sample, electrons (back-scattered or secondary) are ejected from the sample. Detectors collect the secondary or back-scattered electrons, and convert them to a signal that is sent to a viewing screen, producing an image [70]. This is shown schematically in Figure 2.10.

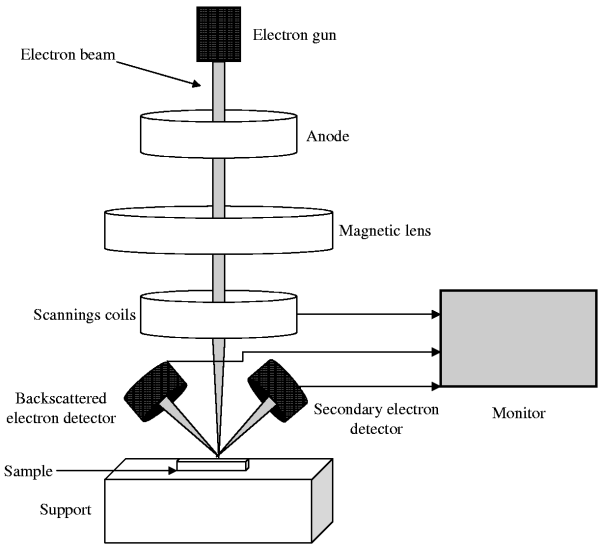

Figure 2.10 *Principle of scanning electron microscopy*

The type of signals produced by a SEM at the interaction of the electron beam with the sample surface include secondary electrons (SE), back-scattered electrons (BSE), characteristic X-rays (EDX) and photons of various energies, but for microscopy only the secondary and back-scattered electrons are of great interest, since they vary according to difference of topography of the specimen.

2.3.2.2 Secondary electrons

Secondary electrons are the electrons ejected from the k-orbitals of the specimen atom and usually have an energy lower as 50 eV. Because of their low energy, secondary electrons originate within only a few nanometers from the samples surface (5 nm). The secondary electrons are first collected at about 400 V and then accelerated towards an scintillator at 2000 V. The accelerated secondary electrons are now sufficiently energetic to cause the scintillator to emit light flashes, which are conducted to a photomultiplier. The amplified electrical signal output by the photomultiplier is displayed as a two-dimensional intensity distribution that can be viewed and photographed on an analogue video display, or subjected to analog-to-digital conversion and displayed and saved as a digital image [71].

2.3.2.3 Back-scattered electrons

The electrons escaping from the surface of the sample and having an energy of ≥ 50 eV are referred to as back scattered electrons (BSE). They are reflected or back-scattered out of the specimen interaction volume by elastic scattering interactions with specimen atoms. Since heavy elements (high atomic number) back-scatter electrons more strongly than light elements (low atomic number), and thus appear brighter in the image, BSE are used to detect contrast between areas with different chemical compositions [71].

2.3.2.4 Energy dispersive X-ray spectroscopy

Energy dispersive X-ray spectroscopy is an analytical technique used for the elemental analysis or chemical characterization of a sample. Its characterization capabilities are due to the fundamental principle that each element has a unique atomic structure allowing X-rays, which are characteristic of element's atomic structure, to be identified uniquely from one another [72].

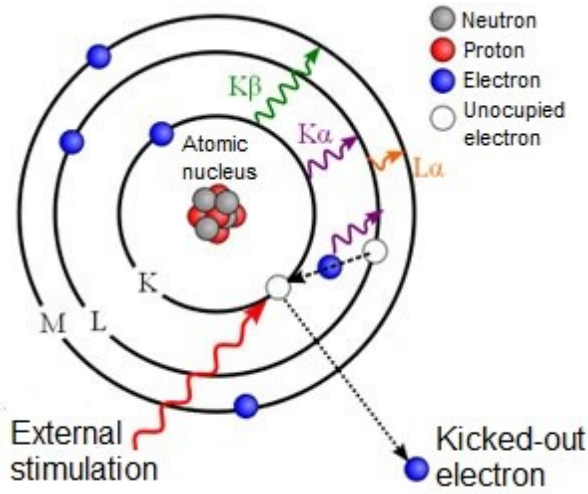

Figure 2.11 *EDX principle [www.quality-analysis.de]*

To stimulate the emission of characteristic X-rays from a specimen, a high energy beam of charged particles such as electrons or protons is focused into the sample being studied. At rest, an atom within a sample contains unexcited electrons in discrete energy levels or electron shells bound to the nucleus. The incident beam may excite an electron in the inner shell, ejecting it from its shell, thus creating an electron hole. An electron from an outer higher energy shell then fills the hole and the energy difference between the shells is released in the form of an X-ray. Because the energy of the X-rays are characteristics of the energy difference between two shells and of the atomic structure of the element from which they were emitted, the measurement of the samples elemental composition is possible [73].

2.3.3 Pin-on-disc method

The sliding wear rate and coefficient of friction of the investigated samples were determined using a CSM pin-on-disc tribometer.

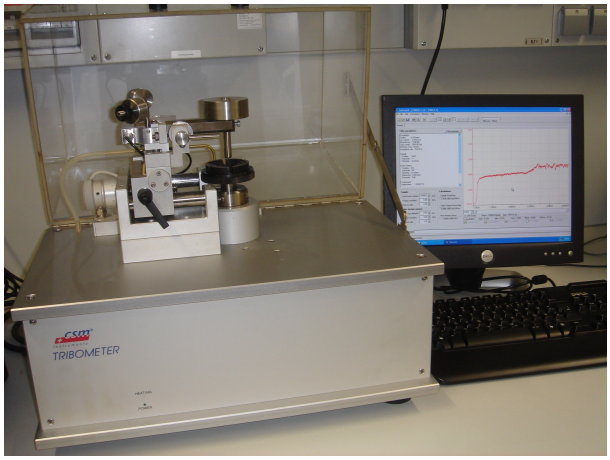

Figure 2.12 *CSM pin-on-disc tribometer*

The unit consists of an arm to which the pin (usually a cermet ball) is attached, a sample holder which allows the mounting of square or disc shaped samples, an electronic force sensor for measuring the friction force, and a computer software for displaying the parameters and storing data for analysis.

The tribometer permits testing with loads up to 10 N, radial speeds ranging between (0,3 – 500) rpm an an adjustable radius of maximum 30mm.

2.3.3.1 Friction coefficient and wear rate determination

The signal for the coefficient of friction is displayed in real time during the test on a PC screen, by measuring the deflection of the elastic arm (fig. 2.13)

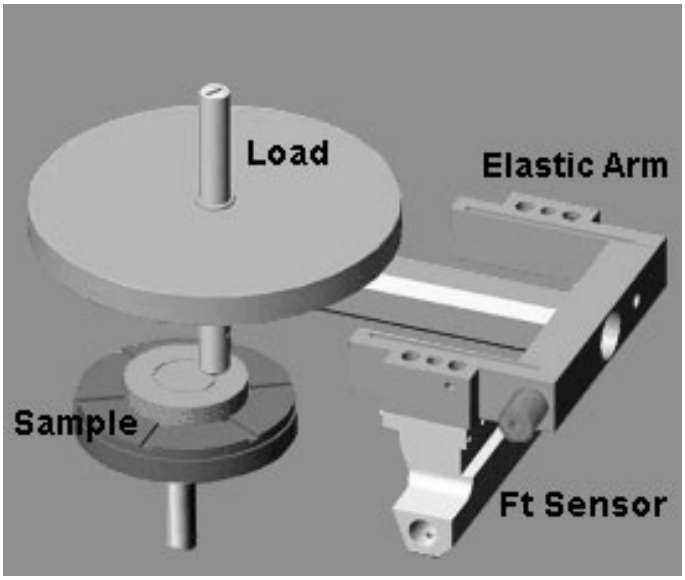

Figure 2.13 *Coefficient of friction measurement [http://www.csm-instruments.com]*

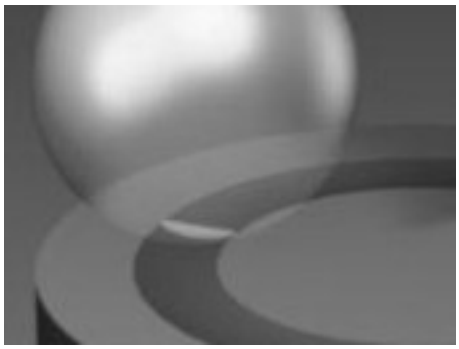

Figure 2.14 *Wear groove geometry [http://www.werner-stehr-tribologie.com]*

The wear rate is quantified by measuring the wear groove and determining the amount of removed material of both sample and ball [74]. The wear rate K is calculated with the equation presented in chapter 1.2.2.3 by adapting it to the shape of the wear groove.

$$K = \frac{V}{L \cdot d} \qquad \text{(Eq. 2.7)}$$

$$V = 2\pi r \cdot A \qquad \text{(Eq. 2.8)}$$

$$A = \frac{h}{6 \cdot s}\left(3h^2 + 4s^2\right) \qquad \text{(Eq. 2.9)}$$

(2), (3) → (1) => $K = \frac{2\pi r \cdot h\left(3h^2 + 4s^2\right)}{6 \cdot L \cdot d \cdot s}$ (Eq. 2.10)

The values for the wear rate are computed by the computer software by introducing the testing parameters: normal load (L) and testing distance (d) and the dimensions of the resulted wear groove height (h) and length (s), as well as the worn cap diameters of the testing pin ball.

2.3.4 Hole drilling residual stress measurement

Residual stress measurements were conducted with the aid of RESTAN equipment from SINT (fig.2.15) through the hole drilling method, which is a strain release based technique.

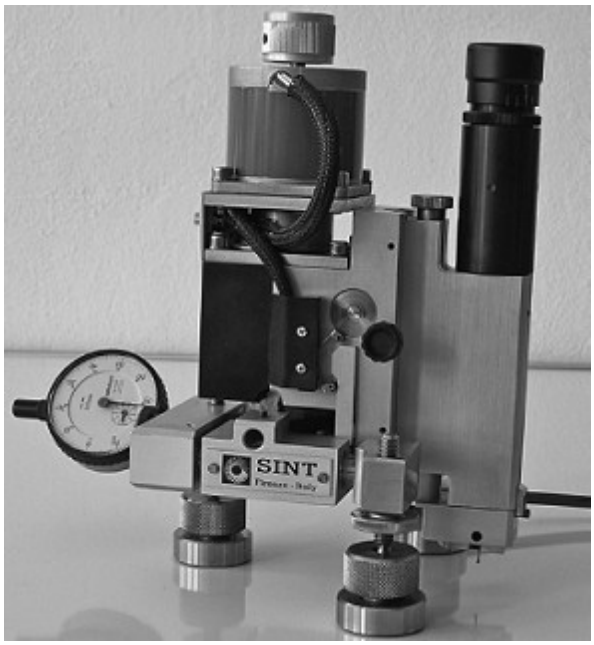

Figure 2.15 *RESTAN residual stress measurement device*

The equipment consists of three magnetic legs connected to the main body by adjustable rods. The heart of the system is represented by a microscope and a high-speed turbine fixed on the main body. During the drilling the turbine is exactly in the axial position with microscope. After optical centering and inspection the turbine can rotate around its axes so the hole is visible by microscope. The turbine is connected to an air system and can reach approximately 300.000 rpm.

2.3.4.1 Principle of the hole drilling method

This semi-destructive technique allows stress determination in the near surface of a sample by measuring the strains induced by hole drilling using strain gage rosettes.

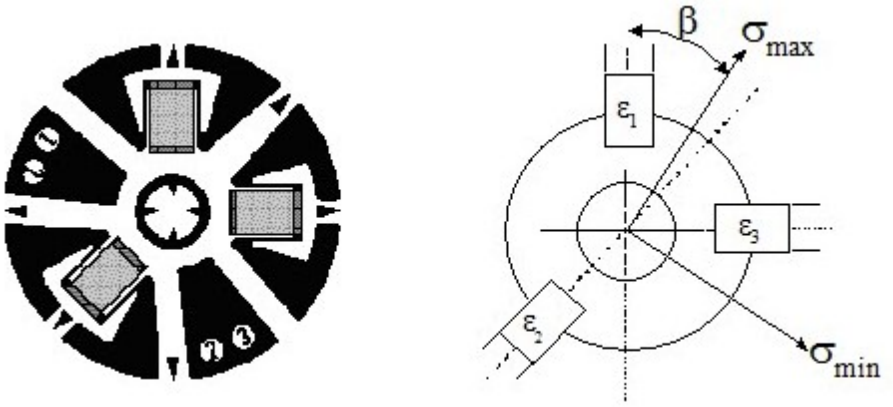

Figure 2.16 *ASTM standard strain gage rosette [http://sites.google.com/site/temfemguy]*

The strain gage rosette is glued to the smoothed surface of the sample and a 1,8 mm diameter hole is incrementally drilled in the strain gage rosettes bulls-eye. Drilling can be conducted step-by-step or in an automatic sequence. The resultant strains corresponding to the stresses released by drilling are recorded by the three gages for each performed step. The stress field is then calculated using established equations [75].

2.3.4.2 Data processing

As mentioned above, the principal stresses are obtained by converting the effective strains recorded during the hole drilling, using the following equations:

$$\sigma_{max} = \frac{\varepsilon_3 - \varepsilon_1}{4A} + \frac{\sqrt{(\varepsilon_3 - \varepsilon_1)^2 + (\varepsilon_3 + \varepsilon_1 - 2\varepsilon_2)^2}}{4B} \qquad \text{(Eq. 2.11)}$$

$$\sigma_{min} = \frac{\varepsilon_3 - \varepsilon_1}{4A} - \frac{\sqrt{(\varepsilon_3 - \varepsilon_1)^2 + (\varepsilon_3 + \varepsilon_1 - 2\varepsilon_2)^2}}{4B} \qquad \text{(Eq. 2.12)}$$

$$\beta = \frac{1}{2}\arctan\left(\frac{(\varepsilon_3 + \varepsilon_1 - 2\varepsilon_2)}{\varepsilon_3 - \varepsilon_1}\right) \qquad \text{(Eq. 2.13)}$$

where, σ_{max} – maximum principal stress, [MPa]

σ_{min} – minimum principal stress, [MPa]

β – angle between the maximum principal stress σ_{max} and gauge 1

A, B – material dependent constants

$\varepsilon_1, \varepsilon_2, \varepsilon_3$ – strains measured by the three strain gages

Once the principal stresses and the angle between them and the strain gauges axes have been obtained, stresses in any other direction can easily be determined.

Four methods of stress determination are usually used: Standard ASTM E 837-01, Integral method, Power Series and the Kockelmann method, but the mostly mentioned in technical literature is the *Integral method* because it is applied for determination of residual stresses in the depth of the hole, especially in locations where the stress along hole depth varies due to different specimen thickness. This method makes possible to use constant amplitude, amplitude which growths with the depth of the hole, or variable stress distribution with optimization of amplitude in depth and oriented to reduction of measurement errors.

2.3.5 Electrochemical corrosion test

The corrosion behavior of the alloyed samples was determined through electrochemical corrosion test, using an electrolytic cell under large signal-polarization. This system is also known under the name of “Three electrode device”.

Figure 2.17 *Electrochemical corrosion cell*

When a current is imposed on an electrolytic cell, reactions at both electrodes are not at equilibrium, and there is consequently an over-potential on each of them. The potential difference measured between the two electrodes then includes the value of the two over-potentials, and it is not possible to determine the potential of the test electrode (sample). To obtain this value, a third electrode, the auxiliary or counter-electrode, must be used. In this arrangement, current flows only between the test and the auxiliary electrodes. A high-impedance voltmeter placed between the test and the reference electrodes prevents any significant current flow through the reference electrode, thus maintaining a stable potential. The test electrode potential and its changes under electric current flow can then be measured with respect to a fixed reference potential [76].

2.3.5.1 Large signal polarization

In large-signal polarization tests, the applied potential is varied over a wide range, using either a series of applied potential steps or a change of potential at a constant rate. There are two types of potentiostatic techniques:

- *Type 1:* recording of the current as a function of time at a constant applied potential, E_{appl}
- *Type 2:* recording of the steady-state current as a function of E_{appl} this type being mostly used because it allows the plotting of a polarization curve

The test is started by applying the first potential. After the current, which is recorded continuously throughout the test on a strip-chart recorder, has reached a steady-state value or after a predetermined time has elapsed, E_{appl} is increased to the next value, and the current is recorded. After the current at the final value of E_{appl} has been recorded, the polarization curve (E_{appl} versus log i) can be plotted using the final values of the current, I, at each potential and converting it into current density, i [77].

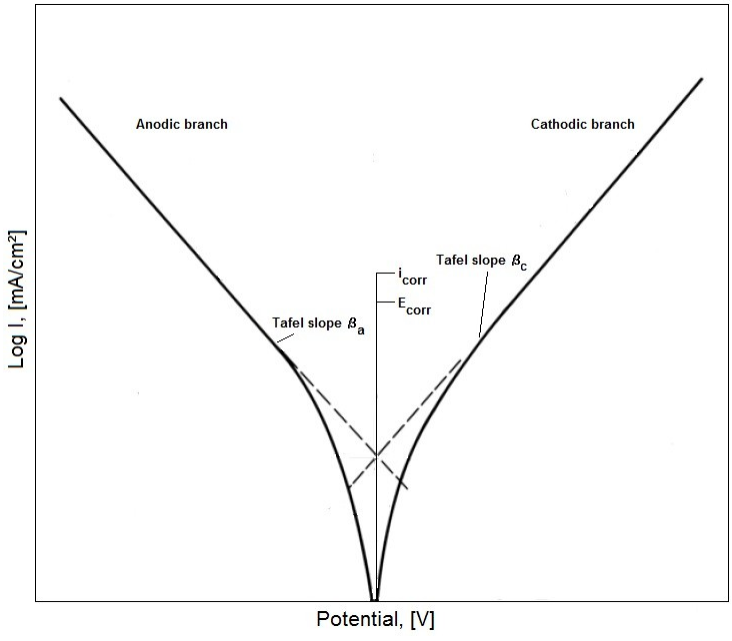

Figure 2.18 *Tafel extrapolation [77]*

A complete polarization curve consists of a cathodic part and an anodic part. The cathodic portion of the polarization curve contains information concerning the kinetics of the reduction reactions occurring for a particular system. Usually, a charge-transfer-controlled region occurs at potentials close to the corrosion potential $E_{corr.}$

The relationship between the applied potential, E_{appl}, and the measured current density, i, in the Tafel region is given by

$$E_{appl} = E_{corr} + \beta_a \log(i / i_{corr}) \qquad \text{(Eq. 2.14)}$$

$$E_{appl} = E_{corr} + \beta_c \log(i / i_{corr}) \qquad \text{(Eq. 2.15)}$$

where, β_a - anodic Beta Tafel constant

β_c - cathodic Beta Tafel constant

Plots of E_{appl} versus log i are called Tafel plots. The corrosion current density, i_{corr}, can be determined according to Eq 1 and 2 by extrapolation of the Tafel lines to $E_{appl} = E_{corr}$, where $i = i_{corr}$ (fig. 2.18). This method of obtaining corrosion current density is called the Tafel extrapolation method. It is also possible to determine i_{corr} from the intersection of both plots and it is advantageous to use computer software to record polarization curves and analyze the experimental data in terms of parameters such as β_a, β_c, and i_{corr} [78].

Chapter III

Powder deposition

3.1 Sample preparation

Prior to the coating process, the surfaces were subjected to a shot peening operation. In this process, abrasive particles (usually aluminium oxide) are propelled by high velocity compressed air onto the workpiece mainly to induce compressive stresses, in order to increase fatigue life; but also to remove surface contaminants, such as oxides and to roughen the surface, thus improving coating adhesion. In this second case, shot peening resembles sandblasting, except that it operates by the mechanism of plasticity rather than abrasion.

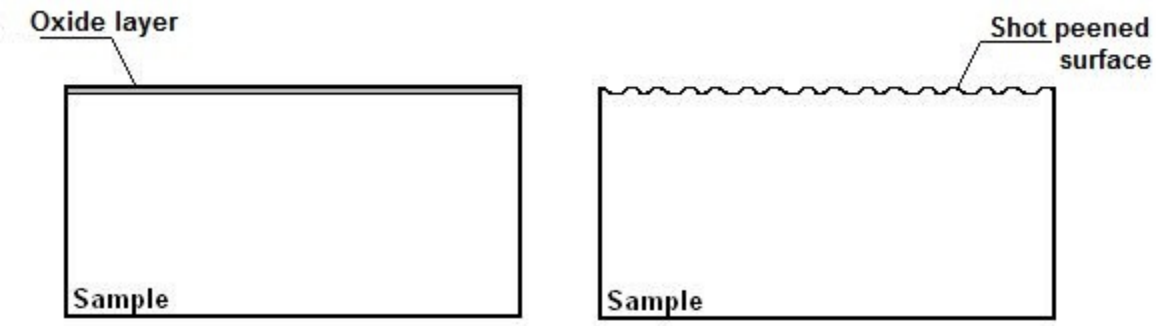

Figure 3.1 *Shot peening effect on the surface geometry*

3.2 Process parameters

3.2.1 A.P.S parameters used in the deposition of the Al8Si20BN

The parameters of the atmospheric plasma spraying process used for the deposition of the boron nitride aluminium-silicon powder are presented in table 3.1.

thermico **Plasma**

Table 3.1 *APS parameters used for the deposition of the boron nitride aluminium-silicon powder*

Burner									
Burner type	Axial III			Powder injection type	Axial				
Burn-chamber type	-			Powder injection angle	-				
Gases									
Hydrogen pressure [bar]	7,5	Argon pressure [bar]	7,5	Nitrogen pressure [bar]	7,5				
Powder doser									
Manufacturer	Thermico								
Type	CPF-2			Transport gas pressure [bar]	7				
Deposition installation									
Manufacturer	Mettech			Type	Axial III				
Burner									
Nozzle	6mm Thermico								
Application									
Sample drawing	***Plate***								
Base material	Titanium								
Powder									
Manufacturer	Sulzer Metco								
Material	Al8Si20BN								
Particle size [µm]	-45 +215								
Burner control system									
Total Flow [l/min]	280								
Argon [l/min]	***238***								
Hydrogen [l/min]	14								
Nitrogen [l/min]	28								
Current[A]	120								
Power [KW]	52								
Powder doser									
Transport gas [l/min]	23								
Discharge[g/min]	40								
Vibrator pressure [bar]	2								
Processing									
Spraying distance [mm]	170								
Spraying angle [Grad]	90								
Robot programme	Flow5_1								
Robot speed [m/sec]	0,01								
Number of overlaps	10								
Coating thickness [µm] set / is	150	150							

A mixture of hydrogen, argon and nitrogen was used as plasma gas with total gas flow of 280 l/min. The powder transport was realized with 28 l/min nitrogen gas flow. The coating process was conducted in 10 overlaps at a deposition distance of 170 mm.

3.2.2 HVOF parameters used in the deposition of the WC-CoCr 84-10-4

The parameters used for the deposition of the tungsten carbide powder are presented in table 3.2

HVOF

Table 3.2 *HVOF parameters used for the deposition of the tungsten carbide cobalt – chromium powder*

Burner									
Burner type	CJS			Powder injection type		4.2			
Burn-chamber type	5.2			Powder injection angle		16			
Gases									
Hydrogen pressure [bar]	20	Oxygen pressure [bar]	20	Nitrogen pressure [bar]	10				
Powder doser									
Manufacturer	Thermico								
Type	CPF-2			Transport gas pressure [bar]	7				
Deposition installation									
Manufacturer	Thermico			Type	C – CJS				
Burner									
Nozzle									
Application									
Sample drawing	***Plate***								
Base material	Titanium								
Powder									
Manufacturer	Thermico								
Material	WC-CoCr 86 10 4								
Particle size [µm]	-25 +5								
Burner control system									
Oxygen [l/min]	700								
Hydrogen [l/min]	110								
Kerosene [l/h]	21								
Nitrogen [l/min]	20								
Powder doser									
Transport gas [l/min]	2 x 12,8								
Discharge[g/min]	2 x 40								
Vibrator pressure [bar]	2								
Processing									
Spraying distance [mm]	350								
Spraying angle [Grad]	90								
Robot programme	Axi 45								
Robot speed [m/sec]	0,9								
Number of overlaps	13								
Coating thickness [µm] set / is	150	200							

A 21l/h kerosene gas flow and a 20 l/min N_2 transport gas flow were used for the deposition. The coating was realized in thirteen overlaps at a spraying distance of 350 mm.

3.3 Investigation of the as-sprayed coatings

The SEM images of the deposited boron nitride aluminium-silicon coating (fig. 3.2) show coagulated particles of boron nitride (red arrow). Also, the phase agglomeration and density differences led to the formation of cracks in the coating (green arrows).

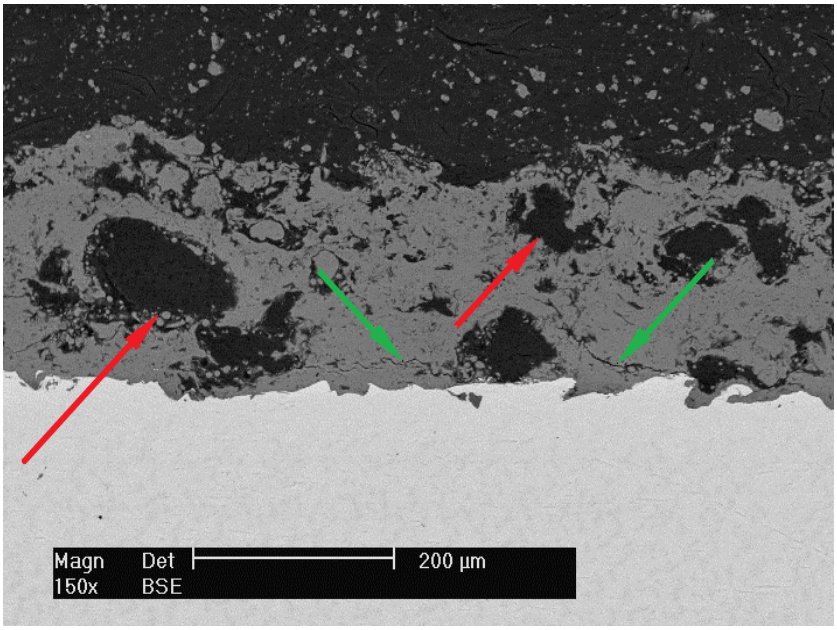

Figure 3.2 *SEM micrograph of the Al8Si20BN coating*

Investigations of the as-sprayed tungsten carbide cobalt-chromium coating revealed that the coating contains oxide inclusions and a high degree of porosity, especially along the coating/substrate interface, which could contribute to a poor bonding during mechanical loading (fig. 3.3).

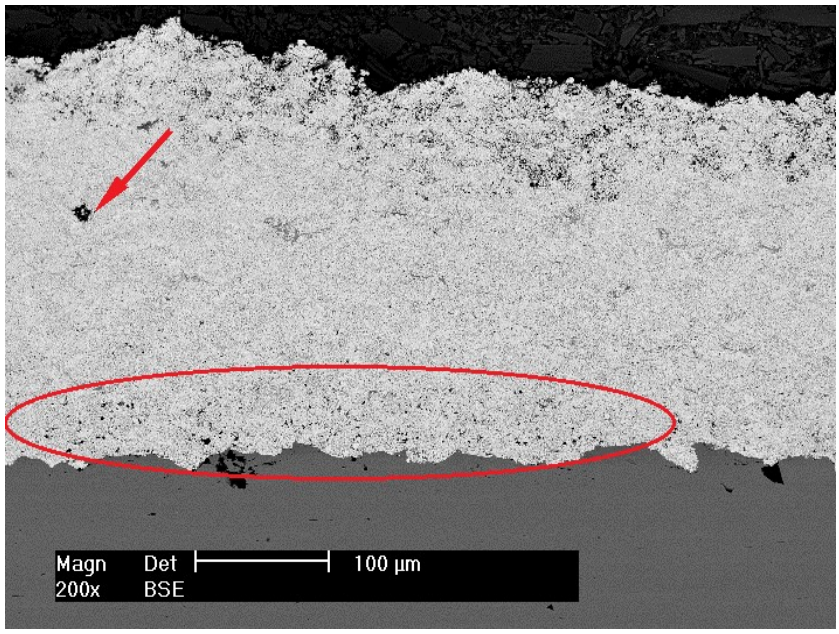

Figure 3.3 *SEM micrograph of the WC-CoCr 84-10-6 coating*

3.4 Conclusions

In this chapter the powder deposition process, including sample preparation, the deposition parameters of both used spraying techniques and the quality of the as-sprayed coatings were presented. From the SEM micrographs of the deposited coating it can be concluded that the shot peening operation performed prior to the spraying process leads to a good mechanical anchoring of the coating on the base material. However, the APS deposited coating shows agglomerations of the hard boron nitride particles and crack formation. In the case of the tungsten carbide cobalt-chromium coating, some oxide inclusions and a high degree of porosity can be seen. These circumstances may lead to unsatisfactory behavior and failure of the coatings under operating conditions.

Chapter IV

Electron beam remelting of the pre-deposited coatings

4.1 Electron beam surface engineering

Despite an intensive development in various hardening methods (including LASER ones) sometimes desired results can only be achieved through the use of electron beam (EB) technologies [79-82]. Nowadays, electron beam surface treatment is a common method for enhancing surface properties of iron, aluminium and titanium components [83-85].

There are basically two trends in the modification of surface properties of metallic components. The first one implies only microstructural modification achieved through transformation hardening, shocking or remelting, and the second consists in introducing compositional changes, which involves the complete (alloying) or a minimum/negligible (cladding) melting of a deposit [86]. The overall classification of the electron beam surface engineering processes is presented in figure 4.1.

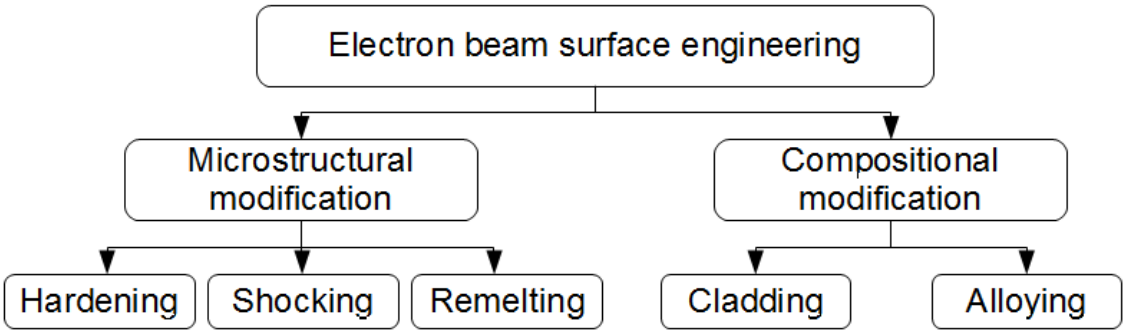

Figure 4.1 *Classification of electron beam surface engineering processes*

The electron beam technologies that include a liquid state of the base material and aim for compositional modification are very promising, since either soluble or insoluble alloying elements can be added in the molten bath.

4.1.1 Electron beam hardening (EBH)

EBH is a technique used to obtain hard and wear resistant surface layers with a typical thickness of 0.5 to 1.5 mm. The technique of EB transformation hardening can be seen as the opposite of conventional transformation hardening. In conventional hardening the product is heated by flame, induction or in a furnace. This process is a reversible equilibrium transformation which requires, dependent on the temperature and the composition some time, typical a few minutes. Hardening takes place when the material is subsequently cooled down at a so high cooling rate that there is not enough time available for the reverse transformation [87]. Together with this transformation a volume expansion occurs, which introduces advantageous residual stresses into the surface improving the mechanical properties like wear and fatigue resistance.

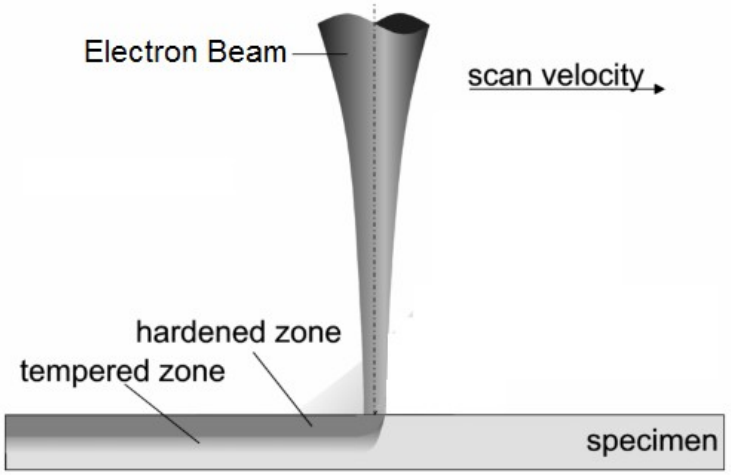

Figure 4.2 *Electron beam transformation hardening [101]*

Normal hardening takes place when the heated product is cooled down suddenly by water or oil. The outer layer cools first and fastest where at deeper layers the cooling rate is lower allowing a reverse transformation to the original structure. The final result depends strongly on the cooling rate and the geometry of the product [88]. In case of electron beam hardening the bulk of the product keeps cool. Only a surface layer is heated by the beam. Cooling takes place by the self-quenching effect of the bulk material.

Because heat transfer takes place by conduction this cooling rate is much higher than in water where vapor production restricts the cooling rate. The surface temperature for conventional hardening is low to reduce the distortion and to restrict the heat content in the bulk. For electron beam hardening on the other hand, the surface temperature should be as high as possible to ensure maximum hardness and hardening depth.

The upper temperature limit is given here by the requirement that surface melting has to be avoided.

4.1.2 Electron beam shock processing (EBS)

The electron beam shocking process represents a further development of classical material adaptation methods by introducing residual stresses by hydrodynamic expansion of heated plasma. The shock wave is a result of ablation of material layers via intensive absorption of electron beam irradiation [89,90]. The material surface originates a phase transformation from solid to material vapor. The plasma is developed in the gas phase which absorbs the energy directly from the laser radiation and from the reflection on the material surface. The expanding plasma causes a shock wave into the atmosphere and into the material (fig. 4.3).

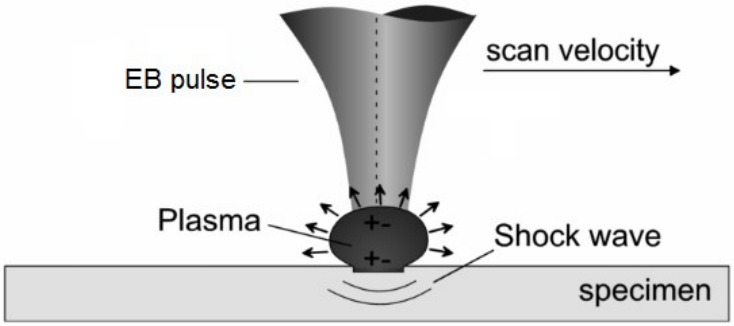

Figure 4.3 *Electron beam shock hardening [101]*

The pressure of the shockwave causes residual stresses in a depth of several millimeters, since local plastic forming causes stretching of a small area, which stands under pressure by the surrounding elastically formed material after release of the pressure.

4.1.3 Electron beam remelting (EBR)

The electron beam heats the base material up to the melting point and above but not up to the evaporation. Because of a relative movement of the electron beam and the base material, a track is generated that consists of the remelted zone and the heat affected zone (HAZ). The geometry of the remelted zone and the HAZ depends on the beam power and the geometry of the focal point on the surface of the work piece (beam intensity), the scanning speed and the absorption of the electron beam at the surface.

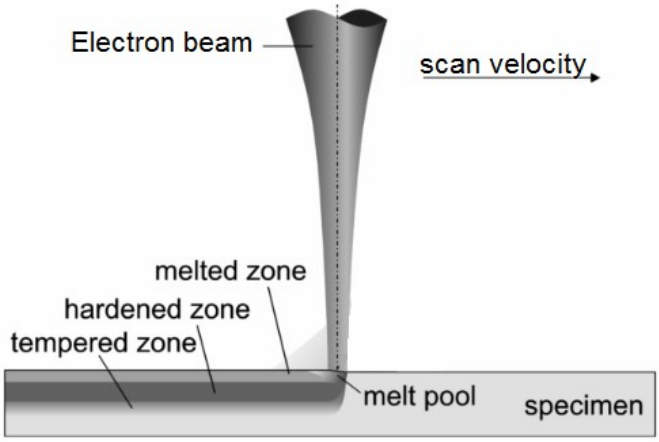

Figure 4.4 *Electron beam remelting [101]*

EBR can also be conducted on atmospheric plasma sprayed and flame sprayed coatings to remove voids, cracks and material inclusions [91]. Depending on the application the coatings may be remelted to certain depths (maximum to the coating/substrate interface), leading to an improved wear and corrosion behavior. Another positive aspect is that the EBR process is conducted in vacuum, thus avoiding the formation of oxide inclusions.

4.1.4 Electron beam cladding (EBC)

The aim of EBC is the deposition of a cladding onto surfaces of work pieces in order to generate functional layers or regenerate the natural shape of parts. The material is deposited by powder injection or by wire feeding. In combination with the electron beam generating a melt pool the additional material is melted. Usually, EBC is mostly done with powder injection [92]. The process is schematically shown in figure 4.5. The powder flow can be off-axis or co-axial. In both cases the powder travels some distance through the laser beam causing the particles to be preheated or even melted before they reach the melt pool.

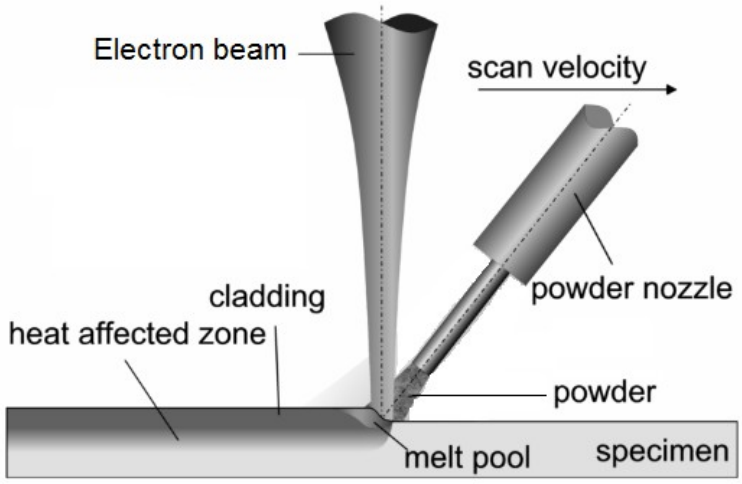

Figure 4.5 *Electron beam cladding [101]*

A characteristic of electron beam cladded surfaces is a comparably small dilution zone of substrate and clad material. In order to realize a low dilution zone the process parameters and material combinations have to be fitted to the geometrical boundary conditions of the work piece.

4.1.5. Electron beam alloying (EBA)

An electron beam surface remelting process that involves the addition of filler material with the principal aim of altering the chemical composition of the remelted metal is generally known as electron beam alloying [93-97]. As illustrated below, an electron beam is scanned across the surface of a work piece in order to melt a layer of material in a heat conduction mode. In the molten state, the metal is enriched with alloying elements.

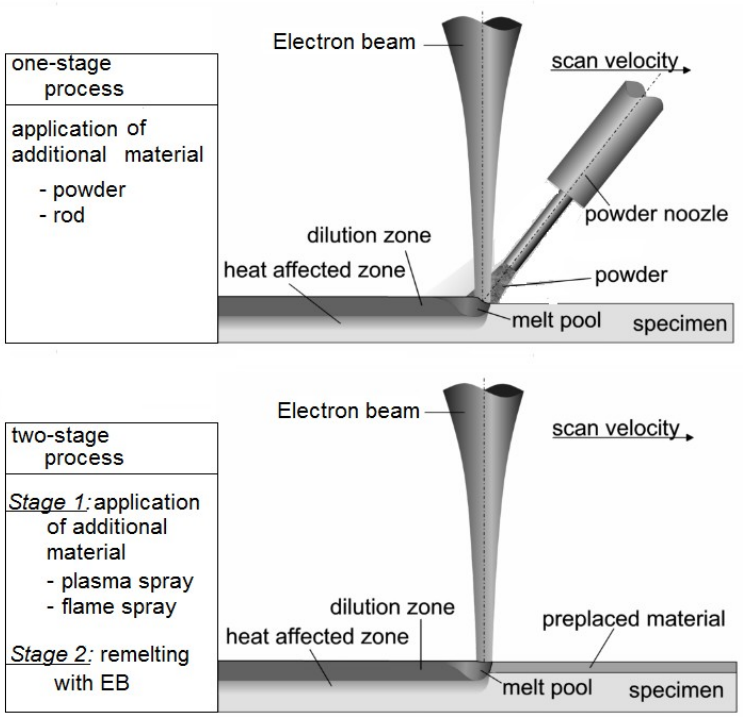

Figure 4.6 *One-stage and two-stage electron beam alloying [101]*

Two material application principles can be distinguished: the one stage (in-situ) technique and the two stage (pre-placed) technique, which are both displayed in figure 4.6. These two methods are both used in practice. The coating material is predominantly supplied in the form of powder particles.

The one stage process starts with the formation of a molten pool at the surface. Simultaneously, the addition material is fed into the the pool, melted and alloyed with the base material. Two possibilities of material feeding are available: wire feeding and powder injection, the second being preferred in most applications.

The two stage process consists in the pre-deposition and subsequent remelting of a coating [96]. When the coating is irradiated by the electron beam, the surface region rapidly reaches melting point and a liquid/solid interface starts to move through the coating. The liquid/solid interface advances and inter-diffusion between the coating and the substrate takes place. The re-solidification velocity rapidly increases towards the surface. The result of the re-solidification is the alloyed zone of the base material with the coating. The detailed alloying process is illustrated in figure 4.7.

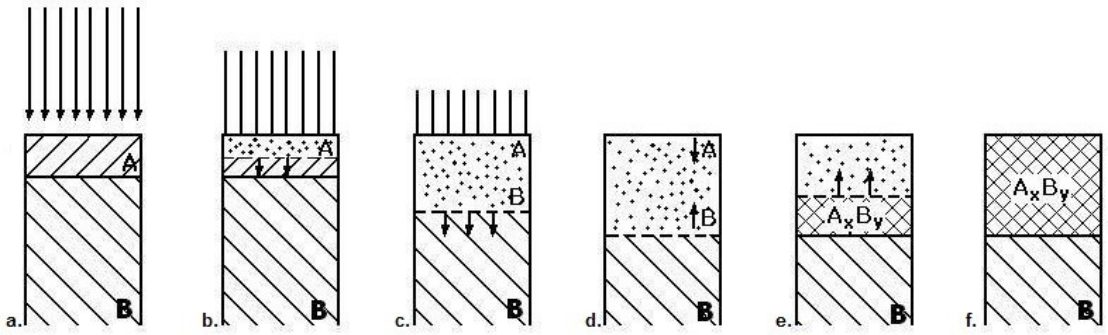

Figure 4.7 *Stages involved in EB alloying: (a) EB irradiation, (b) start of melting, (c) progress of liquid/solid interface, (d) inter-diffusion in liquid state, (e) start of solidification, (f) end of solidification*

4.1.6 Electron beam versus conventional methods

Thermal electron beam (EB) technologies are becoming more and more attractive especially because they are ecologically friendly and energy saving on the one hand and highly precise, excellently controllable and highly productive on the other hand [98].

Using three-dimensional energy transfer fields, the interaction conditions between the EB and the surface of the material, the conditions of the heat conduction in the material, the geometry of the part, and the load conditions of the component must be taken into account. High flexibility, precision, and reproducibility are typical characteristics of EB technologies and facilities [99,100]. High productivity is achieved by new technological solutions like simultaneous interaction of the EB in several processing areas (spots) or by carrying out several processes simultaneously in modern EB facilities and systems.

Table 4.1 *Characteristics of EB and EB technologies [100]*

Electron Beam (EB)	*EB Technologies*
excellent formability and deflect ability	high productivity
good beam profile	excellent flexibility
high efficiency	process safety
large penetration depth	high reproducibility
high beam stability	ecologically friendly

Because of the high velocities of material transport in the molten pool, pores and impurities reach the surface, where they are removed by the vacuum. The result are fine-grained, dense layers with a homogeneous distribution of the elements and negligible metallurgical defects.

4.2 Structural modifications in the substrate – coating system

The samples were remelted using an *EBW 700/3-6* electron beam installation, courtesy of the Universities endowment in Recklinghhausen.

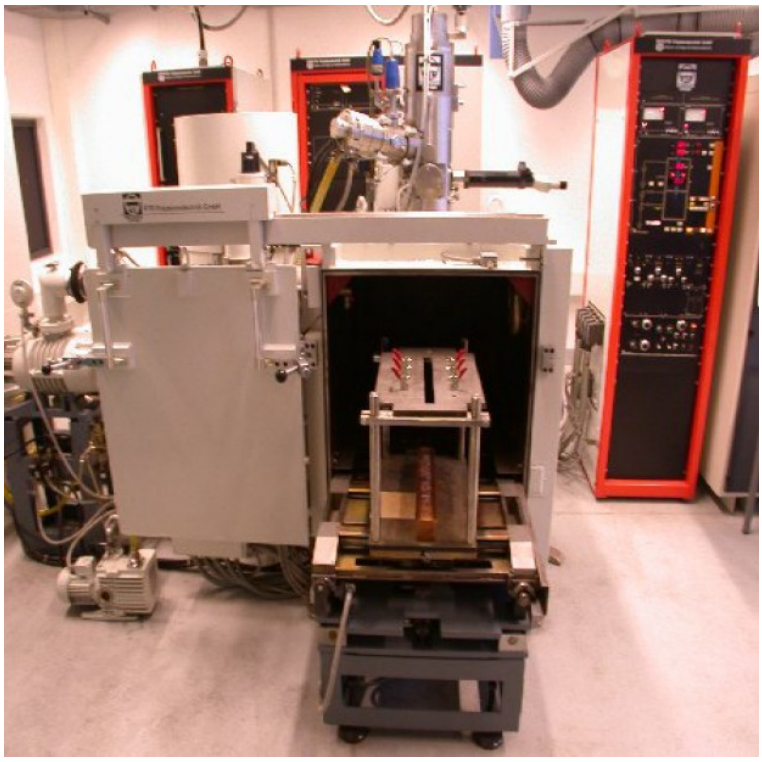

Figure 4.8 *EBW 700/3-6 electron beam equipment*

The electron gun is placed vertically and the electron beam is generated by electrical stimulation of a tungsten electrode. The vacuum chamber is equipped with a table which allows movement on the X, Y directions, as well as the rotation around the Z axis. Table 4.2 summarizes the working conditions of the electron beam equipment.

Table 4.2 *Electron beam remelting conditions*

Input power	Max. 3,3 kW	Oscillation (deflection)	
Voltage	50 – 60 kV	Amplitude	15 mm
Current intensity	10 – 55 mA	Frequency	1000 Hz
Process speed	2,5 – 25 mm/s	Wave shape	Triangle
Work distance	235 mm	Direction	X + Y

The process was conducted by modifying a parameter while maintaining the other parameters constant. The electron beam was scanned with a 1000 Hz frequency on a 15 mm surface, to obtain a remelted area as shown in figure 4.9.

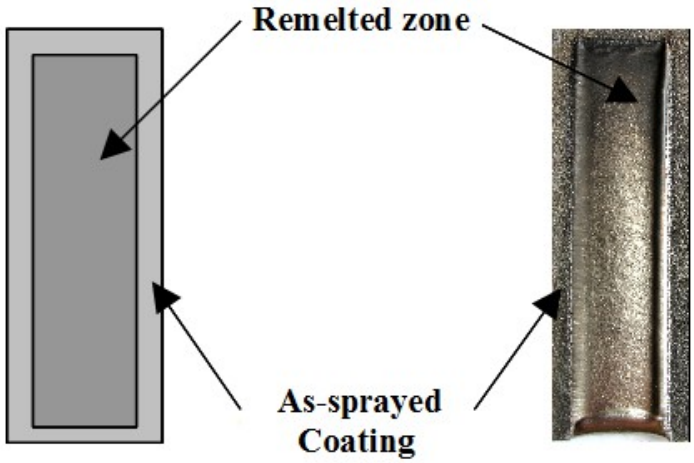

Figure 4.9 *Schematic of remelted samples*

4.2.1 Structural modifications in the titanium – boron nitride system

4.2.1.1 Remelting parameters

The electron beam remelting parameters of the boron nitride coatings are presented in table 4.3.

Table 4.3 *Remelting parameters of the Al8Si20BN coating*

U [kV]	I [mA]	v [mm/s]	Sample
60	10	2,5	TiBN1.1
	10	5	TiBN1.2
	15	2,5	TiBN1.3
	15	5	TiBN1.4
	20	2,5	TiBN1.5
	20	5	TiBN1.6
	25	5	TiBN1.7
50	20	2,5	TiBN2.1
	20	5	TiBN2.2
	25	2,5	TiBN2.3
	25	5	TiBN2.4

Two sets of parameters were used for the remelting of the boron nitride aluminium-silicon coating. The first set was conducted at a constant voltage of 60 kV, while the current intensity and the remelting velocity were modified. The second set was realized by using a voltage of 50 kV. The current intensity was varied from 10 mA to 25 mA, and the remelting speed between (2,5 – 5) mm/s. In both cases the process energy was distributed in a single line geometry. The parameters that provided uniformly remelted coating are marked in table 4.3.

4.2.1.2 Penetration depth of the remelted samples

The cross – sections of the remelted TiBN samples are illustrated in figure 4.10.

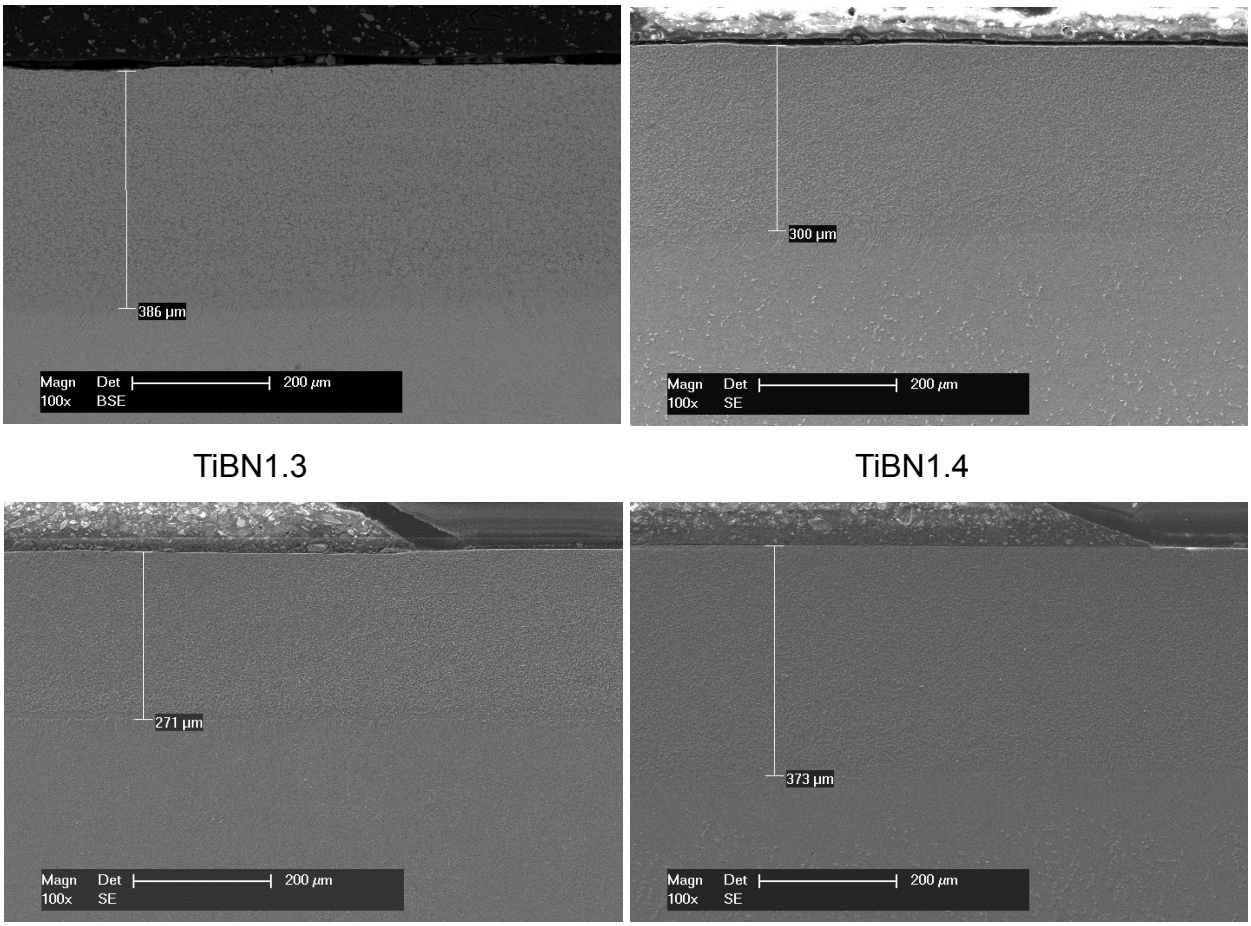

TiBN1.3 TiBN1.4

TiBN2.2 TiBN2.4

Figure 4.10 *Remelted depths of the TiBN samples*

Penetration depths between 270 and 385 μm were obtained through the remelting process. Analyzing the used parameters and the SEM micrographs from figure 4.10, one can observe that by using a lower remelting speed, at constant voltage and current intensity values, the remelting depth is higher (TiBN1.3 vs TiBN1.4). Also, at constant voltage and remelting speed values, the depth of the remelted zone increases with the increase of current intensity (TiBN2.2 vs TiBN2.4). The remelted areas display a high quality, dense structures with no impurities and no agglomeration of unmelted particles [102].

4.2.1.3 Microstructure and phase composition of the TiBN samples

In order to visualize the structures of the remelted zones the samples were etched in a hydrofluoric acid solution. Both EDX and x-ray diffraction were used to identify the phase composition.

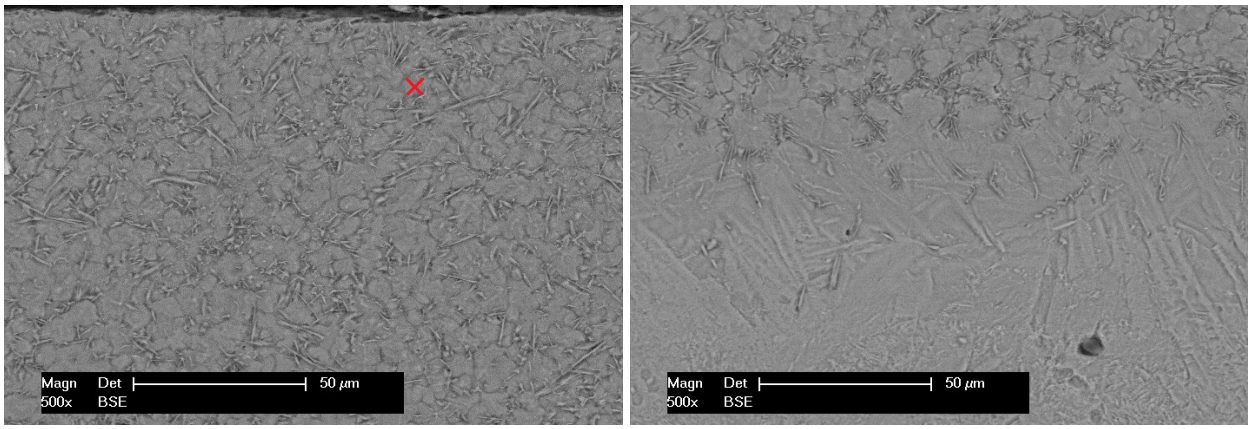

Figure 4.11 *SEM micrographs of the TiBN1.3 sample*

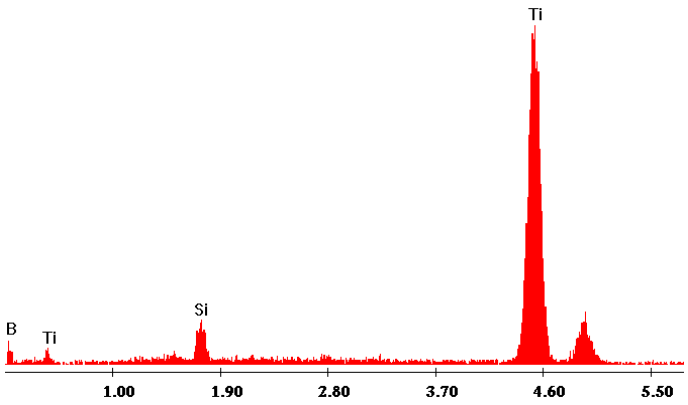

Figure 4.12 *EDX measurement of the light gray phase*

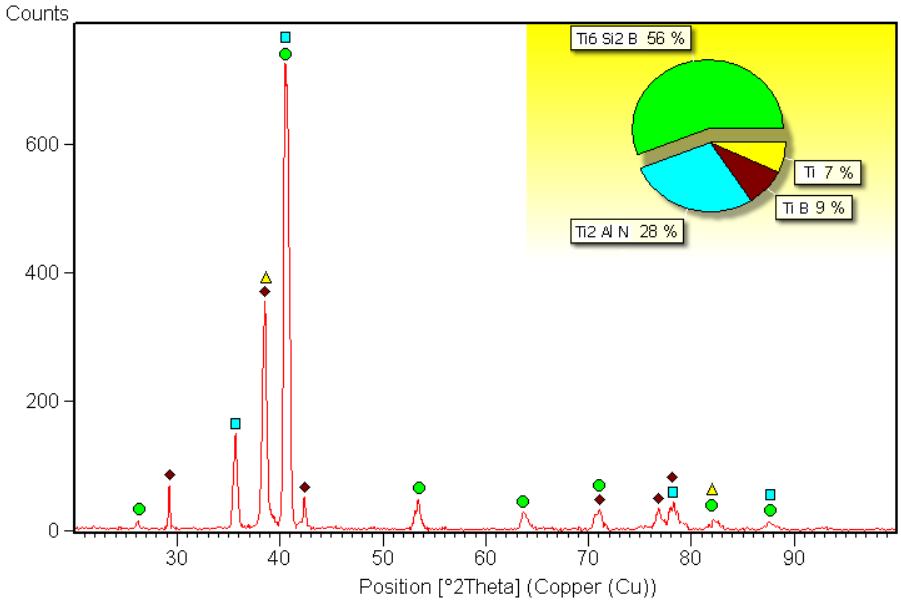

Figure 4.13 *X-Ray diffraction pattern of sample TiBN1.3*

The SEM micrographs (figure 4.11, 4.14, 4.17, 4.20) illustrate the structure of the remelted samples. The EDX analysis reveals that the structures consist of needle-shaped titanium boride (TiB) as well as bright titanium aluminium nitride (Ti_2AlN) and light gray titanium silicon boride (Ti_6Si_2B) spherical phases uniformly distributed in the matrix.

By correlating the SEM micrographs of the alloyed samples and the X-ray diffraction patterns with the process parameters it can be observed that a higher energy density favors the formation of a higher titanium silicon boride content. This, however, also leads to the development of a coarse structure.

Samples TiBN1.4, TiBN2.2 and TiBN2.4 have a considerably lower titanium-silicon boride content along with a significant increase in titanium and titanium-aluminium nitride phase and a moderate enhancement of the titanium boride amount. Furthermore, these samples exhibit a finer microstructure in the alloyed surface. Also, the X-ray diffraction patterns of these samples reveal the formation of a cubic titanium boride (TiB) phase [103].

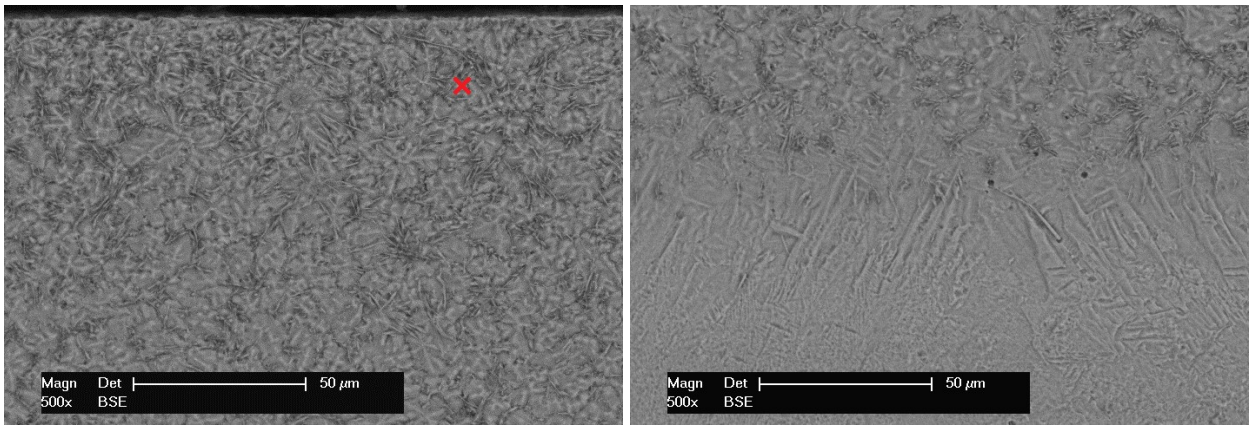

Figure 4.14 *SEM micrographs of the TiBN1.4 sample*

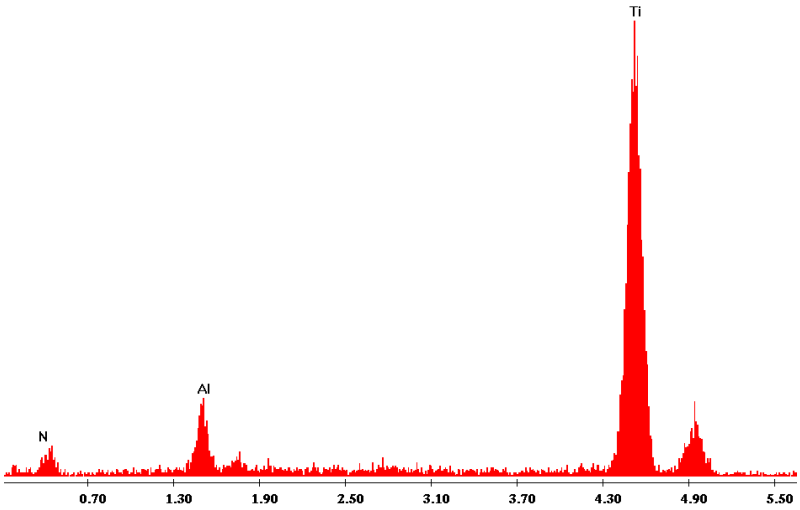

Figure 4.15 *EDX analysis of the bright phase*

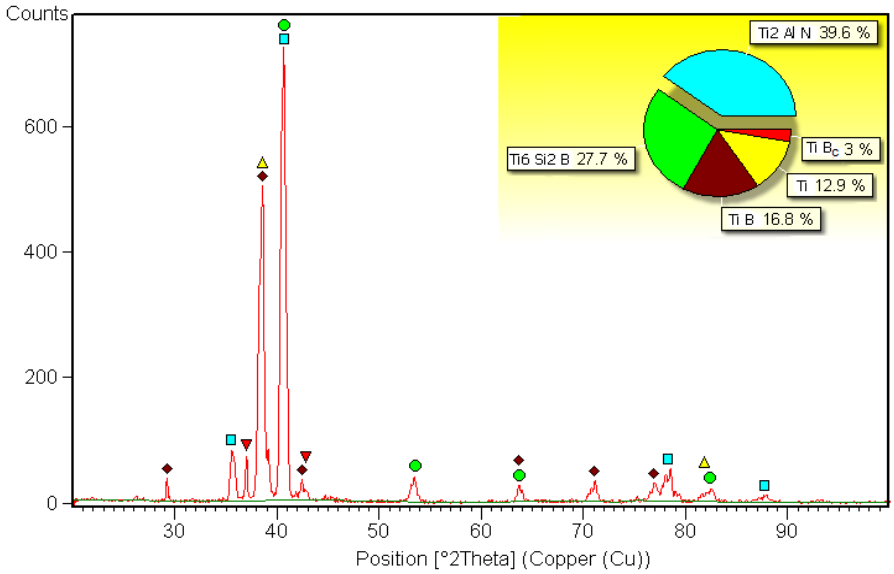

Figure 4.16 *X-Ray diffraction pattern of sample TiBN1.4*

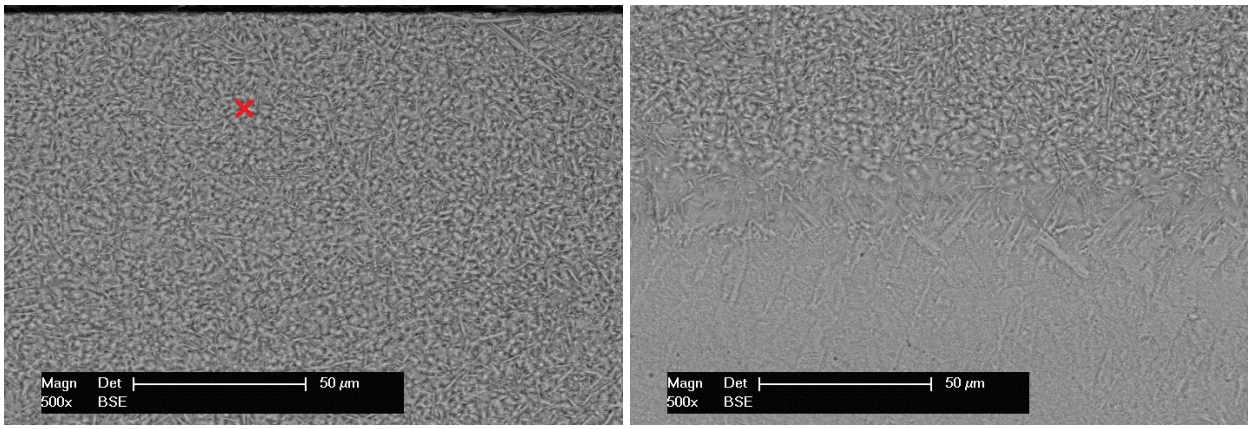

Figure 4.17 *SEM micrographs of the TiBN2.2 sample*

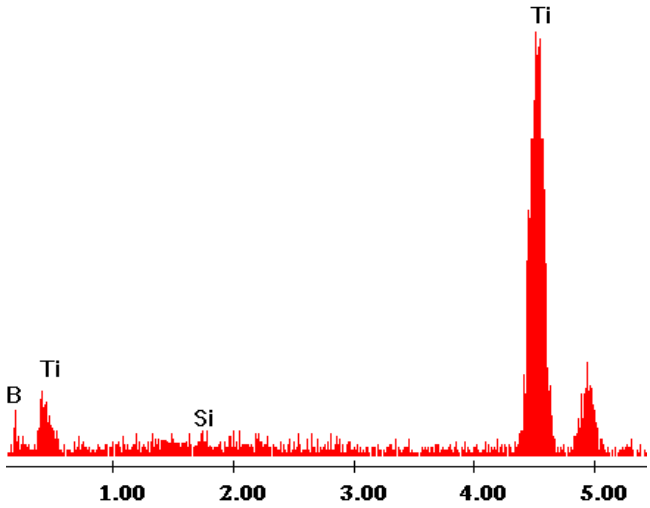

Figure 4.18 *EDX analysis of the needle shaped phase*

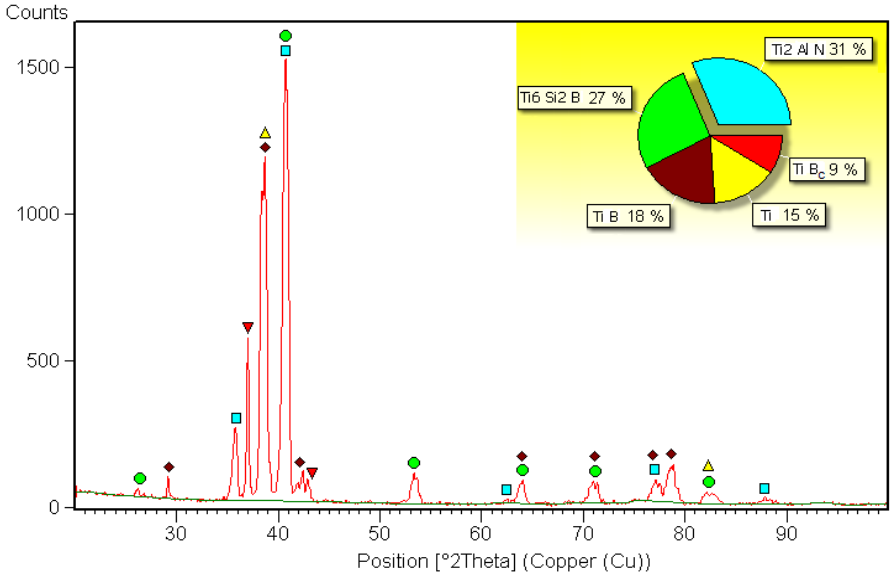

Figure 4.19 *X-Ray diffraction pattern of sample TiBN2.2*

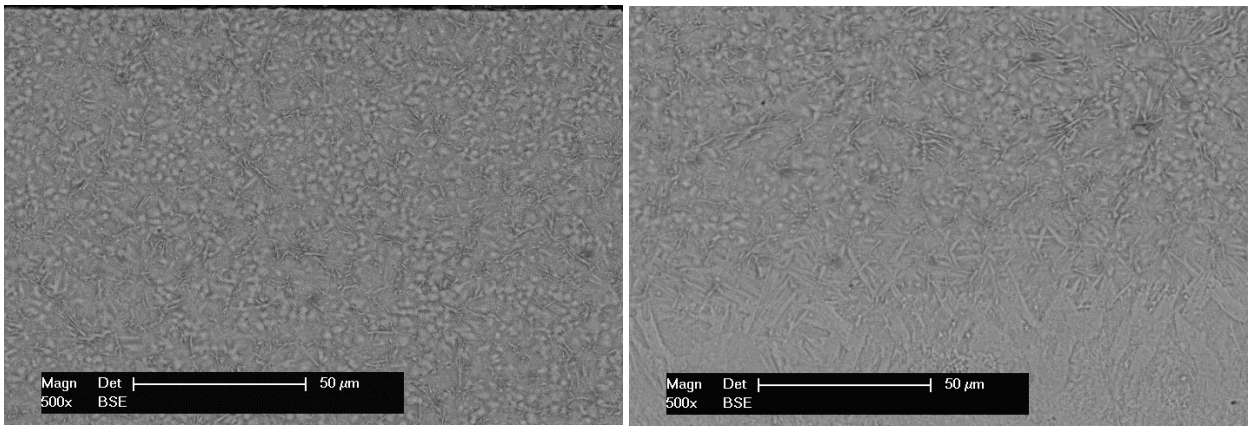

Figure 4.20 *SEM micrographs of the TiBN2.4 sample*

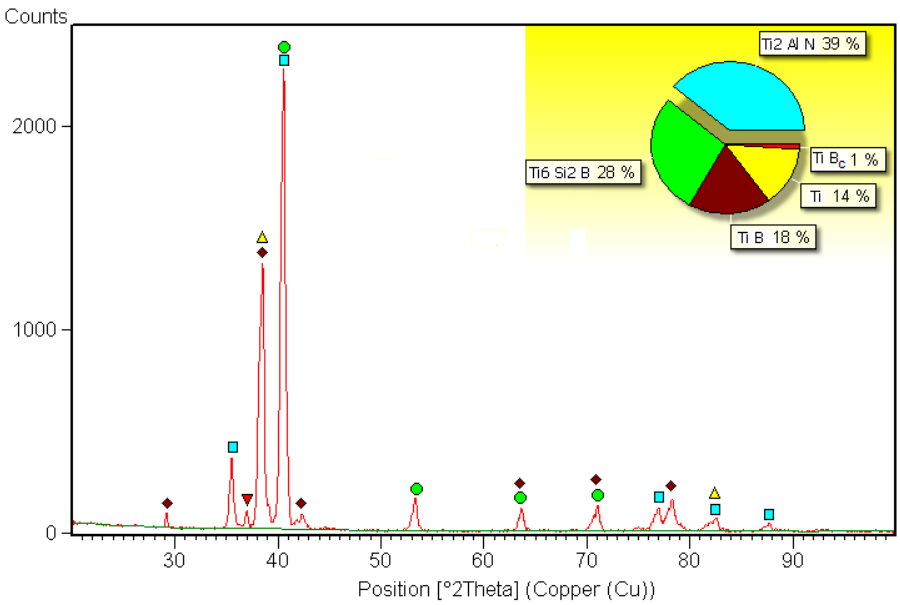

Figure 4.21 *X-ray diffraction pattern of sample TiBN2.4*

An overview of the composition and crystal structures of the phases identified in the TiBN specimens is given in table 4.4.

Table 4.4 *Phase composition of TiBN samples*

	Ti_6Si_2B	Ti_2AlN	TiB	TiB_c	Ti
TiBN1.3	56,00%	28,00%	9,00%	-	7,00%
TiBN1.4	27,70%	39,60%	16,80%	3,00%	12,90%
TiBN2.2	27,00%	31,00%	18,00%	9,00%	15,00%
TiBN2.4	28,00%	39,00%	18,00%	1,00%	14,00%
	hexagonal	***hexagonal***	***orthorombic***	***cubic***	***hexagonal***

4.2.2 Structural modifications in the titanium – tungsten carbide system

4.2.2.1 Remelting parameters

Table 4.5 presents the electron beam remelting parameters of the tungsten carbide cobalt-chromium coating.

Table 4.5 *Remelting parameters of the WC-CoCr coating*

U [kV]	Scan modus	I [mA]	v [mm/s]	Sample
60	line	20	5	TiWC1.1
		20	2,5	TiWC1.2
		25	5	TiWC1.3
		30	5	TiWC1.4
		30	10	TiWC1.5
		30	15	TiWC1.6
		35	15	TiWC1.7
		40	15	TiWC1.8
		40	20	TiWC1.9
		50	20	TiWC1.10
		40	10	TiWC1.11
		35	10	TiWC1.12
		35	8	TiWC1.13
		45	10	TiWC2.1
		40	10	TiWC2.2
		50	10	TiWC2.3
		55	10	TiWC2.4
	field	50	10	TiWC2.5
		55	10	TiWC2.6

The remelting process was conducted at a constant voltage of 60 kV by varying the current intensity from 20 mA to 55 mA and the remelting speed between (2,5 – 20) mm/s. Also, two electron beam energy distribution types were used, namely a line scan and a field scan modus.

4.2.2.2 Penetration depth of the remelted samples

Figure 4.22 illustrates the penetration depths obtained by the remelting of the tungsten carbide cobalt-chromium coating.

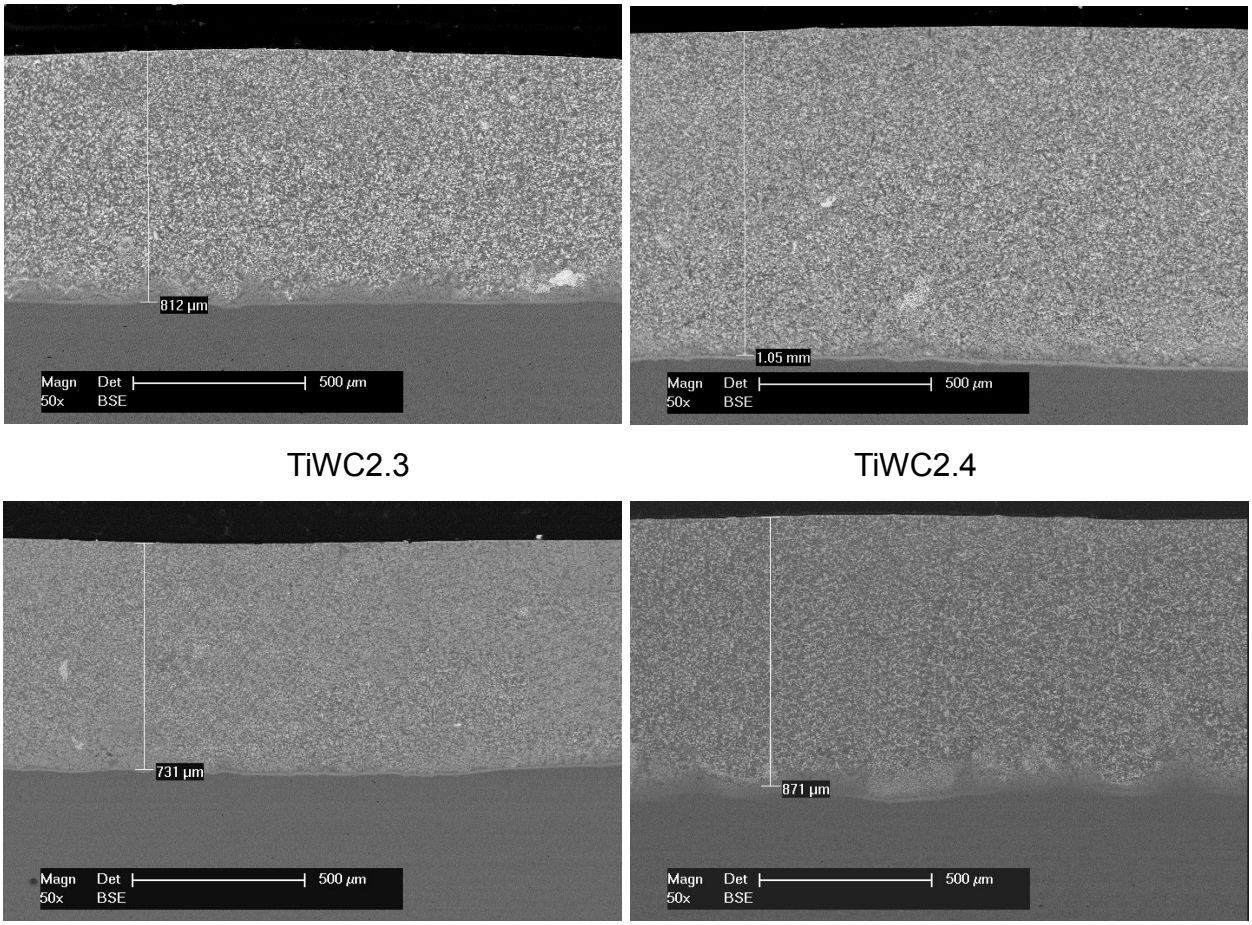

TiWC2.3 TiWC2.4

TiWC2.5 TiWC2.6

Figure 4.22 *Penetration depths of the TiWC samples*

The thickness of the remelted coatings measures up to approximately 800 µm and 1000 µm by the use of a single line scan geometry of the electron beam. The field distribution of the process energy has led to a moderate decrease of the penetration depths, reaching values about 730 µm, respectively 870 µm [104].

4.2.2.3 Microstructure and phase composition of the TiWC samples

Microstructure and phase characterization were performed, as for the TiBN samples, with the help of scanning electron microscopy (SEM), energy dispersive spectroscopy (EDX) and X-ray diffraction.

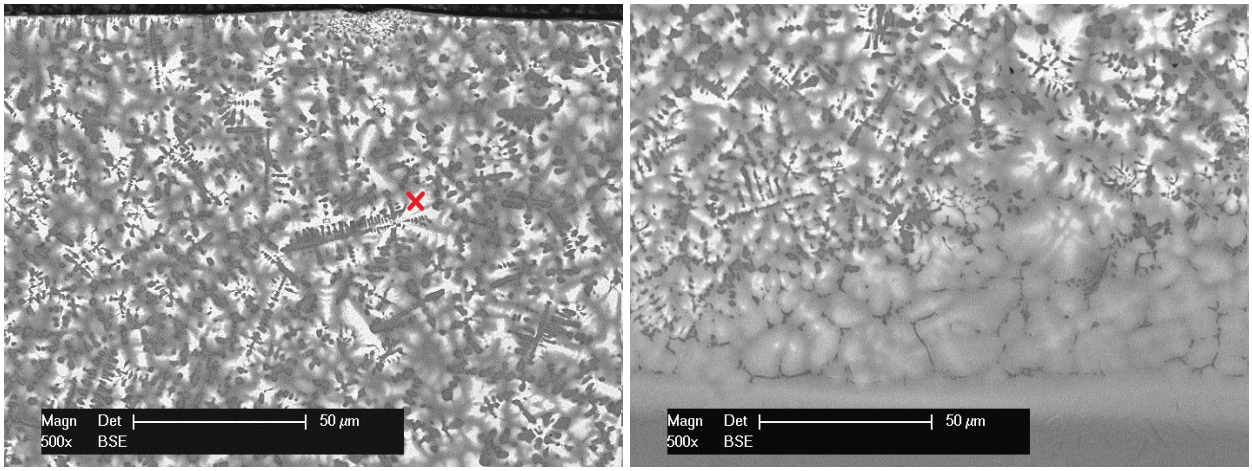

Figure 4.23 *SEM micrographs of the TiWC2.3 sample*

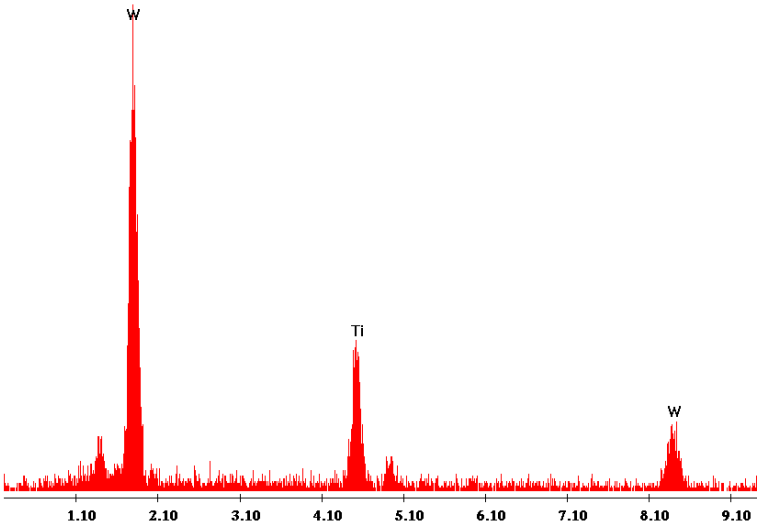

Figure 4.24 *EDX analysis of the bright phase*

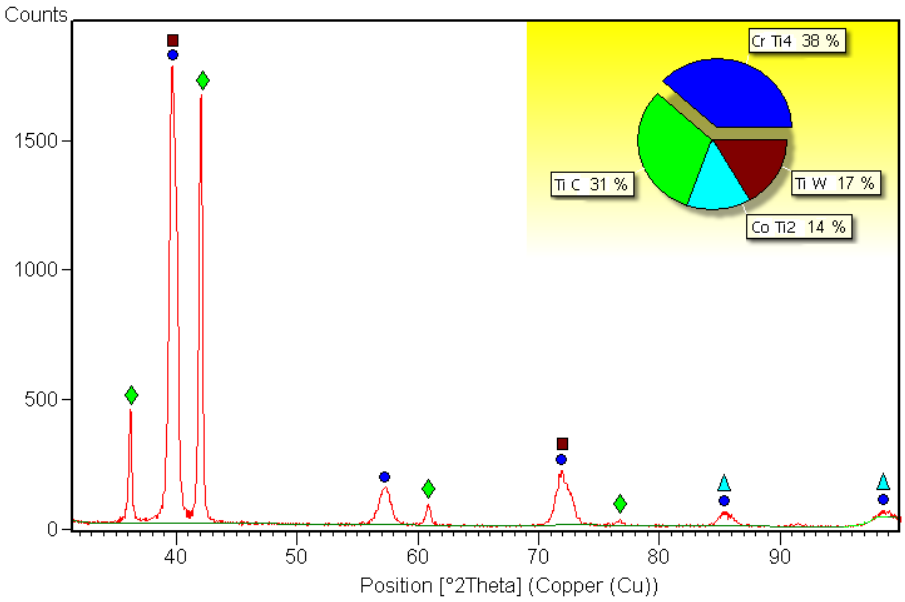

Figure 4.25 *X-ray diffraction pattern of sample TiWC2.3*

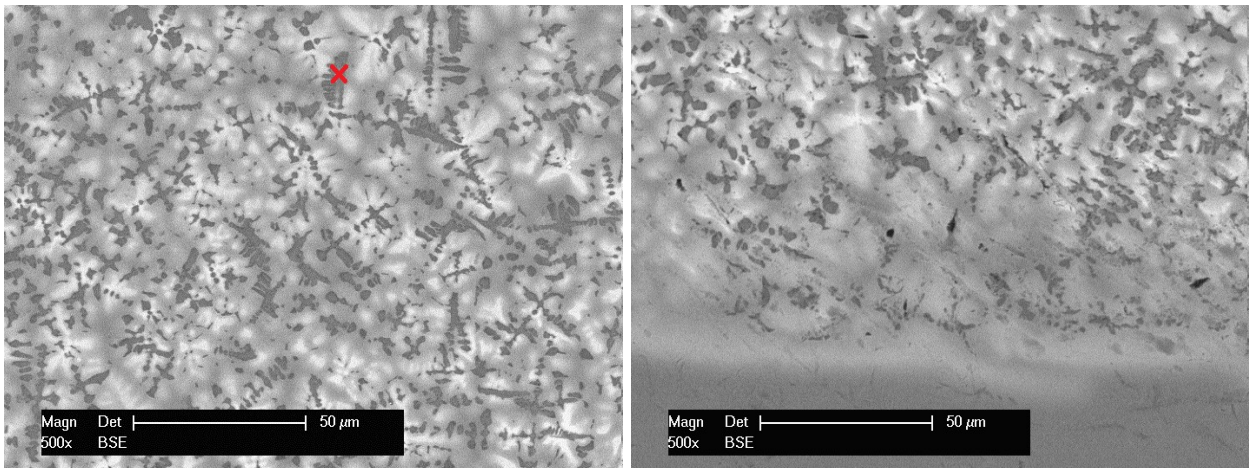

Figure 4.26 *SEM micrographs of the TiWC2.4 sample*

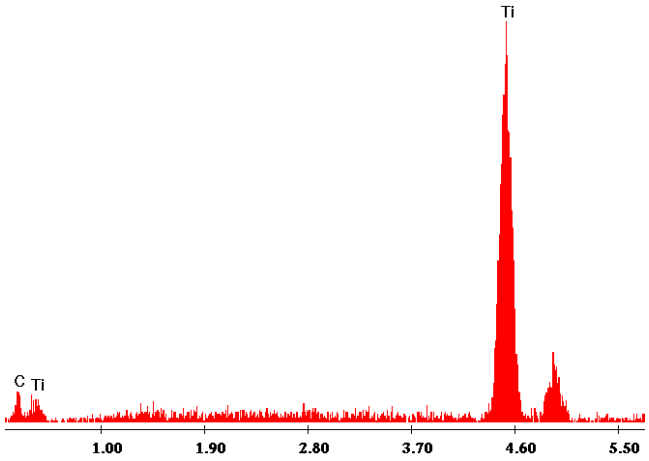

Figure 4.27 *EDX analysis of the dark dendritic phase*

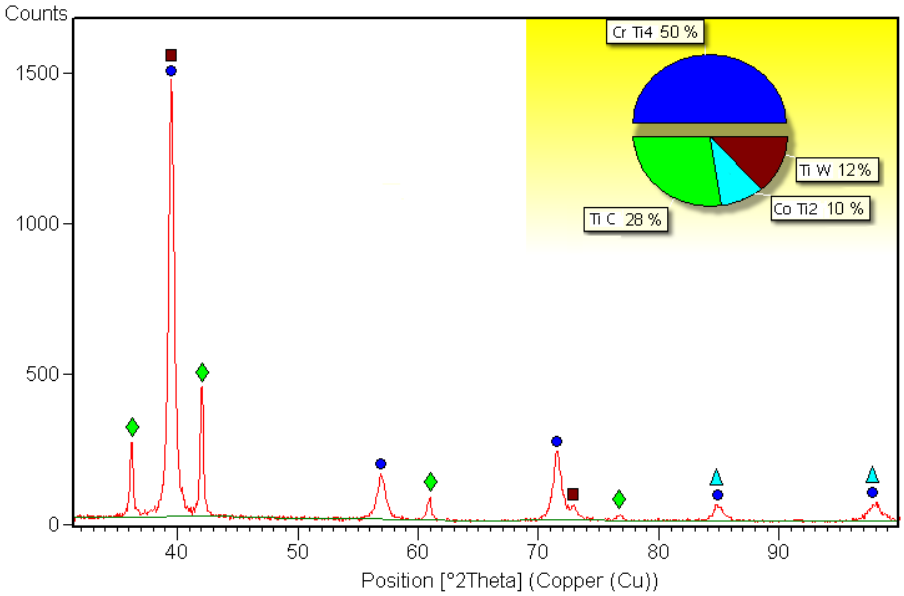

Figure 4.28 *X-ray diffraction pattern of sample TiWC2.4*

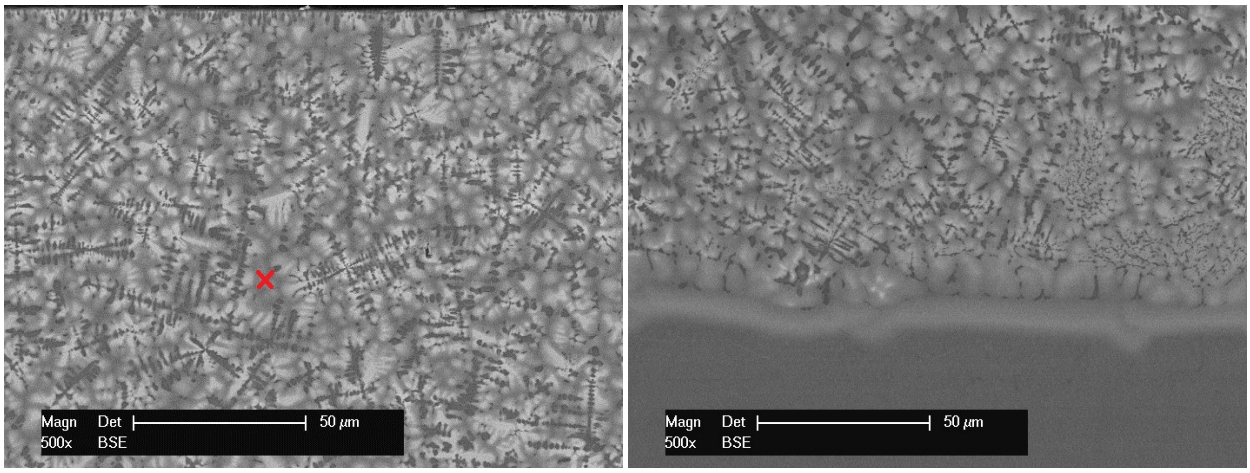

Figure 4.29 *SEM micrographs of the TiWC2.5 sample*

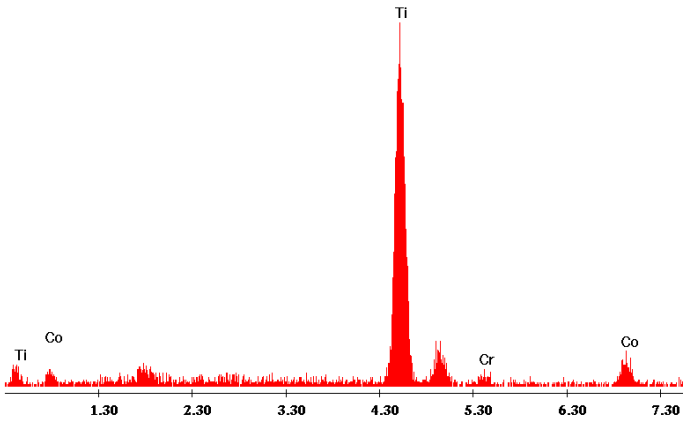

Figure 4.30 *EDX analysis of the dark gray phases*

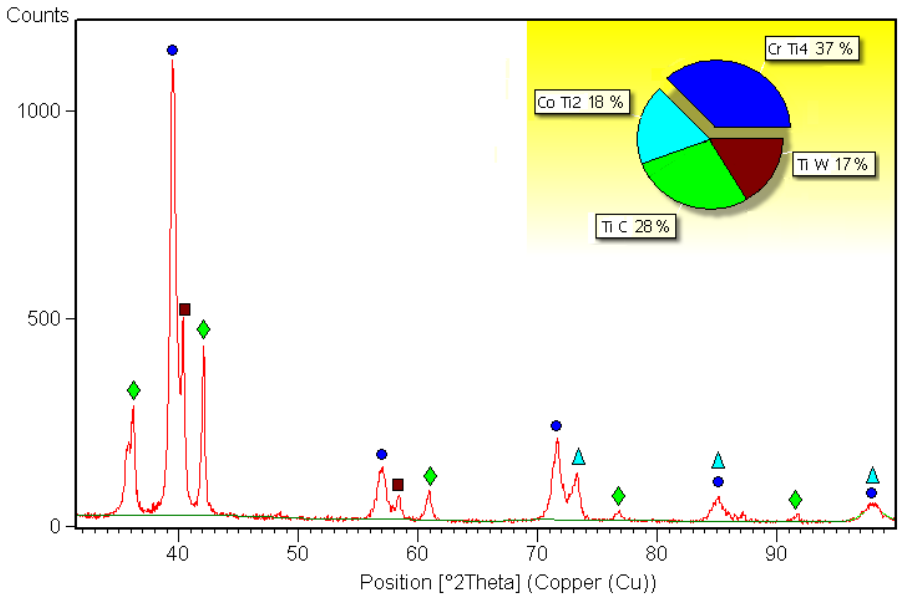

Figure 4.31 *X-ray diffraction pattern of sample TiWC2.5*

The EDX analysis (fig. 4.24) on the bright phase of the remelted zone mostly detects titanium and tungsten. By linking the EDX with the x-ray diffraction patterns it can be concluded that the bright phase in the remelted zones is titanium tungsten (TiW). The structures also consist of a relatively high percentage of dark spherical and dendritic particles. The EDX investigation reveals them to be titanium carbide (TiC). From the EDX analysis in figure 4.30, the dark gray phases can be confirmed to be chromium-titanium ($CrTi_4$) and cobalt-titanium ($CoTi_2$), which represent the biggest share in the alloyed surfaces.

It can be observed that the ratio between the newly formed phases is strongly influenced by the process energy. High energies that imply a greater contribution of the base material to the alloyed surface, encourage the formation of more chromium-titanium phase. Also, the alloying process conducted with a field distribution of the electron beam seems to promote higher cobalt-titanium contents.

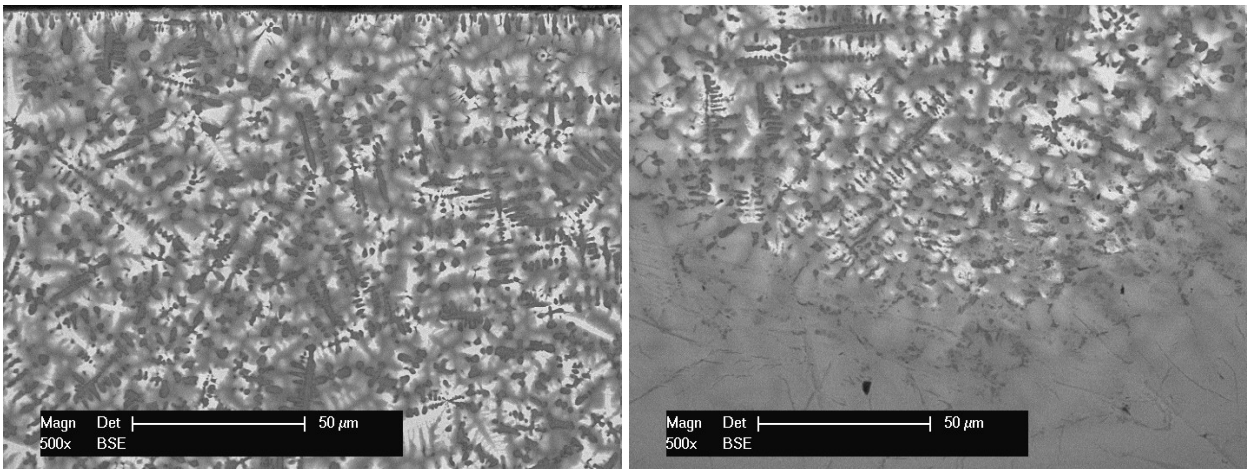

Figure 4.32 *SEM micrographs of the TiWC2.6 sample*

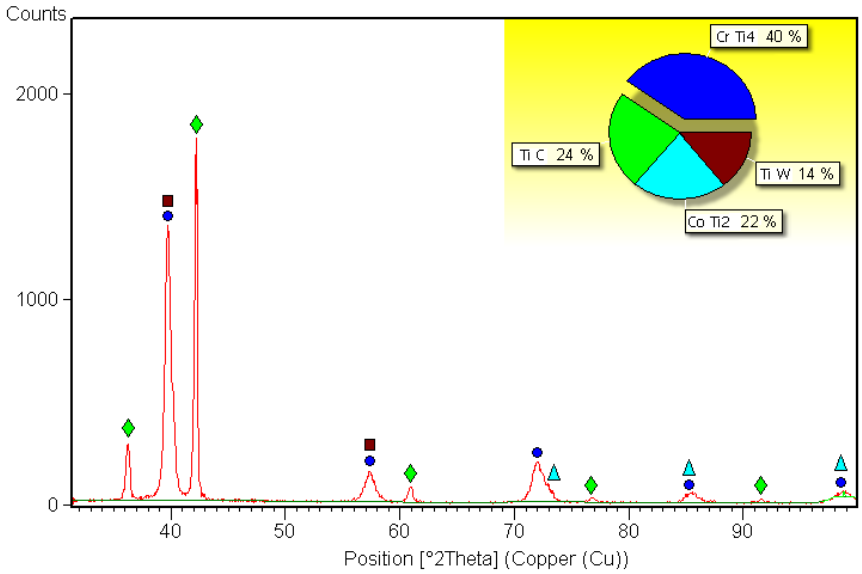

Figure 4.33 *X-ray diffraction pattern of the TiWC2.6 sample*

Table 4.6 summarizes the phase composition of the TiWC samples and the crystal structures of the present phases.

Table 4.6 *Phase composition of TiWC samples*

	$CrTi_4$	TiC	TiW	$CoTi_2$
TiWC2.3	38,00%	31,00%	17,00%	14,00%
TiWC2.4	50,00%	28,00%	12,00%	10,00%
TiWC2.5	37,00%	28,00%	17,00%	18,00%
TiWC2.6	40,00%	24,00%	14,00%	22,00%
	cubic	***cubic***	***cubic***	***cubic***

4.3 Tribological and corrosion behavior of the alloyed surfaces

4.3.1 Surface properties of the TiBN samples

4.3.1.1 Vickers microhardness

Vickers HV 0.3 was measured to determine the microhardness of the alloyed samples. The hardness was measured from the surface down to the substrate and the results are shown in figure 4.34. The overall bulk hardness values are presented in the histogram from figure 4.35.

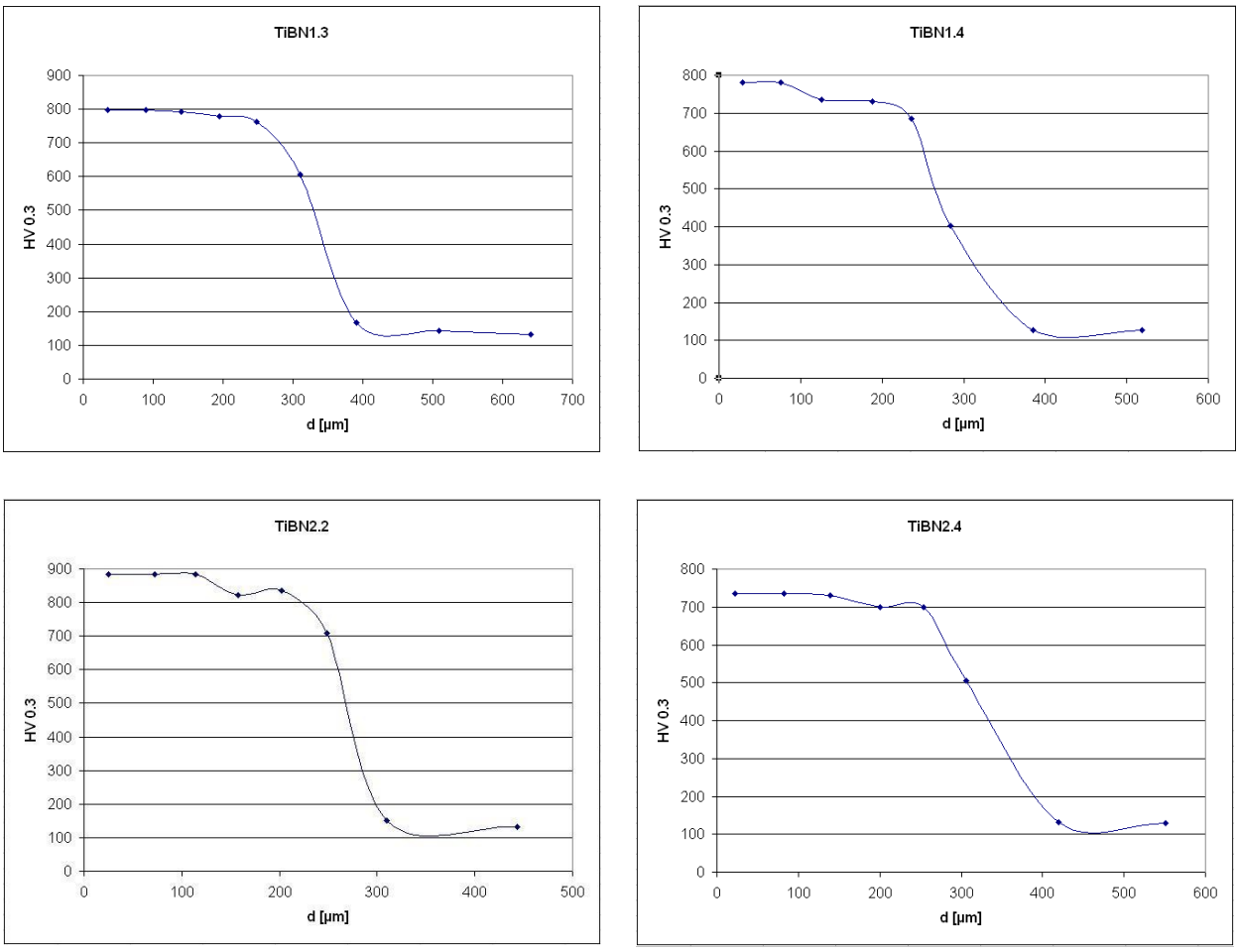

Figure 4.34 *Hardness gradient of the TiBN samples*

The hardness of the surface alloyed TiBN samples ranges from about 736 to 883 HV0.3. The hardness values decrease towards the interfacial region, dropping to about 400 HV0.3. The high hardness values are attributed to the boride and nitride phases formed during the alloying process. Sample TiBN2.2 which has the highest content of cubic titanium boride exhibits the highest hardness values.

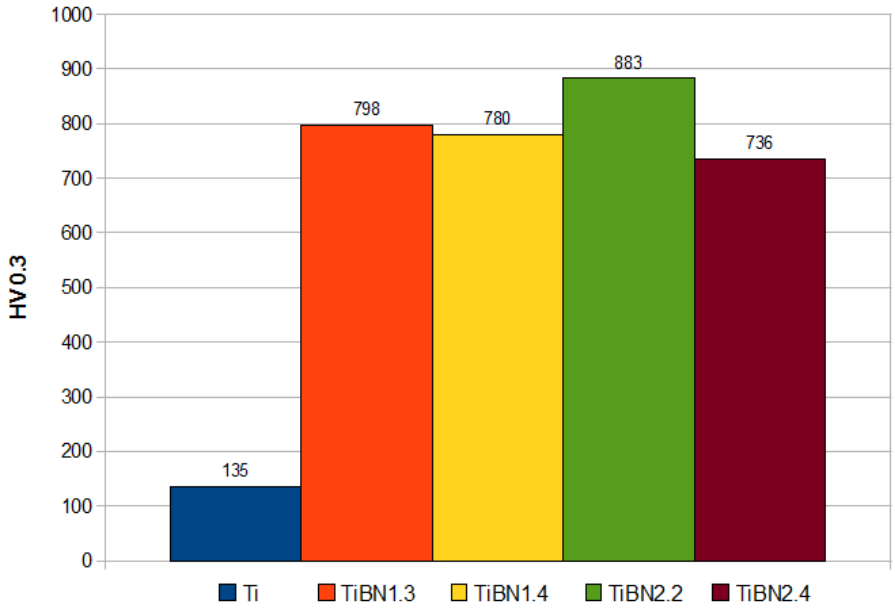

Figure 4.35 *Overall bulk microhardness of the TIBN samples*

4.3.1.2 Friction coefficient and sliding wear rate of the alloyed TiBN samples

The friction coefficients and the sliding wear rate were determined with the pin-on-disc test. The samples were tested for a 1000 m distance, with a 20 m/s velocity under a 5 N load against a WC-Co ball. The friction coefficients were recorded by measuring the deflection of the tribometers elastic arm. The friction coefficients are presented in figure 4.36 to 4.40.

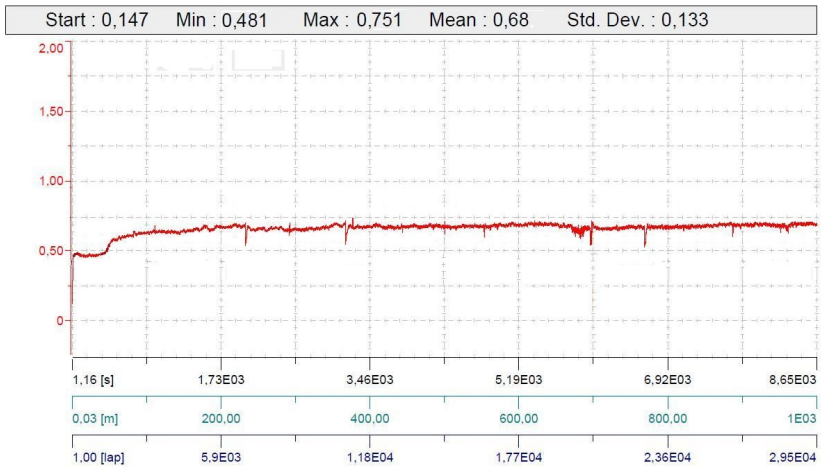

Figure 4.36 *Friction coefficient of the titanium substrate*

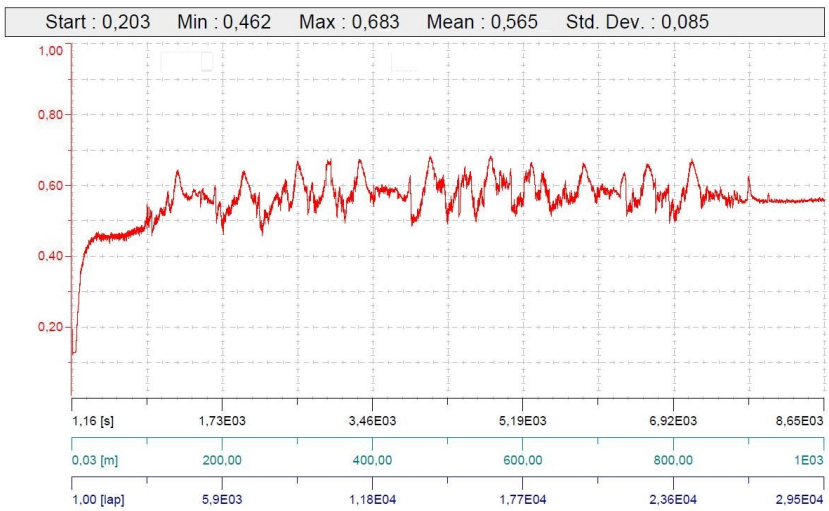

Figure 4.37 *Friction coefficient of sample TiBN1.3*

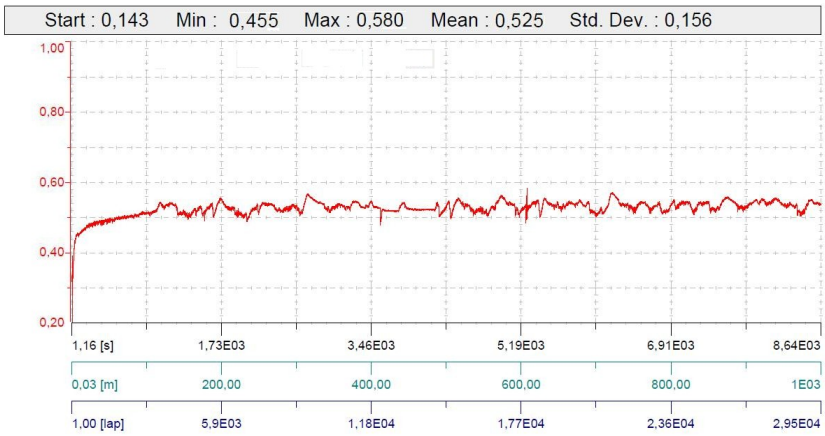

Figure 4.38 *Friction coefficient of sample TiBN1.4*

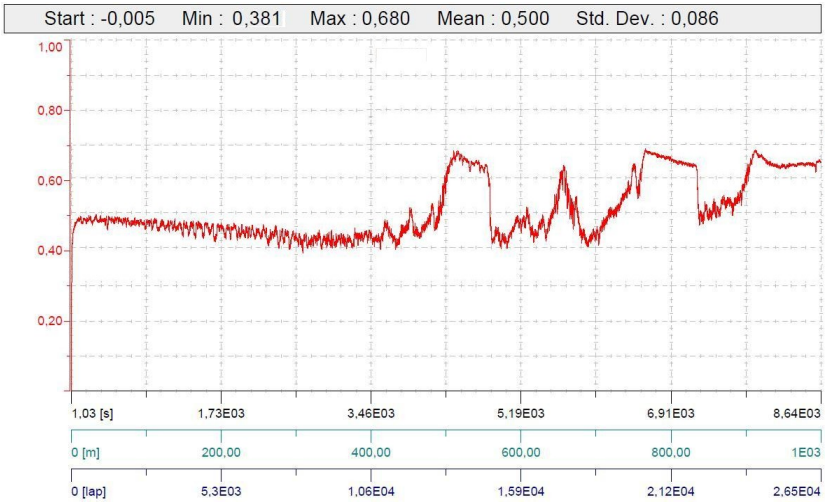

Figure 4.39 *Friction coefficient of sample TiBN2.2*

Figure 4.40 *Friction coefficient of sample TiBN2.4*

The measurements show that the TiBN alloyed surfaces exhibit a lower but more rugged coefficient of friction in comparison with the base material, recorded values being between 0,46 and 0,56. The lowest values for the friction coefficient of samples TiBN2.2 and TiBN2.4 could be attributed to the finer microstructure of these samples, which leads to lower friction forces in the contact [105]. The minimum, maximum and mean values of the friction coefficients are presented in table 4.7.

Table 4.7 *Friction coefficient values of the TiBN samples*

	μ_{min}	μ_{max}	μ_{med}
Ti	0,48	0,751	0,680
TiBN1.3	0,462	0,683	0,565
TiBN1.4	0,455	0,580	0,525
TiBN2.2	0,381	0,680	0,500
TiBN2.4	0,345	0,565	0,460

The sliding wear rates were determined with the aid of the TRIBOX software, by introducing the measured area of the wear tracks and the diagonals of the testing balls worn cap.

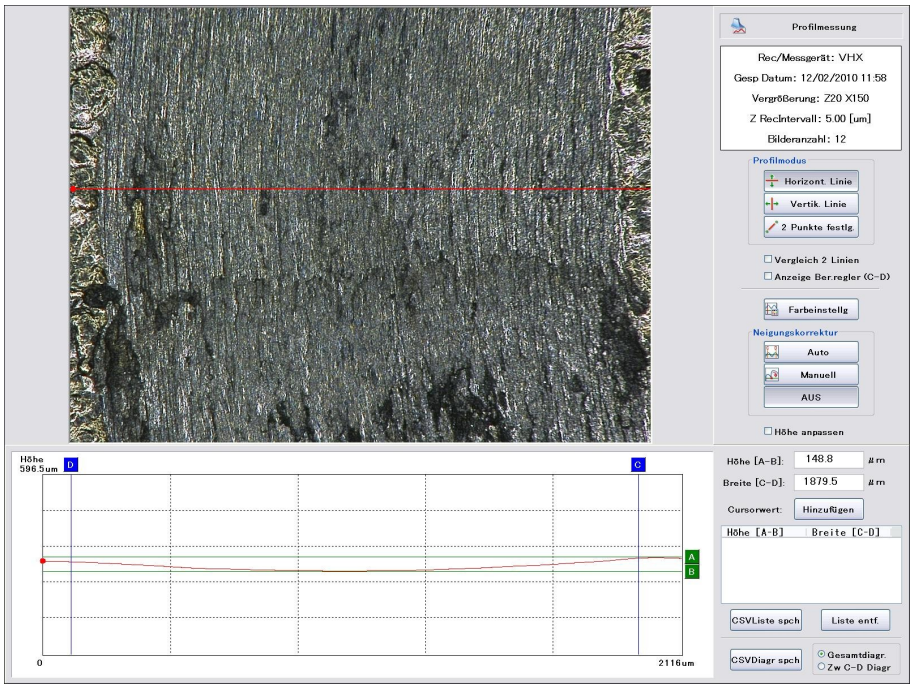

Figure 4.41 *Wear track of the titanium substrate*

The wear track measurements were performed on a digital microscope. The wear track on the titanium substrate together with the measured height and lengths of the wear track are illustrated in figure 4.41. Of course, no wear cap was visible on the testing ball.

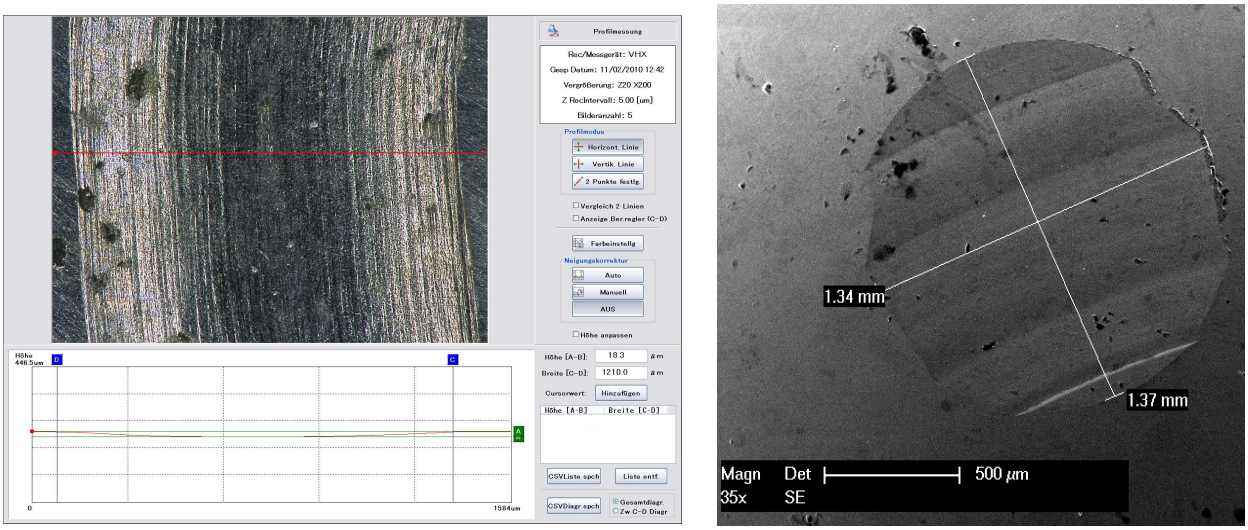

Figure 4.42 *Wear track and ball wear of sample TiBN1.3*

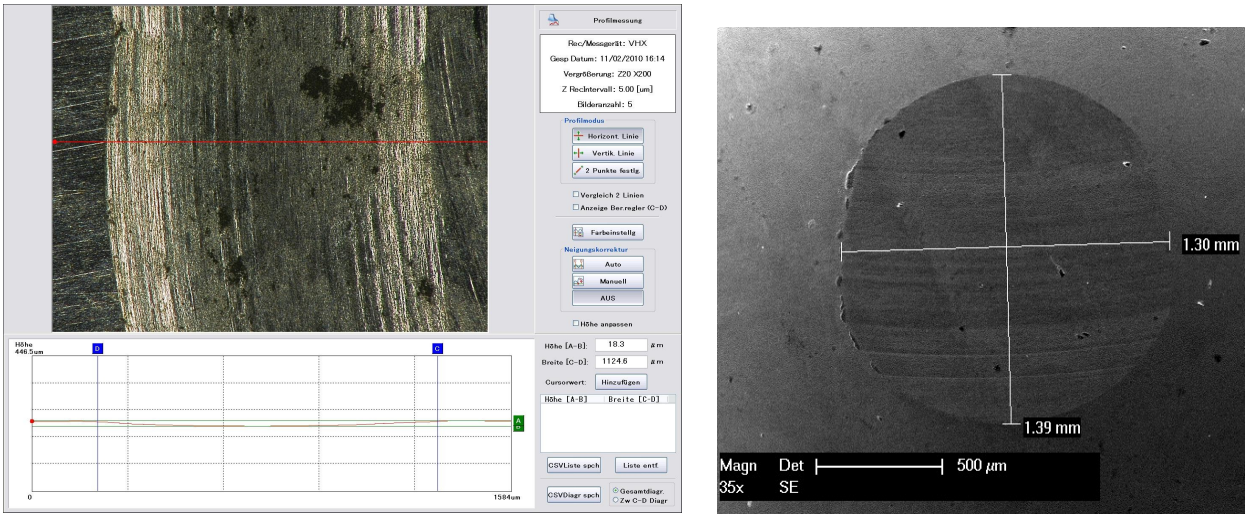

Figure 4.43 *Wear track and ball wear of sample TiBN1.4*

As expected, a higher hardness of the tested surfaces leads to a higher material removal from the testing ball along with a preferential wear of the alloyed surfaces (figures 4.42 to 4.45). A uniformly worn track was observed at sample TiBN2.4 which possesses the lowest friction coefficient of all samples.

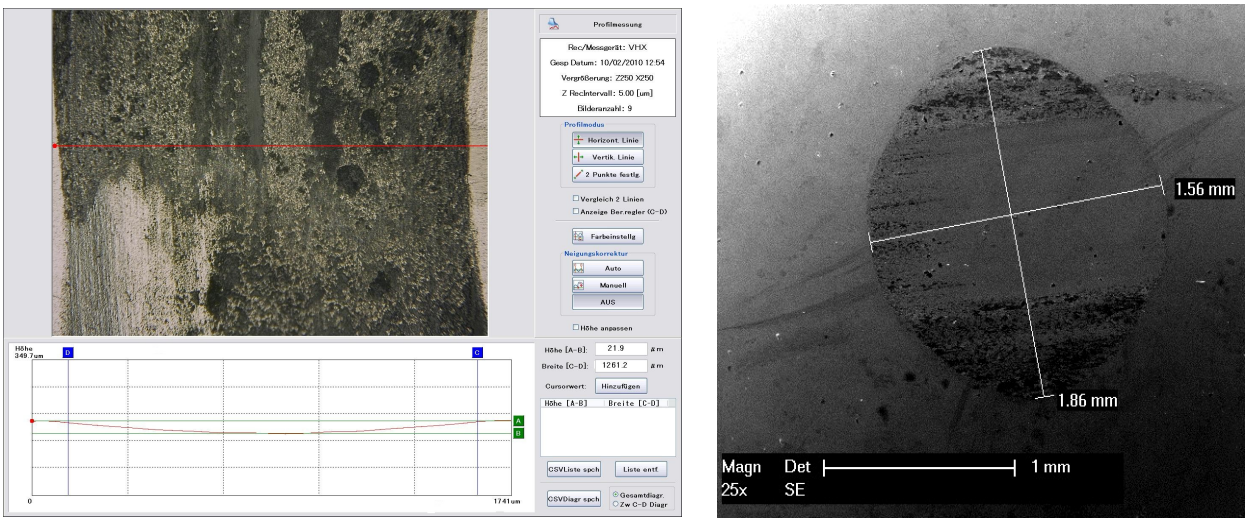

Figure 4.44 *Wear track and ball wear of sample TiBN2.2*

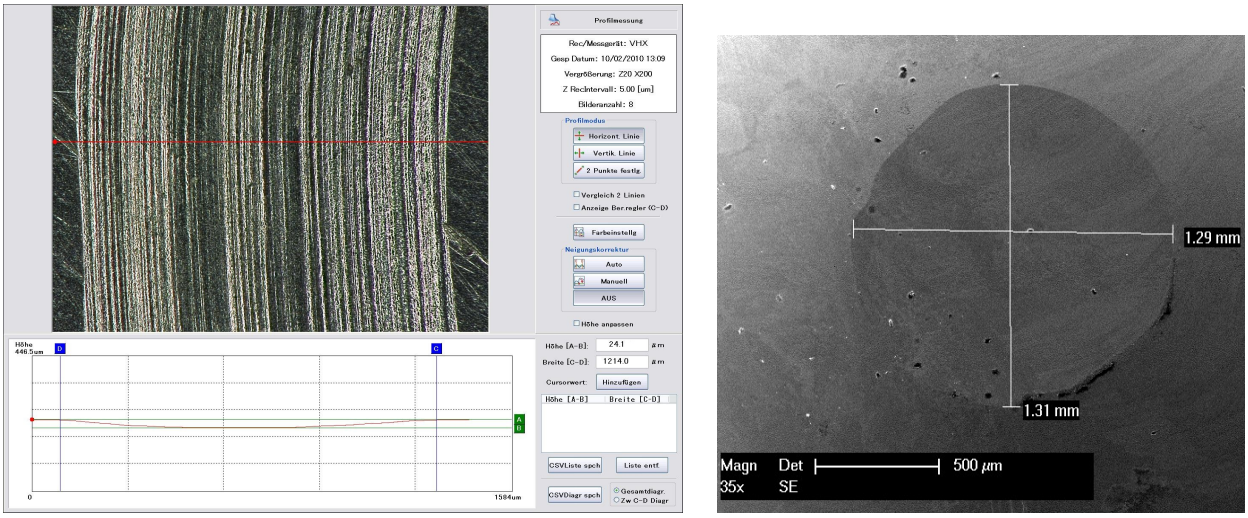

Figure 4.45 *Wear track and ball wear of sample TiBN2.4*

A summary of the wear track measurements of the tested samples, as well as the ball wear and calculated wear rates are presented in table 4.8.

Table 4.8 *Wear measurements of the TiBN samples*

Sample	h [µm]	s [µm]	A [µm²]	Ball wear diagonals [µm]	Wear rate [10^{-5} mm³/Nm]
Ti	148,8	1879,5	187141	-	126,8
TiBN1.3	18,3	1210	14764	1340 x 1370	9,29
TiBN1.4	18,3	1124,6	13722	1300 x 1390	8,64
TiBN2.2	21,9	1261,2	18417	1860 x 1560	13,89
TiBN2.4	24,1	1214	19580	1310 x 1290	14,77

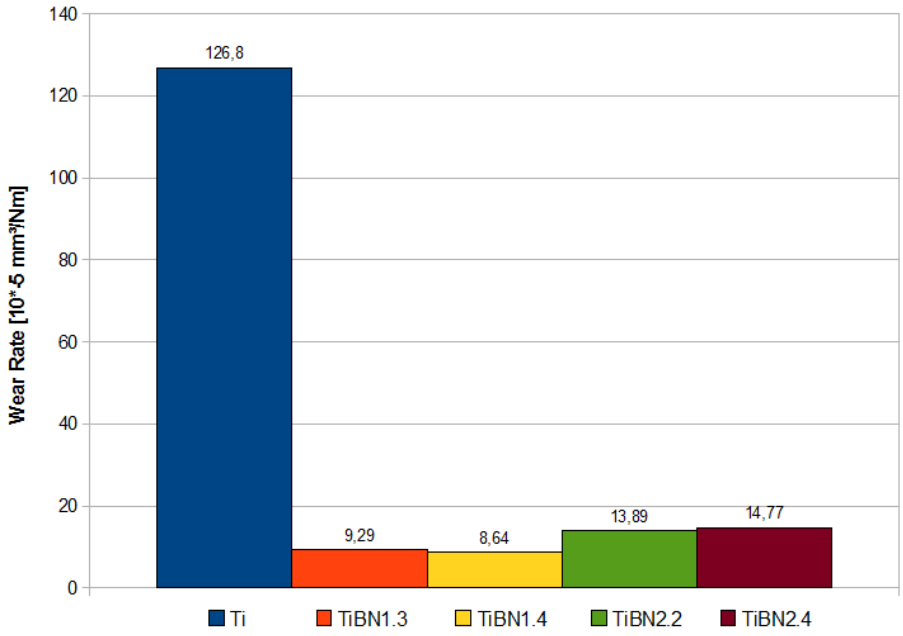

Figure 4.46 *Wear rate histogram of the TiBN samples*

The histogram from figure 4.46 shows a major improvement of the wear resistance when compared with the titanium substrate. This can be assigned to the hard titanium-aluminium nitride, titanium-silicon boride and titanium boride phases. The lower wear rate of sample TiBN1.4 can be explained by the higher Ti_2AlN content, coupled with a moderate volume of TiB. Despite the higher hardness value of the TiBN2.2 sample (highest volume of cubic titanium boride), the wear behavior is strongly influenced by the high titanium content in the alloyed zone, the sample exhibiting a higher wear rate as the samples with lower titanium content.

4.3.1.3 Corrosion behavior of the alloyed TiBN samples

The corrosion behavior of the alloyed samples was investigated by electrochemical testing in 10^{-3} H_2SO_4 solution. A calomel electrode was used as reference electrode, a platinum electrode as the auxiliary electrode and the samples represented the working electrode. The samples were polarized in a potential interval from – 1500 mV to +1500 mV, applied between the calomel electrode and the working electrode.

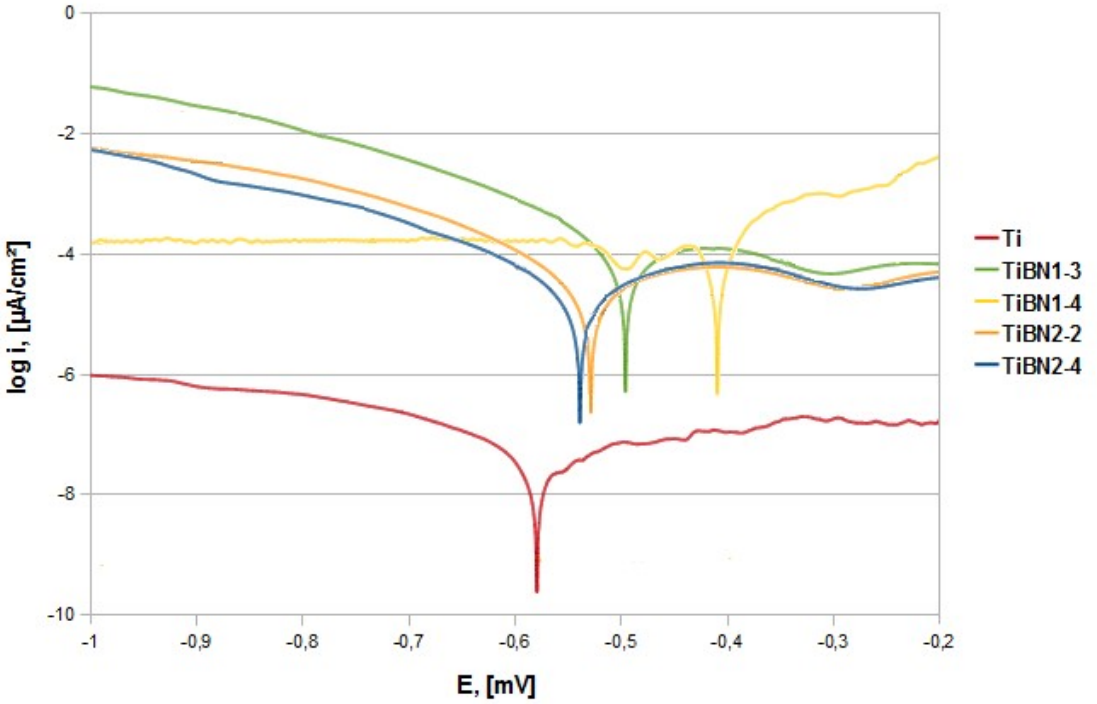

Figure 4.47 *Polarization curves of the TiBN samples*

The rates of corrosion i_{corr}, expressed in current density at the corrosion potential E_{corr} of the tested samples are presented in table 4.9.

Table 4.9 *Corrosion values of the tested TiBN samples*

	Ti	TiBN1.3	TiBN1.4	TiBN2.2	TiBN2.4
E_{corr} [mV]	-576,3	-493,1	-409,4	-525,7	-536,1
i_{corr} [µA/cm²]	0,0061	1,927	1,799	1,596	1,382

As expected, the results presented in table 4.9 and the polarization curves illustrated in figure 4.47 show higher corrosion rates of the alloyed surfaces as that of the base material, i_{corr} raising from 0,0061 µA/cm² to values of 1,927 µA/cm². Also, the corrosion rates of the alloyed surfaces are influenced by the titanium content, the samples with a higher percentage of titanium in the alloyed zone, recording slightly lower corrosion rate values.

4.3.2 Surface properties of the TiWC samples

4.3.2.1 Vickers microhardness

The HV 0.3 hardness values of the TiWC samples were determined, and the hardness gradient for each sample is presented in figure 4.48. The overall bulk hardness values are illustrated in figure 4.49.

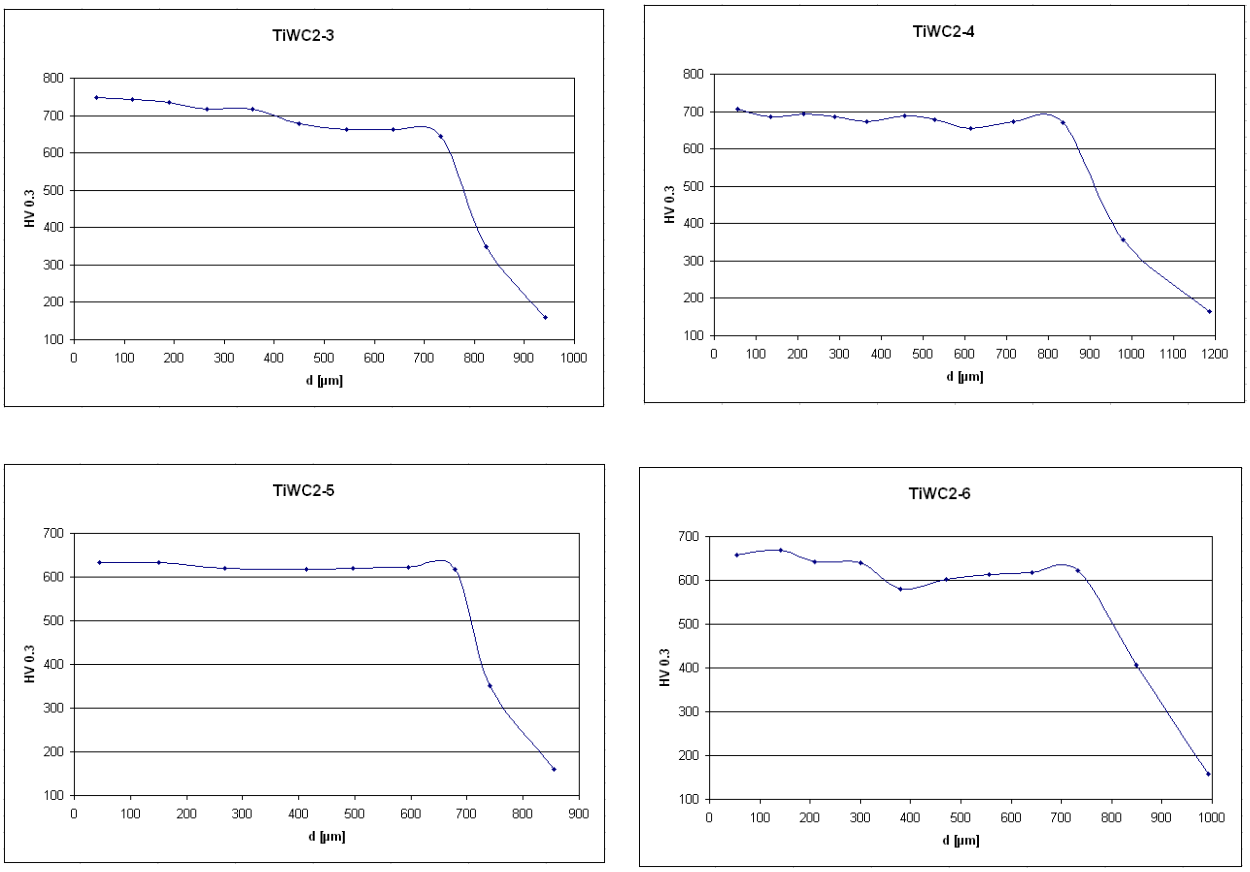

Figure 4.48 *Hardness gradient of the TiWC samples*

The hardness values of the TiWC samples range from 643 HV 0.3 to 748 HV 0.3 at the surface of the alloyed zones and decreases to approximately 350 HV 0.3 at the interface. The relatively high hardness values are due to the presence of the hard titanium carbide phase.

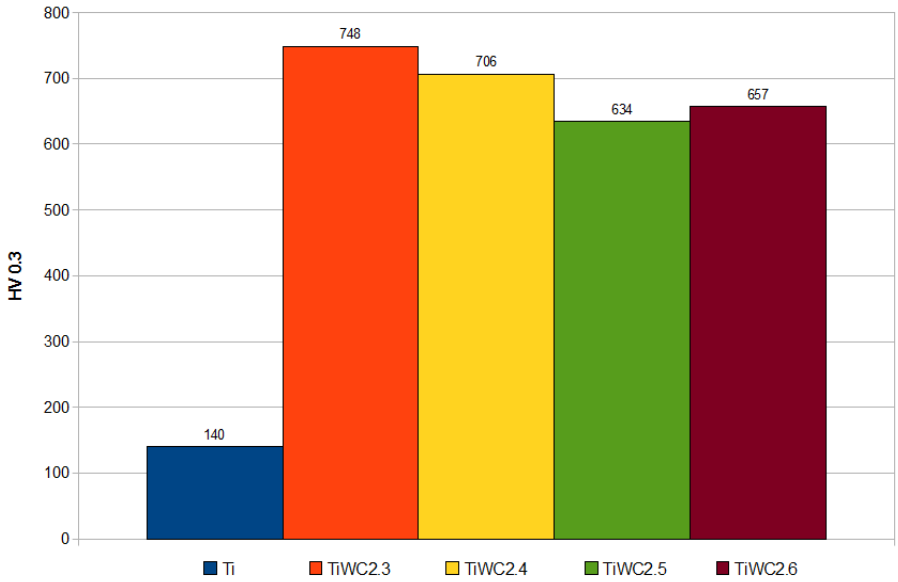

Figure 4.49 *Overall bulk hardness of the TiWC samples*

Hardness measurements of samples TiWC2.5 and TiWC2.6 reveal that the formation of higher quantities of cobalt-titanium ($CoTi_2$) leads to a decrease of the surface hardness.

4.3.2.2 Friction coefficient and sliding wear rate of the alloyed TiWC samples

The coefficient of friction and wear rate determination of the TiWC samples were conducted in identical conditions as for the TiBN samples, namely for a distance of 1000 m, with a 20 m/min velocity and under a 5 N load. The testing body was also a WC-Co ball. The measured friction coefficients of the TiWC samples are illustrated in figures 4.50 to 4.53.

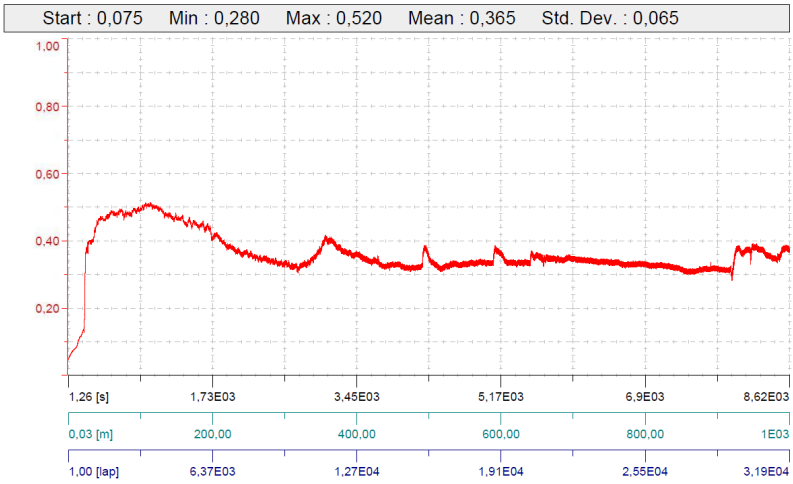

Figure 4.50 *Friction coefficient of sample TiWC2.3*

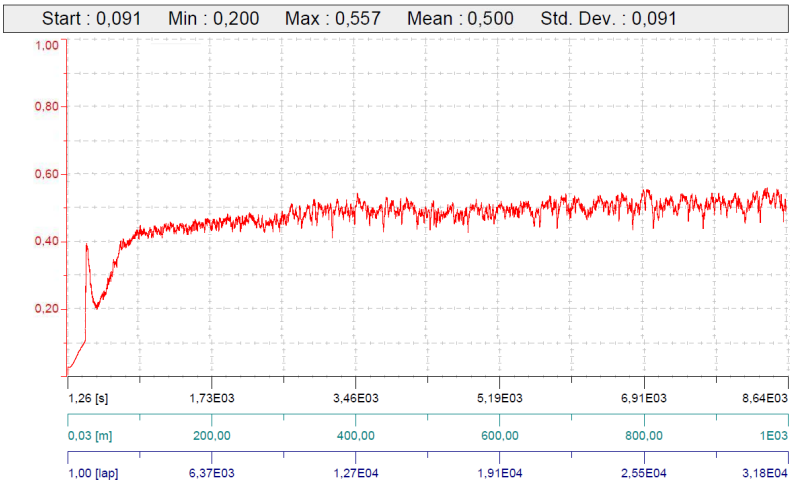

Figure 4.51 *Friction coefficient of sample TiWC2.4*

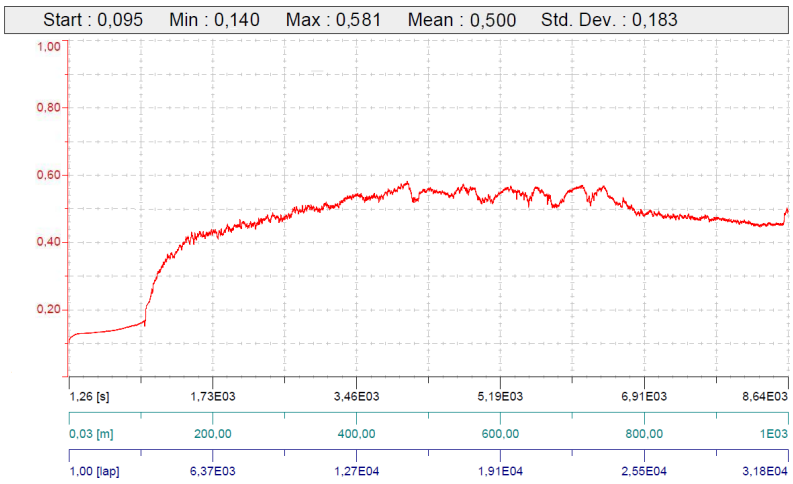

Figure 4.52 *Friction coefficient of sample TiWC2.5*

The measurements illustrated in figures 4.50 to 4.53 indicate that the alloyed TiWC surfaces exhibit lower friction coefficients as that of pure titanium. A reduction of almost 50% of the friction coefficient can be noted for samples TiWC2.3 and TiWC2.6.

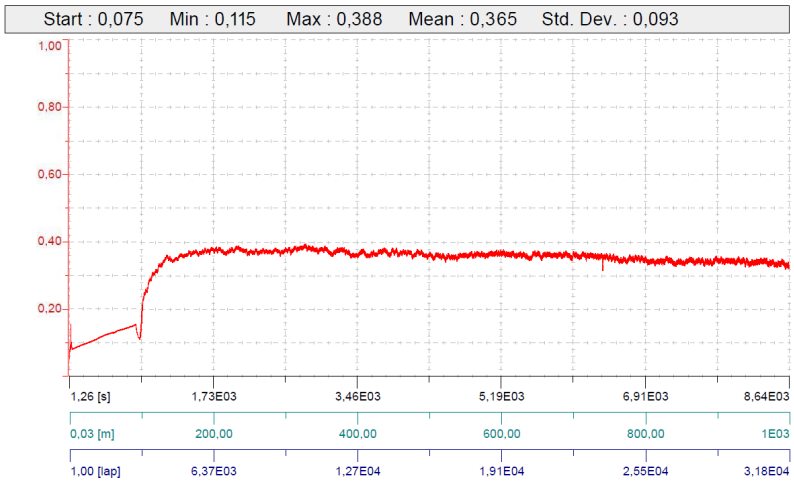

Figure 4.53 *Friction coefficient of sample TiWC2.6*

The minimum, maximum and mean values of the friction coefficients are presented in table 4.10.

Table 4.10 *Friction coefficient values of the TiWC samples*

	μ_{min}	μ_{max}	μ_{med}
Ti	0,482	0,751	0,680
TiWC2.3	0,280	0,520	0,365
TiWC2.4	0,200	0,557	0,500
TiWC2.5	0,140	0,581	0,500
TiWC2.6	0,115	0,388	0,365

Figures 4.54 to 4.57 represent the wear track measurements and ball wear occurred by the wear behavior testing of the TiWC samples.

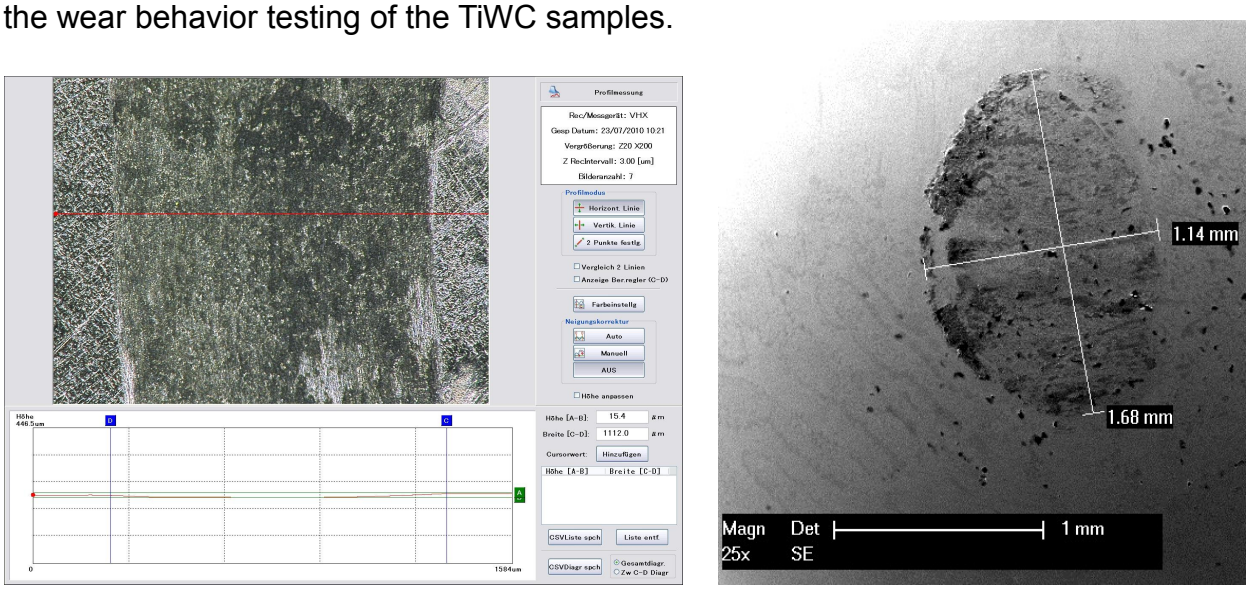

Figure 4.54 *Wear track and ball wear by sample TiWC2.3*

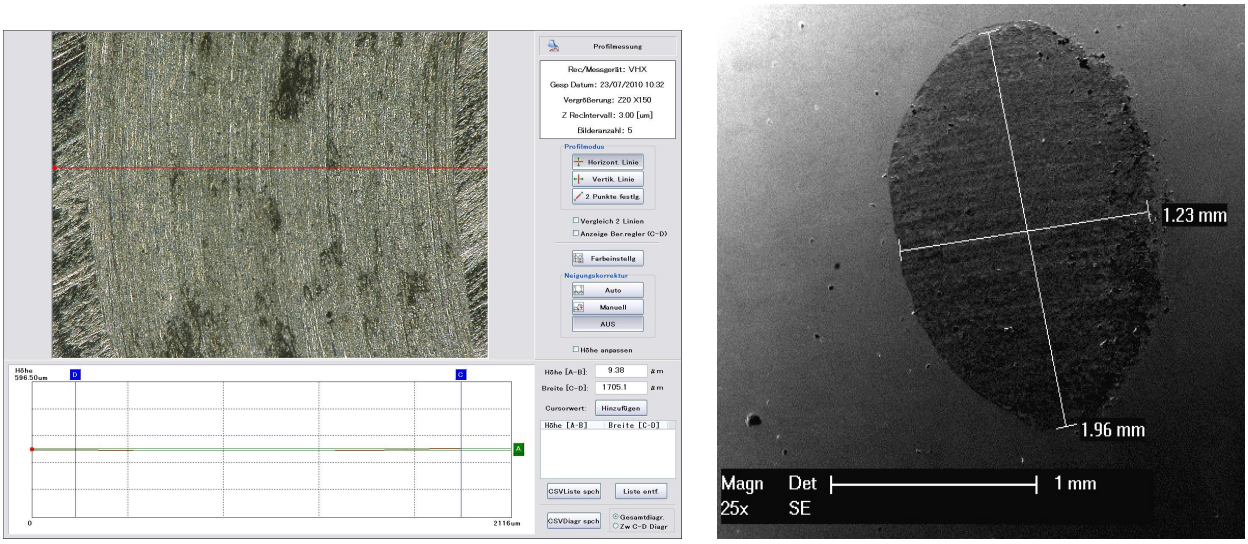

Figure 4.55 *Wear track and ball wear by sample TiWC2.4*

The lower friction coefficients of the TiWC samples resulted in reduced wear in the depth of the alloyed surfaces, the wear track measurements indicating wear grooves with a depth as low as 9,38 μm. However, this has led to a pronounced material removal from the plane surface. This is also confirmed by the relatively wide contact surface visible on the testing balls.

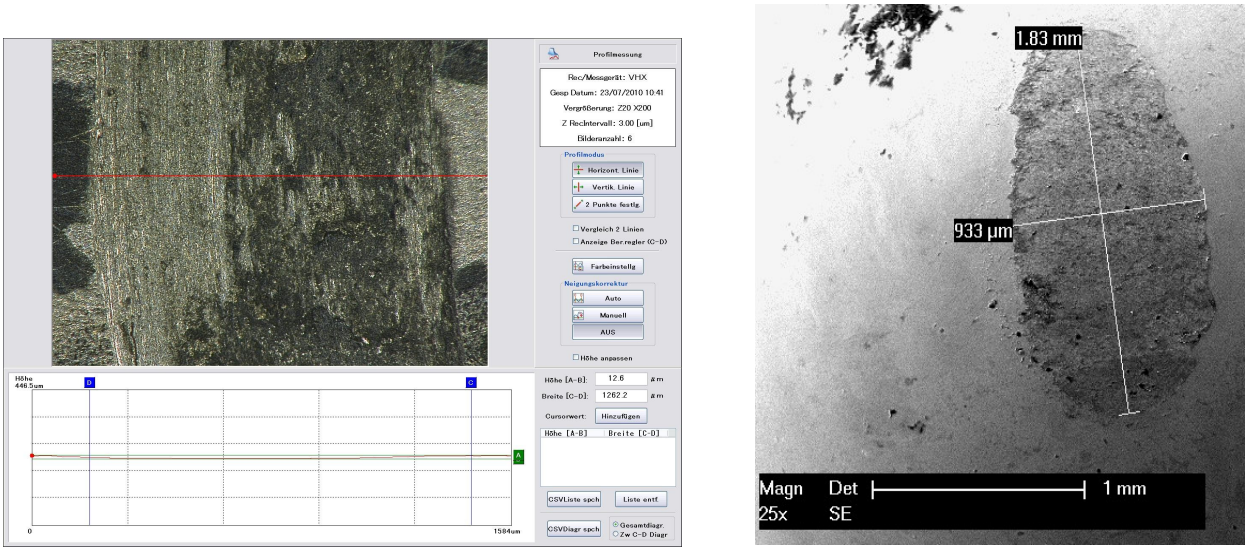

Figure 4.56 *Wear track and ball wear by sample TiWC2.5*

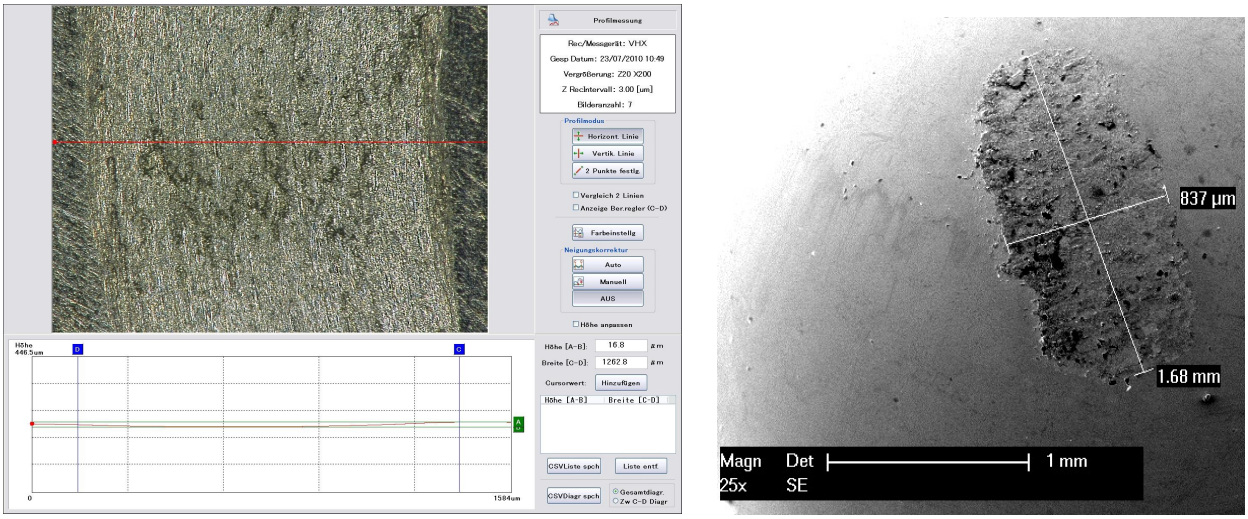

Figure 4.57 *Wear track and ball wear by sample TiWC2.6*

A summary of the wear track measurements of the tested samples, as well as the ball wear and calculated wear rates are presented in table 4.11.

Table 4.11 *Wear measurements of the TiWC samples*

Sample	h [µm]	s [µm]	A [µm²]	Ball wear diagonals [µm]	Wear rate [10^{-5} mm³/Nm]
Ti	148,8	1879,5	187141	-	126,8
TiWC2.3	15,4	1112	14764	1140 x 1680	6,7
TiWC2.4	9,38	1705	13722	1230 x 1960	6,84
TiWC2.5	12,6	1262,2	18417	1830 x 933	9,32
TiWC2.6	16,8	1262,8	19580	1680 x 837	9,9

The improved wear resistance of the TiWC samples illustrated in figure 4.58 is conferred by the formation of the cubic chromium-titanium ($CrTi_4$), cobalt-titanium ($CoTi_2$), titanium-tungsten (TiW) and particularly titanium carbide (TiC) phases in the alloyed zones. The samples exhibit little differences in wear behavior one from each other. Sample TiWC2.3, which has the highest hardness and titanium carbide content exhibits slightly better wear behavior and samples TiWC2.5 and TiWC2.6, characterized by higher cobalt-titanium content present slightly higher wear rates.

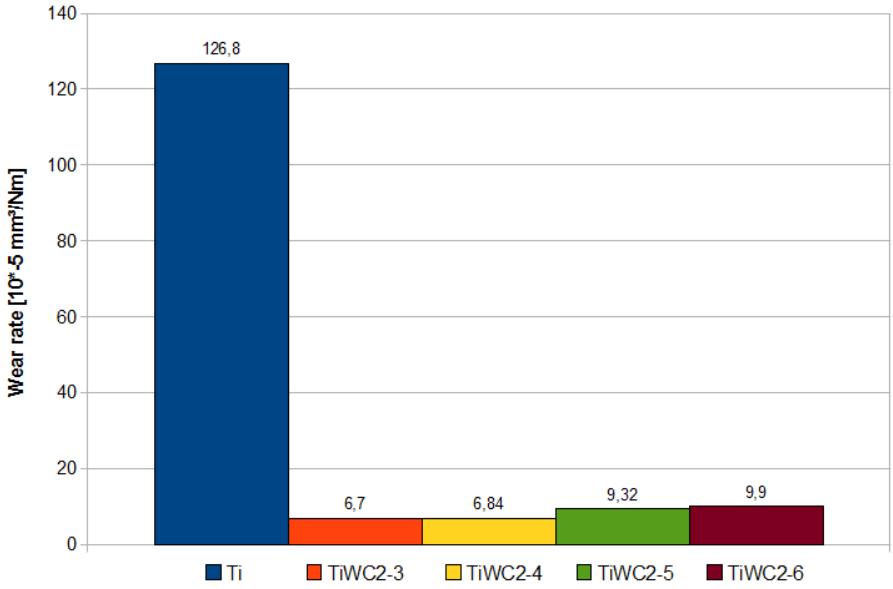

Figure 4.58 *Wear rate histogram of the TiWC samples*

4.3.2.3 Corrosion behavior of the alloyed TiWC samples

The polarization curves of the TiWC samples resulted from the electrochemical corrosion test are displayed in figure 4.59, and the recorded values for the current density at the corrosion potential of the tested samples are presented in table 4.12.

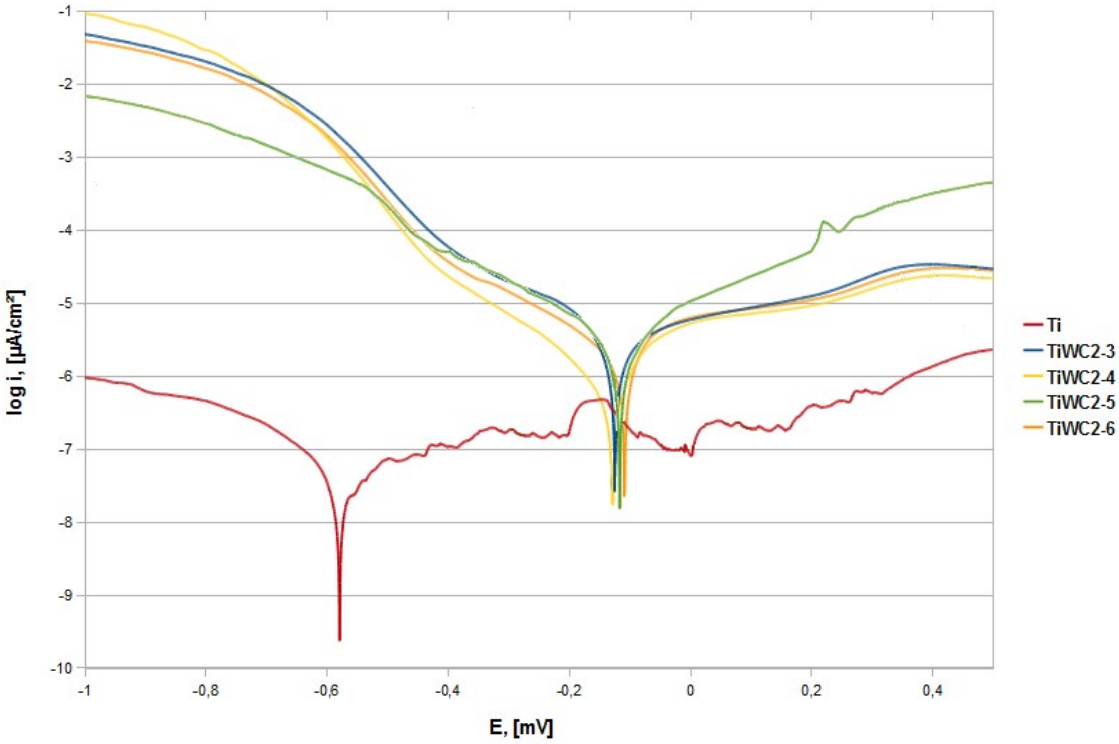

Figure 4.59 *Polarization curves of the TiWC samples*

The results reveal a shift of the corrosion potential from -576 mV to about -120 mV and an increase of the corrosion density to values of 0,99 μA/cm² for the alloyed surfaces. Although the alloyed samples show close corrosion density values one to another, the lower corrosion rates of samples TiWC2.5 and TiWC2.6 could be attributed to the higher amounts of cobalt-titanium in the alloyed zone.

Table 4.12 *Corrosion values of the tested TiWC samples*

	Ti	TiWC2.3	TiWC2.4	TiWC2.5	TiWC2.6
E_{corr} [mV]	-576,3	-122,1	-125,7	-116,4	-106,0
i_{corr} [μA/cm²]	0,0061	0,9929	0,9763	0,5286	0,4875

4.4 Residual stresses in the alloyed samples

Residual stress of the sample was determined with the hole-drilling method. The investigations were conducted to depths of 0,5 – 1,0 mm, depending on the depth of the alloyed area. The residual stresses were calculated with the integral method, based on the measured strains.

4.4.1 Residual stresses in the TiBN samples

The residual stress measurements on the TiBN samples are illustrated in figures 4.60 to 4.63.

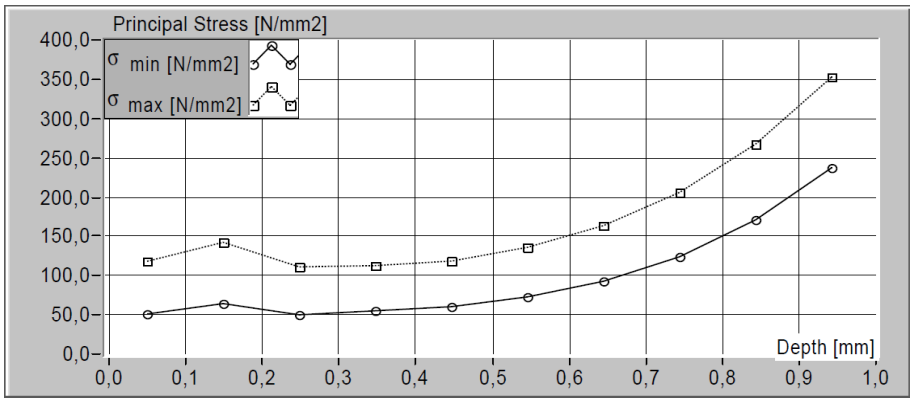

Figure 4.60 *Stress distribution in sample TiBN1.3*

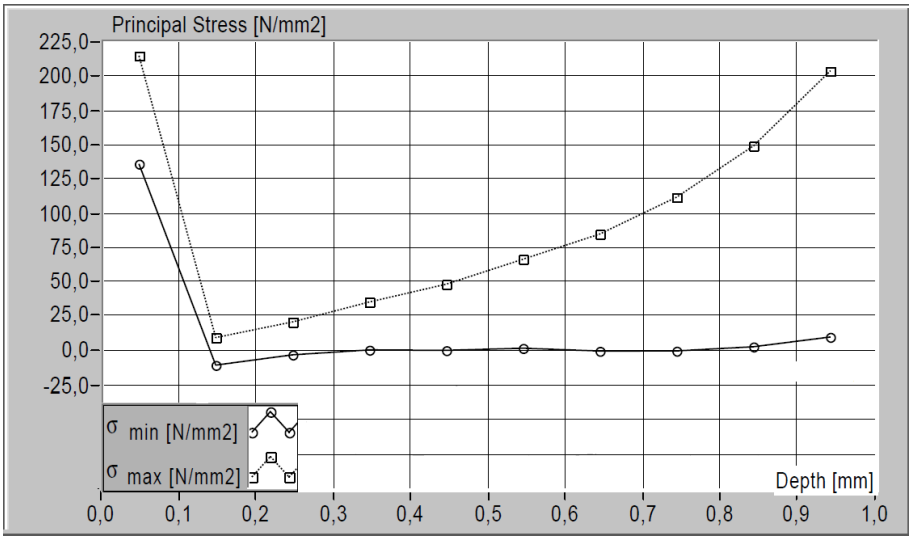

Figure 4.61 *Stress distribution in sample TiBN1.4*

Measurements show that sample TiBN1.3 (fig. 4.60) possesses tensile stresses of maximum 150 N/mm² in the alloyed zone, which increase towards the base material. Sample TiBN1.4 exhibits both tensile and compressive stresses. The maximum tensile residual stress reaches values up to approximately 240 N/mm², whereas the compressive stress has low values of about –20 N/mm².

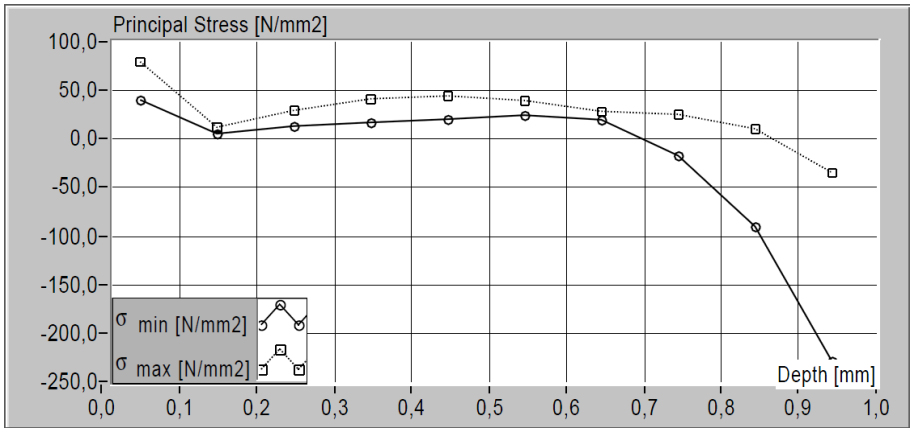

Figure 4.62 *Stress distribution in sample TiBN2.2*

Sample TiBN2.2 shows approximately constant tensile stress of 50 N/mm² for the entire depth of the alloyed zone. The measurements conducted on sample TiBN2.4 show tensile stresses with values up to 350 N/mm², which decrease as the hole depth increases. The tensile residual stresses that occurred in the TiBN samples usually in the first 0,2 mm of the surface is balanced by compressive stresses in the deeper layers. The balanced compressive stresses in the base material.

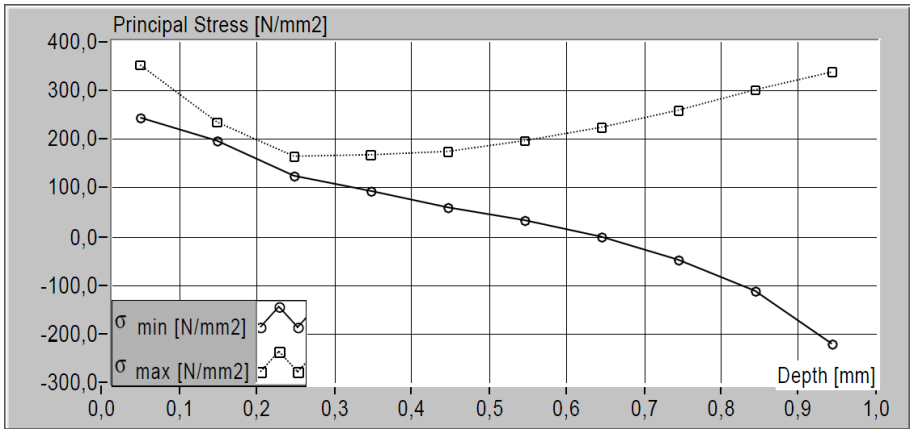

Figure 4.63 *Strain distribution in sample TiBN2.4*

4.4.2 Residual stresses in the TiWC samples

The results of the hole-drilling method for the investigation of the stress distribution in the TiWC samples are presented in figures 4.64 to 4.67.

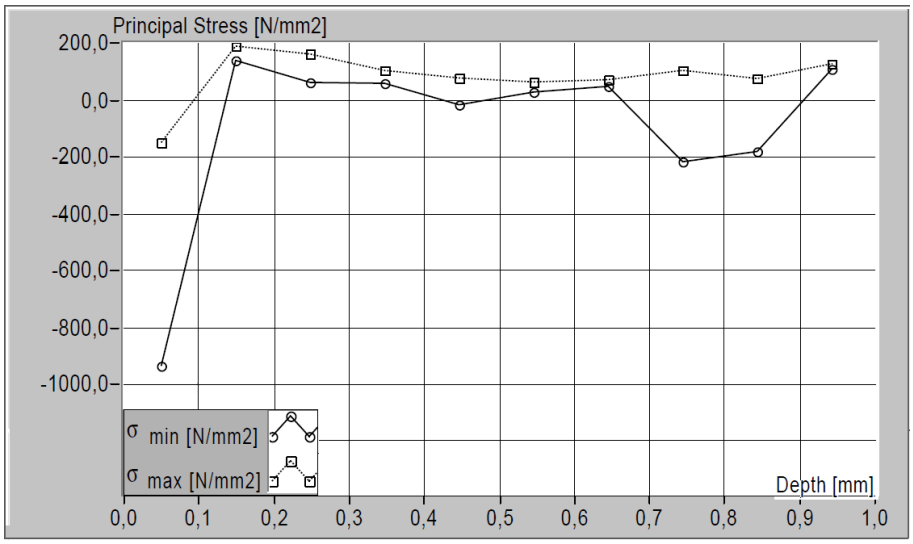

Figure 4.64 *Strain distribution in sample TiWC2.3*

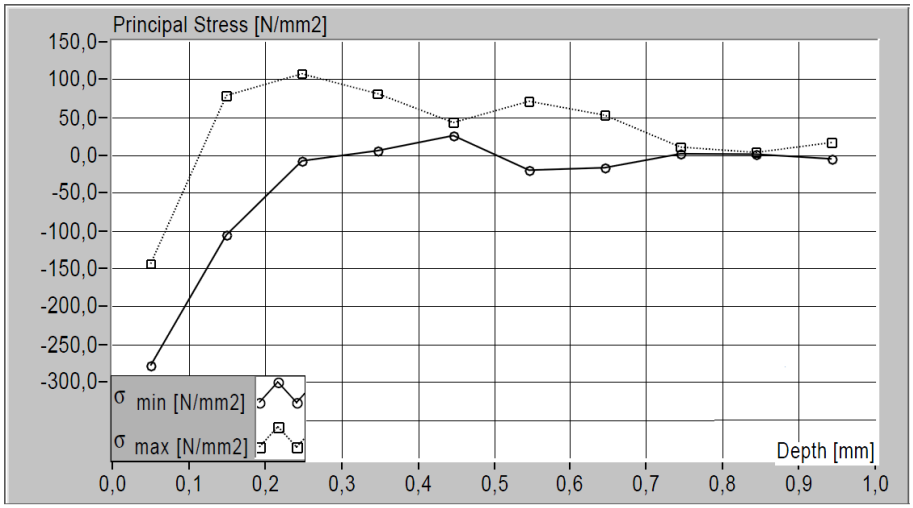

Figure 4.65 *Strain distribution in sample TiWC2.4*

The stress measurement revealed high compressive stresses of about 950 N/mm² in sample TiWC2.3. The stresses occur mainly in the first 0,2 mm depth of the alloyed zone where the compressive residual stresses change their sign.

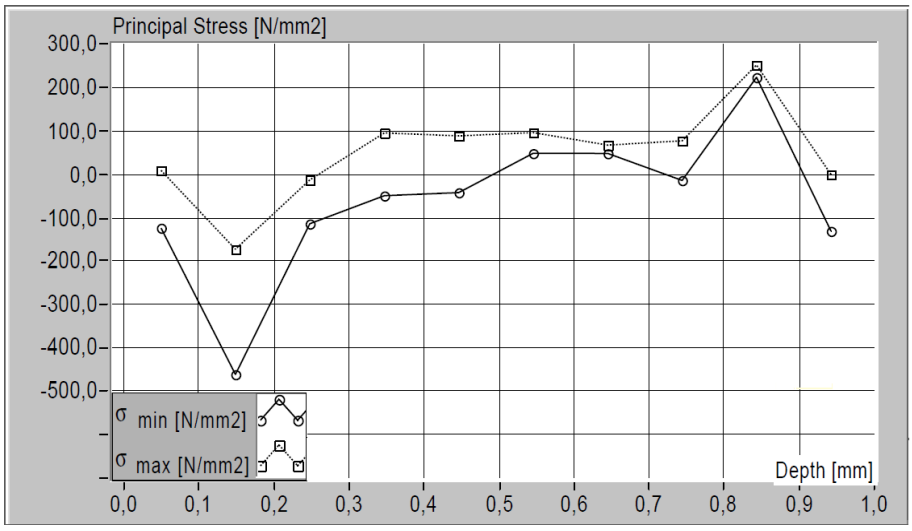

Figure 4.66 *Strain distribution in sample TiWC2.5*

The magnitude of the compressive residual stresses of samples TiWC2.4 and TiWC2.5 reaches moderate values of approximately 300 N/mm², respectively 500 N/mm² until almost 0,3 mm from the surface. Sample TiWC2.6 exhibits tensile residual stresses of low values, which increase at the interface towards the base material.

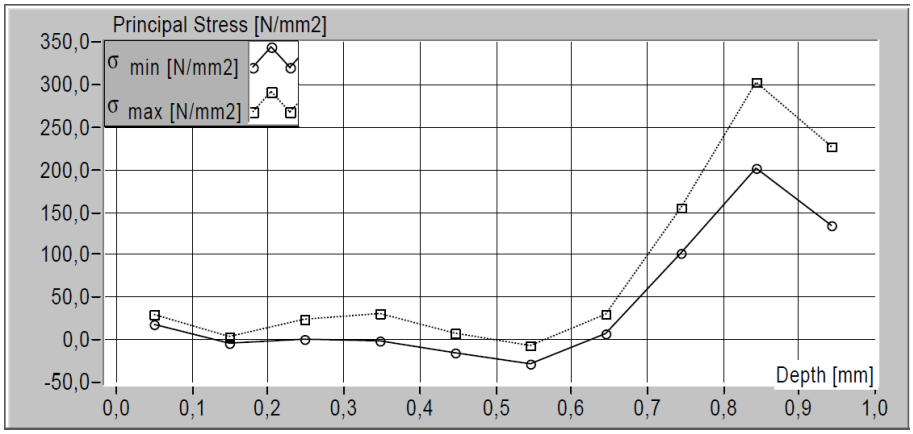

Figure 4.67 *Strain distribution in sample TiWC2.6*

Since material failures initiate at the surface in most cases, the mainly compressive residual stresses recorded in the TiWC samples tend to close up surface cracks, which would greatly improve the mechanical behavior and increase the fatigue life of the material.

4.5 Conclusions

This work was concerned with the electron beam surface engineering techniques. Also, the circumstances of the electron beam alloying process were detailed. Particularly, the structural modifications that occur in the titanium – boron nitride and titanium – tungsten carbide system, the tribological and corrosion behavior as well as the residual stresses of the alloyed near surface regions were investigated.

The analysis of the electron beam remelting parameters of the boron nitride aluminium silicon coating revealed that the alloying depth of the samples increases with the increase of current intensity and the decrease of process speed. The X-ray diffraction patterns coupled with the EDX analysis showed that surface alloying of titanium with boron nitride powder in aluminium silicon matrix leads to the formation of titanium silicon borides (Ti_6Si_2B), titanium aluminum nitrides (Ti_2AlN) as well as orthorhombic and cubic titanium borides (TiB). The formation of the above mentioned phases increases surface hardness and greatly improves the wear behavior.

The electron beam alloying process of the titanium substrate with tungsten carbide cobalt chromium powder was performed applying two energy distribution geometries of the electron beam. The result of the alloying process consists in the development of hard titanium carbide (TiC) distributed in the chromium-titanium ($CrTi_4$), cobalt-titanium ($CoTi_2$) and titanium-tungsten (TiW) phases. The presence of titanium carbide (TiC) in the alloyed zone implies a high increase of surface hardness and wear resistance of the base material and a significant reduction of the friction coefficient.

Electrochemical corrosion tests showed that electron beam surface alloying of titanium with boron nitride, respectively with tungsten carbide powder promotes an impairment of titanium's corrosion behavior, the alloyed surfaces exhibiting higher corrosion rates. Also, the determination of residual stresses in the alloyed samples revealed that in the TiBN samples mostly tensile residual stresses occur, whereas in the TiWC samples the compression residual stresses are predominant.

Chapter 5
General conclusions, original contributions and future work

5.1 Conclusions

The experiments performed on the electron beam surface alloyed commercially pure titanium with boron nitride and tungsten carbide powder lead to the following conclusions:

- surface alloying of titanium with boron nitride powder was achieved at energy ranges between 180 and 360 Ws/mm;
- the structure consists of titanium-silicon boride (Ti_6Si_2B), titanium-aluminium nitride (Ti_2AlN), orthorhombic and cubic titanium borides (TiB) uniformly distributed in the alloyed surface;
- the formation of the nitride and boride phases has led to an increase of the hardness to a maximum of 883 HV 0.3, a slight reduction of the friction coefficient from 0,68 of pure titanium to as low as 0,46 and a significant improvement of the wear behavior;
- surface alloying of titanium with tungsten carbide powder was possible in a narrow energy range from 300 Ws/mm to 330 Ws/mm;
- the structure of the alloyed zone is formed of titanium carbide (TiC) uniformly distributed in the chromium-titanium ($CrTi_4$), cobalt-titanium ($CoTi_2$) and titanium-tungsten (TiW) phases;
- the newly formed structure possesses enhanced hardness values of up to 748 HV 0.3 and superior wear resistance, attributed to the hard titanium carbide

precipitates. Also, the formation of cobalt-titanium has led to the decrease of the friction coefficient to values of 0,365;

- the alloying process led to an increase of the corrosion rates for both TiBN and TiWC samples; the current densities recorded for the TiBN samples reach values of up to 1,92 μA/cm², and up to 0,99 μA/cm² for the TiWC samples;
- the hole-drilling method revealed that the TiBN samples exhibit tensile residual stresses in the first 0,2 – 0,3 mm from the surface, balanced by compression stresses in the deeper layers, whereas the TiWC samples posses mainly compression residual stresses, which may improve the fatigue behavior of the material;
- the conducted experiments and investigations reveal that the titanium surfaces alloyed with tungsten carbide in cobalt – chromium matrix using a line scan geometry of the electron beam, perform better in wear testing as the other TiWC and TiBN alloyed samples, representing the more proper solution in wear applications.

5.2 Original contributions

The purpose of this work was to increase the surface hardness and sliding wear resistance of commercially pure titanium through electron beam alloying, without substantially affecting its well-known corrosion behavior.

Accordingly, two surface alloying directions were established: with a hexagonal boron nitride powder in aluminium – silicon matrix on one hand and with a tungsten carbide powder in cobalt – chromium matrix on the other hand. Boron nitride was chosen because reactions between titanium and boron nitride arouse a great interest due to the high affinity of titanium for both boron and nitrogen, and the stability of resulting borides and/or nitrides; and tungsten carbide promotes the precipitation of hard titanium carbide phases.

The alloying process was conducted through the remelting of the pre-deposited coatings. The boron nitride aluminium-silicon powder was deposited with the atmospheric plasma spraying (APS) technique, and the tungsten carbide cobalt-

chromium powder using high velocity oxygen fuel (HVOF) spraying.

The aim of the experimental program was to investigate the resulting structural modifications in the base material – coating system after the remelting process and the study of the formed structures. These were studied with various methods of investigation such as X-ray diffraction, Scanning Electron Microscopy(SEM), Energy Dispersive Spectroscopy (EDX). Hardness measurements, pin-on-disc wear tests, hole-drilling measurements of the residual stresses and electrochemical corrosion tests were used to determine the properties of the alloyed samples.

5.2 Future work

The theoretical and experimental studies conducted in the present thesis emphase the current trends in surface engineering of titanium alloys, as well as the vastness of this domain.

In this regard, some further research directions can be outlined:

- attempts to develop mathematical models for the prediction of the microstructure of the alloyed surfaces;
- heat treatments of the alloyed surfaces and the examination of the stress relaxation;
- surface alloying with other economically attractive powder materials, like graphite.

References

[1] H.J. Spies, *"Randschichtbehandlung von Aluminium- und Titanlegierungen – ein Überblick"*, HTM – Journal of heat treatment and materials, 2010

[2] A.P. Sanders, *"Surface hardening of titanium articles with titanium boron layers and its effects on substrate shape and surface texture"*, Journal of manufacturing science and engineering, 2009

[3] T. Rostlund, B. Albrektsson, T. Albrektsson, H. McKellop, *"Wear of Ion- Implanted pure Titanium against UHMWPE"*, Biomaterials, 1989

[4] A.M. Maurer, S.A. Brown, J.H. Payer, K. Merritt, J.S. Kawalee, *"Reduction of fretting corrosion of Ti-6Al-4V by various Surface treatments"*, Journal of Orthopedic Research, 1993

[5] C. Met, L. Vandenbulcke, M.C. Sainte Catherine, *"Friction and wear characteristics of various prosthetic materials sliding against Diamond – coated Titanium alloy"*, Wear, 2003

[6] B.J. Kooi, Y.T. Pei, J.T.M de Hosson, *"The evolution of microstructure in a Laser clad TiB-Ti composite coating"*, Acta Materialia, 2003

[7] M.Pappas, G. Makris, F. Baechel, *"Titanium nitride ceramic films against Polyethylene: A 48 Million cycle wear test"*, Clin Orthop Relat Res, 1995

[8] W. Herr, E. Broszeit, *"Effect of an annealing process on the tribological properties of sputtered hard coatings"*, Surface and coatings Technology, 1997

[9] S. Bahadur, Chien-Nan Yang, *„Friction and wear behavior of tungsten and titanium carbide coatings"*, Wear, 1996

[10] G. Hunter, V. Pawar, A. Saleht, M. Long, *"Abrasive wear of modified CoCr and Ti-6Al-4V surfaces against bone cement"*, Materials and Processes for Medical devices, 2003

[11] H. Hamatani, Y. Miyazaki, *"Optimization of an electron beam remelting of HVOF sprayed alloys and carbides"*, Surface and Coatings Technology, 2002

[12] J.K. Wessel, *"Handbook of Advanced Materials"*, Wiley Interscience, 2004

[13] G.S. Brady, H.R. Clauser, J.A. Vaccari, *"Materials Handbook, Fifteenth Edition"*, McGraw-Hill Handbooks, 2002

[14] F.H. Froes, *"Light Metal age"*, 58, 2000

[15] I.J. Polmear, *"Light Alloys, Metallurgy of the Light Metals"*, 3rd Ed. Edward Arnold, 1996

[16] E.K. Molchanova, *"Phase Diagrams of Titanium Alloys"*, Israel Program for Scientific Translations, 1995

[17] F.H. Froes, D. Eylon, H.B. Bomberger, *"Titanium Technology: Present Status and Future Trends"*, International Titanium Association, 1985

[18] M. Peters, J. Kumpfert, C.H. Ward, C. Leyens, *"Titanium Alloys for Aerospace Applications"*, Advanced Engineering Materials, Wiley-VCH, 2003

[19] M. Peters, J. Hemptenmacher, J. Kumpfert, C. Leyens, *„Structure and Properties of Titanium and Titanium Alloys"*, Wiley-VCH, 2003

[20] C. Leyens, *"Oxidation and Protection of Titanium and Titanium Aluminides"*, Wiley-VCH, 2003

[21] J.S. Grauman, B. willey, *"Shedding New Light on Titanium in CPI Construction"*, Chemical Engineering, 1998

[22] P.H. Morton, *"Designing with Titanium"*, Inst. Metals, 1986

[23] H. Fujii, Y. Yamashita, K. Takahashi, *"Application of Titanium and its Alloys for Automobile parts*", Nippon Steel Technical Report, 2003

[24] S. Eisenberg, *"Titanwerkstoffe im Automobil"*, EUROFORUM, 1998

[25] K. Faller, *"The use of titanium in family automobiles: Current trends"*, Journal of Material Science, 2001

[26] O. Schauerte, S. Eisenberg, M. Kramer, K. Faller, *"Einsatzpotentiale für Titan im Serienfahrzeug"*, VDI/VW Gemeinschaftstagung Technologien um das 31-Auto, 1999

[27] K. Miyoshi, D.H. Buckley, *"Correlation of Tensile and Shear Strengths of Metals with Their Friction Properties"*, ASLE Trans., Vol 27, 1982

[28] K.E. Budinski, *"Tribological Properties of Titanium Alloys"*, Wear, Vol 151, 1991

[29] D.H. Buckley, *"Surface Effects in Adhesion, Friction, Wear, and Lubrication"*, Elsevier Scientific, 1981

[30] K. Holmberg, A. Matthews, *"Coatings Tribology. Properties, Techniques and Application in Surface Engineering"*, Elsevier, 1994

[31] P.J. Blau, *"Friction and wear transitions of materials – Break-in, Run-in, Wear-in"*, Noyes Publications, 1989

[32] F.P. Bowden and D. Tabor, "*Friction. An Introduction to Tribology",* Robert Krieger Publishing, 1982

[33] N.P. Suh, H.C. Sin, *"The genesis of friction"*, *Wear*, 1981

[34] D.H. Buckley, *"Importance and Definition of Materials in Tribology: Status of Understanding"*, *Tribology in the 80's,* Vol 1, NASA Conf. Publ. 2300, National Aeronautics and Space Administration, 1983

[35] D.H. Buckley, "*Surface Effects in Adhesion, Friction, Wear and Lubrication",* Elsevier, 1981

[36] S.E Franklin, *"The friction and wear characteristics of several wear-resistant surface coatings"*, Phillips CFT Technology, 1991

[37] P.J. Alison, H. Wilman, *"The Different Behavior of Hexagonal and Cubic Materials in their*

Friction", Wear and Work Hardening During Abrasion, *Brit. J. Appl. Phys.,* Vol 15, 1964

[38] R.P. Steijn, *"Friction and Wear of Single Crystals"*, *Wear,* Vol 7, 1964

[39] T.E. Fischer, M.P. Anderson, S. Jahanmir, *"Influence of Fracture Toughness on the Wear Resistance of Yttria-doped Zirconium Oxide"*, *J. Am. Ceram. Soc.,* Vol 72, 1989

[40] H. Czichos, K. Habig, *"Tribology Handbook – Friction and Wear"*, Vieweg, 1992

[41] W.A. Glaeser, *"Characterization of Tribological Materials. Materials Characterization Series."* Butterworth-Heinemann, 1993

[42] G.W. Stachowiak, A.W. Batchelor, *"Engineering Tribology*", Elsevier Butterworth-Heinemann, 2005

[43] J.A. Williams, *"Wear and wear particles - Some fundamentals."* Tribology International 38(10), 2005

[44] M.H Jones, D. Scott, *"Industrial Tribology: the practical aspects of friction, lubrication, and wear"*, Elsevier Scientific Publishing Company, 1983

[45] U. Lotz, J. Postlethwaite, *„Erosion-Corrosion in Disturbed Two Phase Liquid/ Particle Flow"*, *Corros. Sci.,* Vol 30 (No. 1), 1990

[46] T.F.J. Quinn, *"Review of oxidational wear. Part I: The origins of oxidational wear"*, Tribology Int., 1983

[47] T.F.J. Quinn, W.O. Winer, *"The thermal aspects of oxidational wear"*, Wear, 1985

[48] F.M. Kustas and M.S. Misra, *"Friction and Wear of Titanium Alloys"*, Martin Marietta Astronautics Group, 1992

[49] P. Sioshansi, *"Improving the Properties of Titanium Alloys by Ion Implantation"*, *J. Metals,* 1990

[50] W.C. Oliver, R. Hutchings, J.B. Pethica, E.L. Paradis, and A.J. Shuskus, *"Ion Implanted Ti-6Al-4V*", *Mater. Res. Soc. Symp. Proc.,*, 1984

[51] A. Bloyce, *"Surface engineering of titanium for wear protection"*, Proceedings of the Institution of Mechanical Engineers/ Jurnal of engineering tribology, 1998

[52] F. Preissner, P. Minarski, "*Results on nitriding titanium and Ti-6Al-4V with a new thermochemical treatment under high gas pressure"*, Science and Technology, 1993

[53] Wolfson Institute for Surface Engineering, University of Birmingham, *"Surface Engineering of Titanium Components"*, Final Report, BRITE/EURAM Contract RI. 1B.0151C(H), 1991

[54] R.M. Streicher, H. Weber, R. Schon, and M. Semlitsch, *„New Surface Modification for Ti-6Al-7Nb Alloy: Oxygen Diffusion Hardening (ODH)"*, *Biomaterials*, 1991

[55] M. Thoma, *"Plating on Titanium"*, Plating and Surface Finishing*,* 1983

[56] C.G. John, *"Electroplated Coating of Titanium for Engineering Applications",* Proceedings International Conference Designing with Titanium*,* Institute of Metals, 1986

[57] W.A. Baeslack III, S. Krishnamurthy, F.H. Froes, *„Solidification Characteristics of Laser Surface Melts in Advanced Titanium Alloys“*, Rapid Solidification Technology, 1986

[58] P.H. Morton, T. Bell, A. Weisheit, B.L. Mordike, K. Sagoo, „*Laser Gas Nitriding of Titanium and Titanium Alloys“*, Surface Modification Technologies V, Proceedings of the 5th International Conference, 1992

[59] M. Vilnat, *„Traitment de Durface: Le Laser S' Affirme“*, Technologies, 1993,

[60] Marcel Schneider, “*LASER CLADDING WITH POWDER, effect of some machining parameters on clad properties“*, PhD Thesis, 1998

[61] K.E. Schneider, *“Thermal spraying for power generation components”*, WILEY-VCH, 2006

[62] B, Wielage,*” Protection of titanium alloys surfaces by thermal spraying*”, Proceedings of the International Thermal Spray Conference, 2005

[63] J. Wilden, *“Thermal spraying, simulation of coating structure”*, Proceedings of the International Thermal Spray Conference, 2005

[64] R.B Heimann, *“Plasma Spraying Coatings”,* Wiley-VCH, 1996

[65] D.S. Arensburger, S.Y. Zymakov, P.A. Kulu, *“Coatings deposited by the High Velocity Flame Spraying Method”*, Powder Metallurgy and Metal Ceramics

[66] E. Lifshin, *“X-ray characterisation of metals”*, Wiley-VCH, 1999

[67] B.D. Cullity, S.R. Stock, *“Elements of X-ray diffraction”*, Prentice Hall, 2001

[68] N. Stribeck, *“X-ray scattering of soft matter”*, Springer, 2007

[69] J.I. Goldstein, *“Scanning electron microscopy and X-ray microanalysis”*, Kluwer Academic/ Plenum Publ., 2003

[70] S.L. Flegler, J.W. Heckman, K.L. Klomparens, *“Elektronenmikroskopie: Grundlagen, Methoden, Anwendungen”*, Spektrum/ Akademische Verlag, 1995

[71] L. Reimer, *“Scanning electron microscopy: physics of image formation and microanalysis”*, Springer, 1998

[72] H. Günzler, H.U. Gremlich, *“IR spectroscopy”*, Wiley-VCH, 2002

[73] M. Sauer, *“Handbook of fluorescence spectroscopy and imaging from ensemble to single molecules”*, Wiley-VCH, 2009

[74] ASTM G99-05(2010) Standard Test Method for Wear Testing with a Pin-on-Disk Apparatus

[75] ASTM E 837-01. Standard Test Method for Determining Residual Stresses by the Hole-Drilling Strain-Gage Method.

[76] E. Protopopoff, P. Marcus, *„Potential Measurements with Reference Electrodes“*, Corrosion: Fundamentals, Testing, and Protection, ASM Handbook, 2003

[77] F. Mansfeld, *“The Polarization Resistance Technique for Measuring Corrosion Currents”*, ASM Handbook vol.13, 2003

[78] N.G. Thompson and J.H. Payer, "*Corrosion Testing Made Easy-dc Electrochemical Methods",* ASM Handbook vol. 13, 2003

[79] S. Schiller; S. Panzer, *"Thermal surface modification by HF-deflected electron beams"*, Proceedings of the Conference on the Laser VS the Electron Beam in Welding, Cutting and Surface Treatment: State of the Art, 1985

[80] R. Zenker, *„Electron beam surface treatment: industrial application and prospects"*, Surface Engineering, 1996

[81] R. Zenker, E Wagner, B. Furchheim, *„Electron beam – a modern energy source for surface treatment*", 6th International Seminar of IFHT: Advanced Heat Treatment Techniques Towards the 21st Century, 1997

[82] R. Zenker, *„Electron beam surface treatment and multipool welding – state of the art"*, International Conference on High-Power Electron Beam Technology", 2002

[83] R. Zenker, N. Frenkler, T. Ptaszek, *„Electron beam surface treatment of Al, Mg, and Ti alloys"*, Proceedings of the 7th International Seminar of IFHT: Heat treatment and surface engineering of light alloys, 1999

[84] R. Zenker, P. Krug, A. Buchwalder, T. Dickmann, N. Frenkler, S. Thiemer, *„Elektronenstrahlschweißen und –profilieren von sprühkompaktierten Zylinderlaufbuchsen aus Al-Si-Werkstoffen"*, Zylinderlaufbahn, Kolben, Pleuel – Innovative Systeme im Vergleich, Tagung Böblingen, VDI-Berichte 2006

[85] A. Buchwalder, *„Beitrag zur Flüssigphasen-Randschichtbehandlung von Bauteilen aus Aluminiumwerkstoffen mittels Elektronenstrahl"*, Dissertation TU Bergakademie Freiberg, 2007

[86] R. Zenker, G. Sacher, A. Buchwalder, J. Liebich, A. Reiter, R. Häßler, *„Hybrid Technology Hard Coating – Electron Beam Surface Hardening"*, Surface and Coatings Technology, 2007

[87] S. Schiller; S. Panzer, *„Härten von Oberflächenbahnen mit Elektronenstrahlen"*, HTM 2(1987)

[88] R. Zenker, A. Buchwalder, H.J. Spies, „*New electron beam technologies for surface treatment*", Proceedings of the 7th International Conference on Electron Beam Technologies, 2003

[89] G. Mattausch, H. Morgner, J. Daenhardt, et al., *„Survey of electron beam technologies at FEP"*, Proceedings / EBEAM 2002: International Conference on High-Power Electron Beam Technology", 2002

[90] R. Zenker, *„Elektronenstrahl-Randschichtbehandlung, Innovative Technologie für höchste industrielle Ansprüche"*, Monographie, pro-beam AG & Co, 2003

[91] R. Zenker, A. Buchwalder, N. Frenkler, S. Thiemer, *„Moderne Elektronenstrahltechnologien zum Fügen und zur Randschichtbehandlung"*, Vakuum in der Praxis, 2005

[92] R. Zenker, H.J. Spies, *„15 Jahre industrielle Anwendung der Elektronenstrahl Randschicht-behandlung“*, Härtereikolloquium Wiesbaden, 2001

[93] T. Loewer, *„Analysis, visualisation and accurate description of an electron beam for high repeatability of industrial production processes“*, „Proceedings of the 7th International Conference on Electron Beam Technologies“, 2003

[94] R. Zenker, *„Elektronenstrahlbearbeitung für Powertrainkomponenten“*, Kooperationsforum Metalle im Automobilbau, Innovationsforum in Be- und Verarbeitung, 2005

[95] H.J. Spies, R. Zenker, K. Bernhard, *„Duplex- Randschichtbehandlung von metallischen Werkstoffen mit Elektronenstrahltechnologien“*, Härtereitechnik, 1998

[96] O. Kessler, *„Combination of coating and heat treatment processes“, Surface and Coatings Technology*, 2006

[97] H.J. Spies, S. Friedrich, A. Buchwalder, *„Elektronenstrahlbehandlung von PVD-Hartstoffschichten“*, Mat.wiss und Werkstofftechnik, 2003

[98] R. Zenker, A. Buchwalder, N. Frenkler, S. Thiemer, *„Electron beam surface shaping/profiling“*, 8th Int. Conf. on EB Technologies, 2006

[99] R. ZENKER, *„Structure and properties of electron beam surface treatment“*, Advanced Engineering Materials, 2004

[100] R. Zenker, *„Modern thermal electron beam processes – research results and industrial application“*, European Conference „Innovation in heat treatment for industrial competitiveness”, 2008

[101] F. Vollertsen, K. Partes, J. Meijer, *„State of the art of Laser Hardening and Cladding“*, Proceedings of the Third International WLT-Conference on Lasers in Manufacturing, 2005

[102] D. Uțu, G. Marginean, **C. Pogan**; W. Brandl, V.A. Șerban „*Improvement of the wear resistance of titanium alloyed with boron nitride by electron beam irradiation*”, Surface and Coatings Technology 201 (2007) 6387-6391; ISSN: 0257-8972

[103] **C. Pogan**, G. Marginean, V.A. Șerban, W. Brandl “*Surface alloying of titanium by electron beam irradiation*” Xth Edition Academic Days International Symposium Engineering Materials New Horizons and Processing Techniques, Tom 52(66), Fasc.2, 2007

[104] **C. Pogan**, I. Secosan, I. Mitelea, W. Brandl, *„The influence of electron beam scanning modus on the properties of titanium surfaces alloyed with tungsten carbide powder”*, to be presented at ModTech 2011, Moldova

[105] M.K Khraisheh, B.M. Darras, P. Kalu, M. Adams-Hughes, N. Chandra, *„Correlation Between the Microstructure and Forces Generated During Friction Stir Processing of AA5052”*, Materials Science Forum Vols. 475-479, 2005

[106] I. Mitelea, D. Uțu, **C. Pogan** “*Geometrical aspects of titanium base composites deposited*

by plasma transferred arc welding", Scientific Bulletin of the "Politehnica" University of Timișoara, Tom 52 (66), Fasc.1, 2007; ISSN 1224-6077

[107] I. Mitelea, D. Uțu, **C. Pogan**, "*Dilution phenomenon during coating of titanium alloys by Plasma Transferred Arc (P.T.A) process*", 1st EUCOMAS Conference Berlin, May 2008, ISSN 0083-5560, ISBN 978-3-18-092028-3

[108] I. Mitelea, D. Uțu, **C. Pogan,** *"Characteristics of Plasma Transferred Arc (P.T.A.) deposition on titanium alloys",* Scientific Bulletin of the "Politehnica" University of Timișoara, Tom 53 (66), Fasc. 3, 2008, ISSN 1224-6077

[109] I. Mitelea, D. Uțu, **C. Pogan,** *"The effect of process parameters on the hardness of WC coatings deposited by Plasma Transferred Arc (P.T.A) welding"*, Scientific Bulletin of the "Politehnica" University of Timișoara, Tom 53 (67), Fasc. 4, 2008, ISSN 1224-6077

[110] **C. Pogan**, I. Secosan, I. Mitelea, W. Brandl, *„Surface alloying of titanium with tungsten carbide powder using electron beam irradiation"*, forwarded for publishing

Internet references

[111] *[http://people.bath.ac.uk]*

[112] *[http://forums.pelicanparts.com]*

[113] *[http://www.psi-pci.com]*

[114] *[http://www.dynamettechnology.com]*

[115] *[www.kermetico.com]*

[116] *[www.surfacetechno.com]*

[117] *[http://serc.carleton.edu]*

[118] *[www.quality-analysis.de]*

[119] *[http://www.csm-instruments.com]*

[120] *[http://www.werner-stehr-tribologie.com*

[121] *http://sites.google.com/site/temfemguy]*

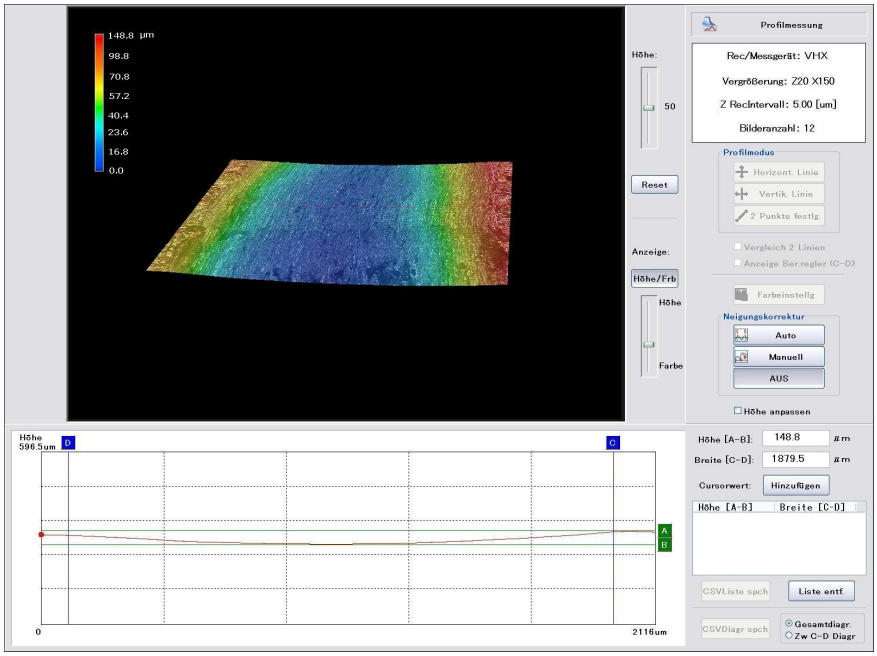

Figure A.1 *Wear track profile on the titanium sample*

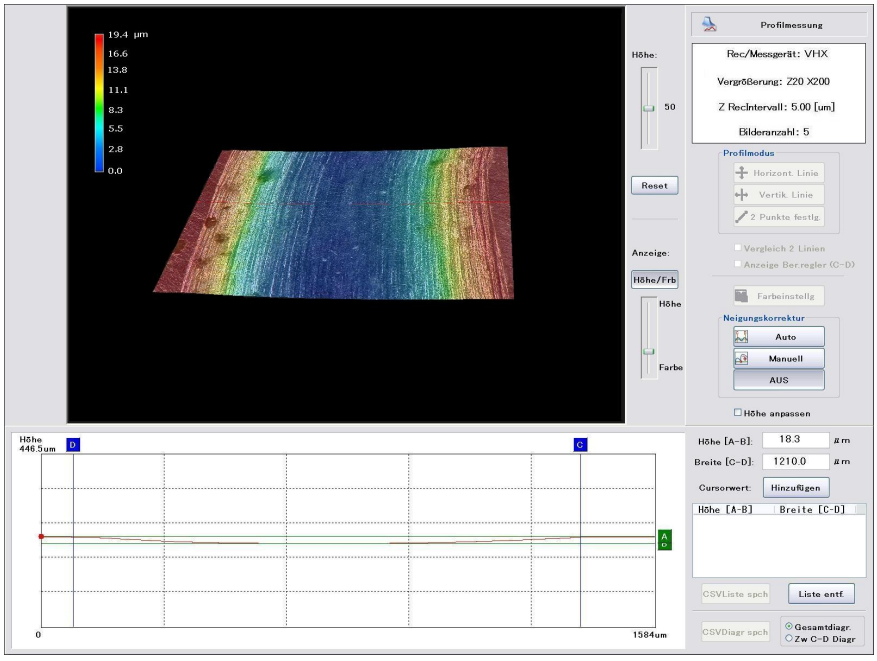

Figure A.2 *Wear track profile on sample TiBN1.3*

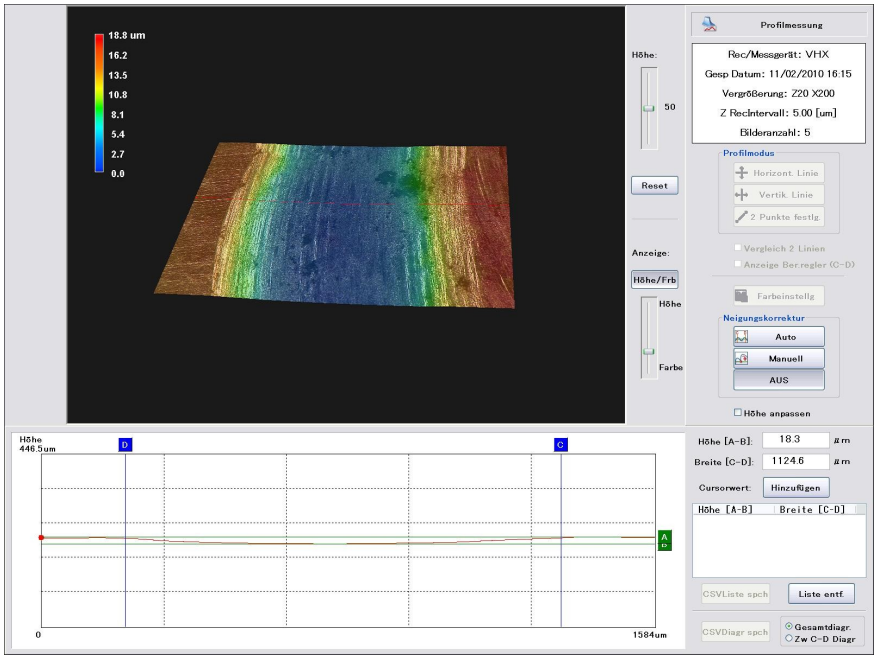

Figure A.3 *Wear track profile on sample TiBN1.4*

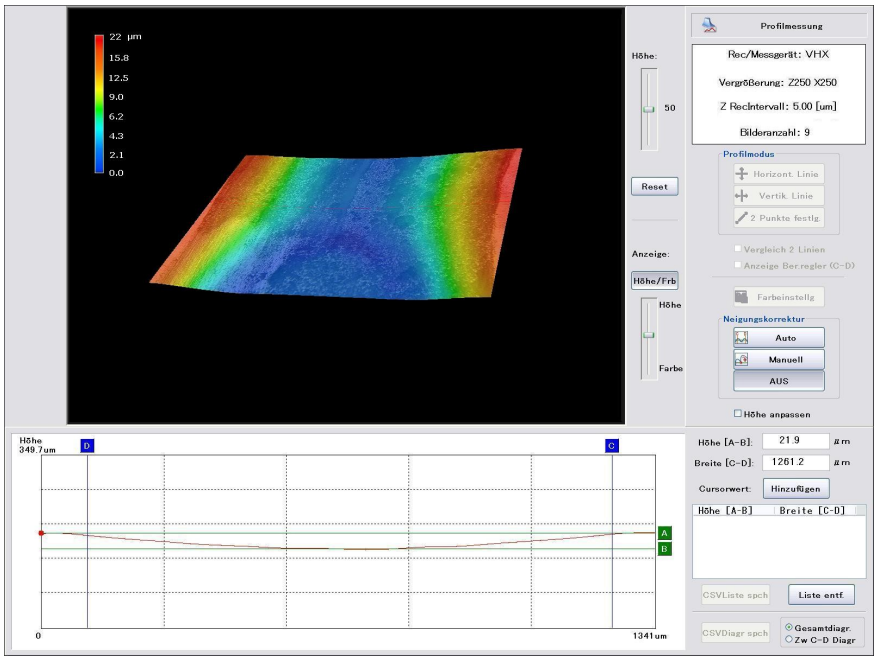

Figure A.4 *Wear track profile on sample TiBN2.2*

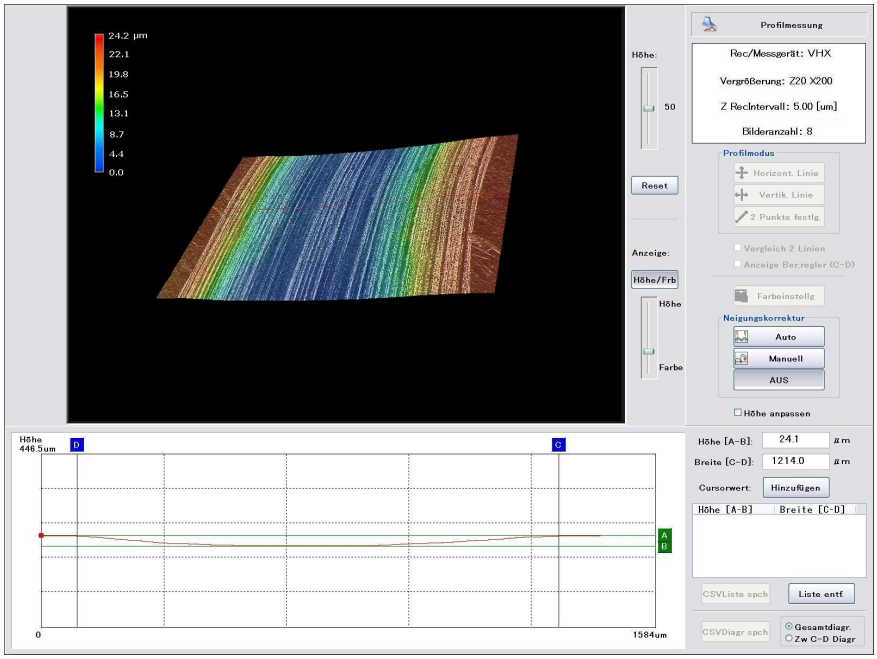

Figure A.5 *Wear track profile on sample TiBN2.4*

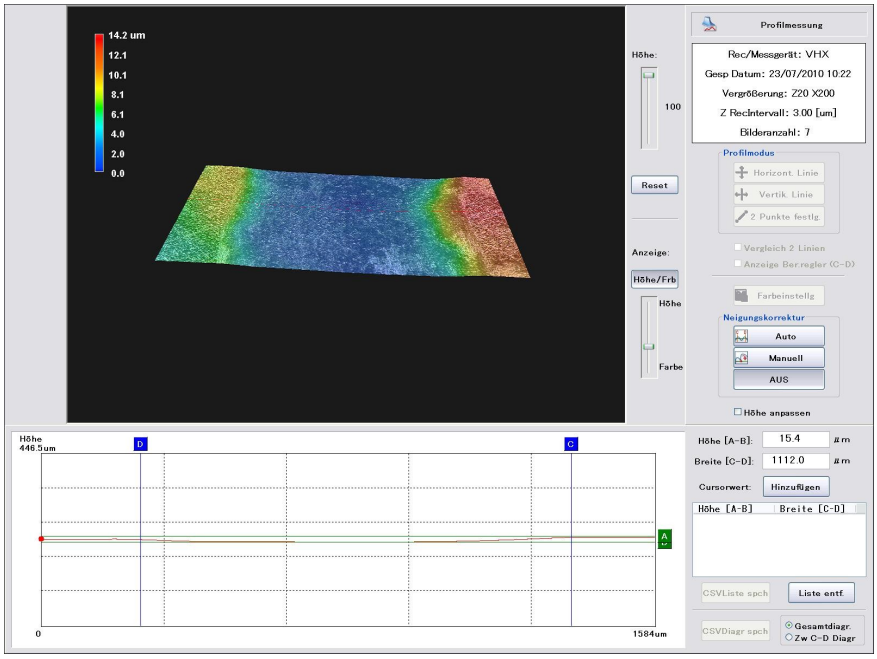

Figure A.6 *Wear track profile on sample TiWC2.3*

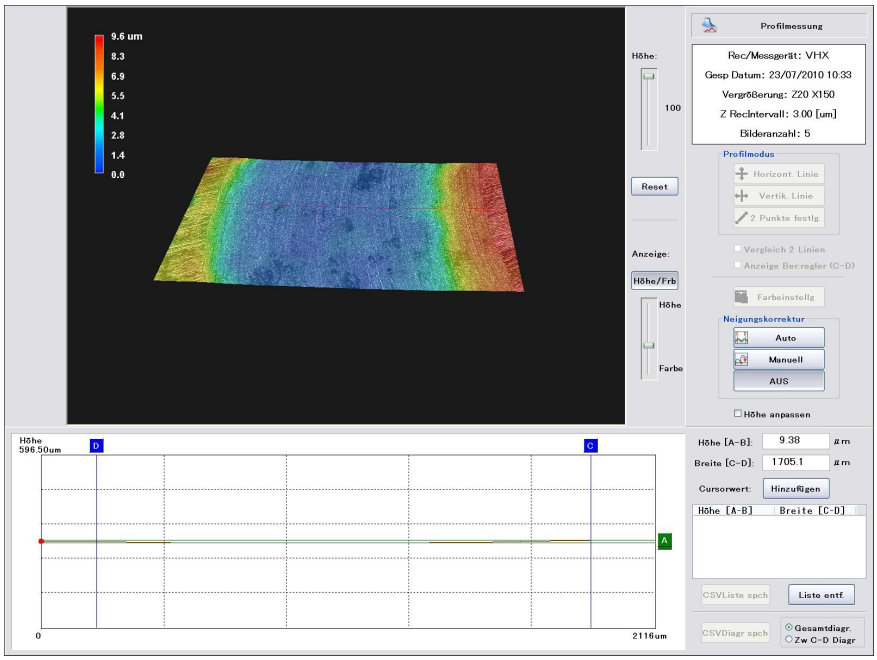

Figure A.7 *Wear track profile on sample TiWC2.4*

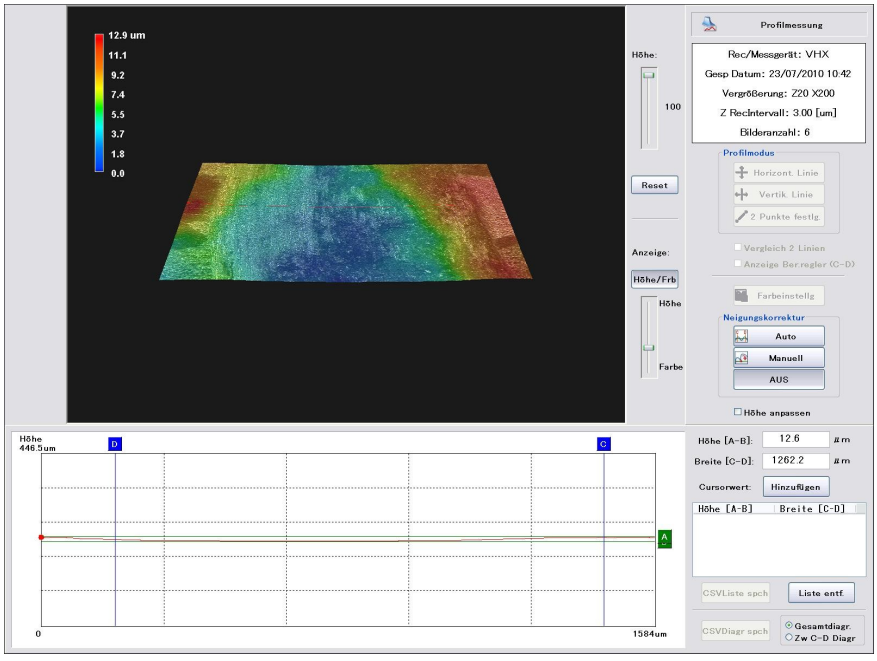

Figure A.8 *Wear track profile on sample TiWC2.5*

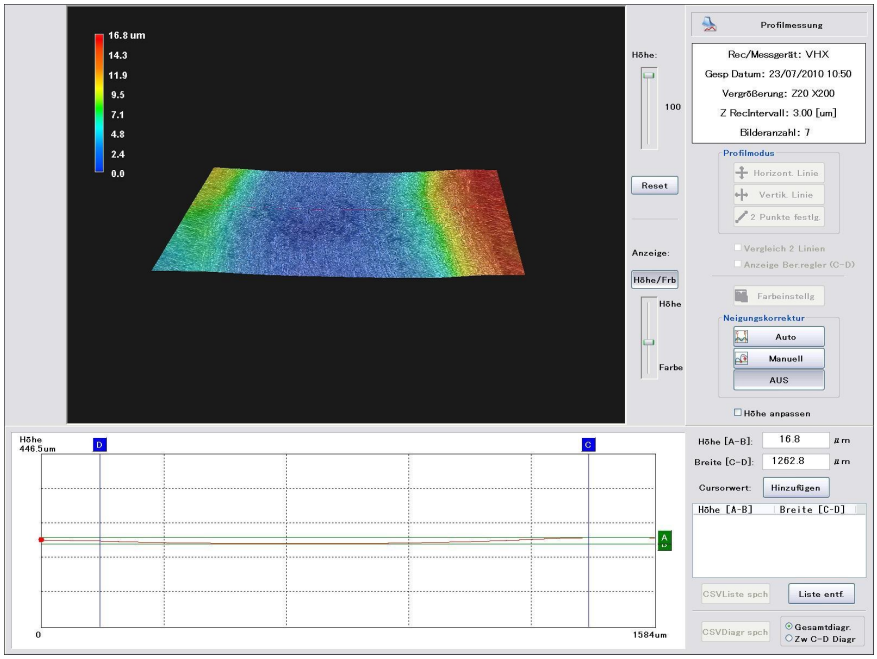

Figure A.9 *Wear track profile on sample TiWC2.6*

Table A.1 *Interpolated values of measured strains and stress calculation for sample TiBN1.3*

Depth [mm]	ε_a [1e-6]	ε_b [1e-6]	ε_c [1e-6]	Alfa Angle [°]	σ_{min} [N/mm2]	σ_{max} [N/mm2]
0,05	-8,53	-4,58	-2,50	7,03	50,94	118,07
0,15	-20,92	-10,64	-7,02	-11,58	64,28	142,38
0,25	-33,31	-16,71	-11,55	-13,46	49,97	110,92
0,35	-45,70	-22,77	-16,07	-14,16	55,08	112,58
0,45	-58,09	-28,83	-20,60	-14,52	60,22	118,39
0,55	-70,48	-34,89	-25,12	-14,74	72,67	135,85
0,64	-82,87	-40,96	-29,65	-14,89	92,69	163,53
0,74	-95,26	-47,02	-34,17	-15,00	123,88	205,92
0,84	-107,65	-53,08	-38,70	-15,08	170,92	267,41
0,94	-120,04	-59,14	-43,22	-15,15	237,20	352,74

Table A.2 *Interpolated values of measured strains and stress calculation for sample TiBN1.4*

Depth [mm]	ε_a [1e-6]	ε_b [1e-6]	ε_c [1e-6]	Alfa Angle [°]	σ_{min} [N/mm2]	σ_{max} [N/mm2]
0,05	-12,29	-7,98	-11,22	-45,33	135,97	215,06
0,15	-16,60	-10,20	-13,25	-37,57	-11,28	8,80
0,25	-20,91	-11,67	-15,27	-33,85	-3,73	20,30
0,35	-25,23	-12,41	-17,29	-32,89	-0,23	34,94
0,45	-29,54	-12,41	-19,32	-33,15	-0,49	47,89
0,55	-33,85	-11,68	-21,34	-33,86	1,06	66,17
0,64	-38,17	-10,21	-23,37	-34,69	-0,97	84,56
0,74	-42,48	-8,01	-25,39	-35,50	-0,88	111,56
0,84	-46,79	-5,07	-27,41	-36,24	2,13	149,09
0,94	-51,11	-1,40	-29,44	-36,91	9,26	203,82

Table A.3 *Interpolated values of measured strains and stress calculation for sample TiBN2.2*

Depth [mm]	ε_a [1e-6]	ε_b [1e-6]	ε_c [1e-6]	Alfa Angle [°]	σ_{min} [N/mm2]	σ_{max} [N/mm2]
0,05	-2,46	-3,42	-6,07	-65,24	40,48	79,77
0,15	-3,58	-5,26	-8,61	-64,91	5,63	12,29
0,25	-6,37	-7,09	-11,14	-64,71	13,36	29,62
0,35	-10,09	-8,93	-13,68	-64,57	17,19	41,49
0,45	-13,98	-10,77	-16,22	-64,47	20,46	44,44
0,55	-17,32	-12,61	-18,75	-64,39	24,70	39,83
0,64	-19,34	-14,45	-21,29	-64,33	20,04	28,63
0,74	-19,30	-16,29	-23,83	-64,28	-16,93	25,48
0,84	-16,47	-18,12	-26,37	-64,24	-89,98	10,59
0,94	-10,08	-19,96	-28,90	-64,21	-228,58	-34,42

Table A.4 *Interpolated values of measured strains and stress calculation for sample TiBN2.4*

Depth [mm]	ε_a [1e-6]	ε_b [1e-6]	ε_c [1e-6]	Alfa Angle [°]	σ_{min} [N/mm2]	σ_{max} [N/mm2]
0,05	-23,12	-16,43	-20,86	-38,60	244,98	353,08
0,15	-45,04	-35,55	-43,71	-40,76	197,58	235,68
0,25	-63,04	-54,67	-66,12	-45,65	125,24	165,46
0,35	-77,14	-73,79	-88,09	-54,42	94,26	168,49
0,45	-87,32	-92,92	-109,62	-68,67	60,72	175,58
0,55	-93,60	-112,04	-130,71	-84,01	34,04	197,46
0,64	-95,95	-131,16	-151,36	85,75	0,15	225,13
0,74	-94,40	-150,28	-171,58	79,89	-47,05	259,96
0,84	-88,94	-169,40	-191,35	76,38	-111,14	301,96
0,94	-79,56	-188,52	-210,69	74,10	-219,92	338,48

Table A.5 *Interpolated values of measured strains and stress calculation for sample TiWC2.3*

Depth [mm]	ε_a [1e-6]	ε_b [1e-6]	ε_c [1e-6]	Alfa Angle [°]	σ_{min} [N/mm2]	σ_{max} [N/mm2]
0,05	444,91	707,73	259,30	-59,37	-936,12	-149,86
0,15	450,54	751,25	230,11	-52,04	139,15	189,21
0,25	414,19	744,81	217,20	-51,94	61,84	161,40
0,35	374,51	767,83	204,05	-50,82	58,45	103,72
0,45	363,04	750,93	200,47	-50,08	-17,23	77,40
0,55	332,72	760,31	192,50	-49,36	27,46	62,83
0,64	305,82	763,30	175,22	-48,56	47,91	71,59
0,74	336,21	683,20	174,00	-49,32	-217,47	104,13
0,84	353,51	614,41	190,74	-51,36	-181,68	75,51
0,94	337,01	582,24	180,44	-51,31	108,15	127,09

Table A.6 *Interpolated values of measured strains and stress calculation for sample TiWC2.4*

Depth [mm]	ε_a [1e-6]	ε_b [1e-6]	ε_c [1e-6]	Alfa Angle [°]	σ_{min} [N/mm2]	σ_{max} [N/mm2]
0,05	108,37	-12,21	159,86	-18,64	-284,55	-148,22
0,15	366,49	170,96	353,73	44,64	-108,04	77,04
0,25	270,10	336,90	363,28	40,08	-8,10	104,62
0,35	172,07	398,68	356,26	-24,84	5,55	82,11
0,45	191,14	378,04	346,47	-26,99	31,35	48,33
0,55	188,95	342,52	310,84	-28,68	-22,40	74,84
0,64	155,05	338,84	276,92	-29,62	-17,81	52,14
0,74	141,54	354,74	265,43	-33,12	3,56	11,08
0,84	105,61	341,70	244,33	-33,91	3,56	5,91
0,94	100,65	330,72	226,60	-34,76	-5,10	19,26

Table A.7 *Interpolated values of measured strains and stress calculation for sample TiWC2.5*

Depth [mm]	ε_a [1e-6]	ε_b [1e-6]	ε_c [1e-6]	Alfa Angle [°]	σ_{min} [N/mm2]	σ_{max} [N/mm2]
0,05	-1,19	-16,97	67,01	-16,36	-123,61	8,82
0,15	171,88	307,38	285,89	2,75	-460,68	-172,66
0,25	216,64	455,29	433,71	-28,74	-114,06	-12,91
0,35	245,42	438,47	470,18	-21,17	-49,33	94,91
0,45	312,90	440,11	442,25	-17,79	-42,29	88,03
0,55	328,12	424,35	409,86	-25,13	48,03	95,62
0,64	318,29	408,50	398,65	-26,38	47,93	66,89
0,74	318,19	433,25	388,70	-30,06	-14,35	76,84
0,84	265,78	394,84	347,92	-32,56	222,99	251,34
0,94	292,52	381,10	318,94	-36,97	-130,94	-0,79

Table A.8 *Interpolated values of measured strains and stress calculation for sample TiWC2.6*

Depth [mm]	ε_a [1e-6]	ε_b [1e-6]	ε_c [1e-6]	Alfa Angle [°]	σ_{min} [N/mm2]	σ_{max} [N/mm2]
0,05	-18,15	-16,09	-9,01	-2,28	18,23	29,79
0,15	-19,35	-19,21	-15,28	12,54	-3,97	3,82
0,25	-32,80	-18,46	-22,13	-12,97	0,70	24,16
0,35	-58,71	-19,95	-20,00	-32,08	-1,17	30,97
0,45	-74,82	-23,03	-9,76	-19,73	-15,23	7,75
0,55	-71,97	-25,93	-4,12	-10,16	-28,29	-6,66
0,64	-71,94	-32,02	-17,17	-6,76	7,32	30,11
0,74	-109,31	-50,04	-51,65	-21,30	101,89	155,10
0,84	-187,43	-82,90	-93,86	-23,27	201,79	302,76
0,94	-246,55	-101,68	-126,08	-26,67	134,33	227,24